HIGH ENERGY X-RAY STUDY OF DEFECT MEDIATED DAMAGE IN BULK POLYCRYSTALLINE NI SUPERALLOYS

by

Diwakar Prasad Naragani

A Dissertation

Submitted to the Faculty of Purdue University

In Partial Fulfillment of the Requirements for the degree of

Doctor of Philosophy

School of Aeronautics & Astronautics

West Lafayette, Indiana

August 2019

THE PURDUE UNIVERSITY GRADUATE SCHOOL
STATEMENT OF COMMITTEE APPROVAL

Dr. Michael D. Sangid, Chair
School of Aeronautics and Astronautics
Dr. Weinong W. Chen
School of Aeronautics and Astronautics
Dr. Paul A. Shade
Air Force Research Laboratory
Dr. David F. Bahr
School of Materials Engineering

Approved by:
Dr. Weinong W. Chen
Head of the Graduate Program

To my parents, Nina and Raghuram,
and my sister, Divya,
for their endless love and support.

ACKNOWLEDGMENTS

First and foremost, I would like to express my sincerest gratitude to Dr. Michael Sangid for all his advice and guidance during the course of my study at Purdue University. He has always led by example as an excellent researcher and an amazing human being. He has always answered queries with an eidetic memory of literature and displayed abundant patience while teaching us. As a mentor he has been always available with keen insight and foresight towards my life and career goals. The completion of thesis would have been possible without your support and encouragement.

I would like to acknowledge the support provided for this work by DARPA (N66001-14-1-4041), the Rolls-Royce Corporation, Air Force Office of Scientific Research (FA9550-14-1-0284), and NSF (F-00067846-02-010). Particularly, Mark Hardy and Iain Parr for providing the initial material at the start of my PhD. A special thanks to Dr. Wayne Chen, Dr. Paul Shade and Dr. David Bahr for serving on my dissertation committee. Use of the Advanced Photon Source was supported by the US Department of Energy, Office of Science, Office of Basic Energy Sciences, under contract No. DE-AC02-06CH11357.

Paul Shade, Joel Bernier, and Hemant Sharma are among those who helped tremendously in the initial stages when the steep learning curve of these experiments and analysis was very daunting for which I will be ever grateful. I would look forward to every discussion with them to not only clarify my doubts but also to leapfrog my understanding, it is only because of these giants that I could see farther and clearer. I am thankful to the staff and scientists at Argonne: Jun-Sang Park, Peter Kenesei, and Jon Almer for their patience and confident demeanor during setup which would usually make our team very anxious. Thanks to Andrea Rovinelli, Reeju Pokharel and Ricardo Lebensohn for their support with my foray into crystal plasticity simulations.

I would like to thank all member of the ACME^2 lab. Andy, John, Imad, Andrea, Saikumar, Prithivi, Ritwik. Ronald, Saikiran, Alex, Todd, Bhisham and Alberto. To Andrea and Imad, I could not have asked for smarter, more helpful people to sit next to than either of you. To Priya, Sven, and Danilo, mentoring you has been a privilege and our discussions have been a learning experience every single time. Finally, Ajey and Kartik, who have been tolerated me at my best and worst both at the lab and at home, thank you for being great friends and teaching me, each in your own way, so much about being zen in life. One of the strengths of the ACME^2 lab is in the

environment of support, teamwork and being offered help without the need to ask. I hope this environment persists in the years to come.

Finally, I would like to thank my family living around the world, it is always difficult to stay in touch with everyone but every time that I have had a chance to catch up, I have been met with a warm embrace. Even though they never really knew what I was doing or why I kept pursuing higher studies they were always supportive. My mother, Nina, for always supporting my ambitions and for all her sacrifice in raising me and always checking up on me. My father, for his support and encouraging me to achieve. And my sister, for always being a role model through her confidence and grace. Thank you all, you are my bedrock.

TABLE OF CONTENTS

LIST OF FIGURES

LIST OF TABLES

LIST OF ABBREVIATIONS

APS	Advanced Photon Source
μ-CT	Computed micro-Tomography
FCC	Face centered cubic
HEDM	High energy diffraction microscopy
FF-HEDM	Far-field HEDM
NF-HEDM	Near-field HEDM
MIDAS	Microstructural Imaging and Diffraction Analysis Software
RAMS	Rotational and axial motion system
EBSD	Electron back-scatter diffraction
DIC	Digital image correlation
SFC	Short fatigue crack
FWHM	Full width at half maximum
PM	powder metallurgy
AM	Additive manufacturing
SLM	Selective laser melting
EVP	elasto-viscoplastic
CP	Crystal plasticity
FEM	Finite element analysis
FFT	Fast Fourier transform

LIST OF SYMBOLS

γ, γ', γ''	Ni matrix with FCC structure and precipitate structures with $L1_2$ ordering and BCT structure resp.
λ	Wavelength of X-ray beam
h, k, l	Miller indices of the diffracting lattice plane
d_{hkl}	Inter-planar distance
$2\theta_{hkl}$	Bragg angle
2θ, η, ω	polar coordinates (radial, azimuthal, and rotational resp.) of a diffraction peak
σ_{ij}	Stress tensor
ϵ_{ij}	Strain tensor
C_{ijkl}	Stiffness tensor
σ_{vm}	von Mises Stress
σ_{Hyd}	Hydrostatic Stress
σ_{TRI}	Stress triaxiality
τ_{MRSS}	Max. resolved shear stress
σ_{CoAX}	Stress coaxiality

ABSTRACT

Author: Naragani, Diwakar, P. PhD
Institution: Purdue University
Degree Received: August 2019
Title: High-energy X-ray study of Defect Mediated Damage in Bulk Polycrystalline Ni-superalloys
Committee Chair: Dr. Michael D. Sangid

Defects are unavoidable, life-limiting and dominant sites of damage and subsequent failure in a material. Ni-based superalloys are commonly used in high temperature applications and inevitably found to have defects in the form of inclusions, voids and microscopic cracks which are below the resolution of standard inspection techniques. A mechanistic understanding of the role of defects in such industrially relevant bulk polycrystalline material is essential for philosophies of design and durability to follow and ensure structural integrity of components in the inevitable presence of such defects. The current understanding of defect-mediated damage, in bulk Ni superalloys, is limited by experimental techniques that can capture the local micromechanical state of the material surrounding the defect. In this work, we combine mechanical testing with in-situ, non-destructive 3-D X-ray characterization techniques to obtain rich multi-modal datasets at the microscale to interrogate complex defect-microstructure interactions and elucidate the mechanisms of failure around defects. The attenuated X-ray beam, after passage through the material, is utilized through computed micro-tomography to characterize the defects owing to its sensitivity to density differences in the material. The diffracted X-ray beam, after illuminating the material, is employed through high energy diffraction microscopy in various modes to interrogate the evolving micromechanical state around the discovered defects.

Three case studies are performed with specimens made of a Ni-based superalloy specially designed and fabricated to have internal defects in the form of: (i) an inclusion, (ii) a microscopic crack, and (iii) voids. In each case, the grain scale information is investigated to reveal heterogeneity in the local micromechanical state of the material as a precursor for the onset of failure. Models and simulations based on finite element or crystal plasticity are utilized, wherever necessary, to assess the factors essential to the underlying mechanism of failure. In the first case study, the detrimental effects of an inclusion in initiating a crack upon cyclic loading is interrogated and the state of bonding, residual stresses, and geometrical stress concentrations around the

inclusion are demonstrated to be of utmost importance. In the second case study, the propagation of a short fatigue crack through the microstructure is examined to reveal the crystallographic nature of crack growth through the (i) alignment of the crack plane with the most active slip system, (ii) the correlation between the crack growth rate and the maximum resolved shear stresses, and (iii) the dependence of the crack growth direction on microplasticity within grains ahead of the crack front. In the third case study, the role of voids in ductile failure under tensile loading is explored to illuminate the activation and operation of distinct mechanisms of inter-void shear and necking under the control of the local state of stress triaxiality and the local plasticity within the grains at critical sites of fracture.

In summary, a grain scale description of the micromechanical state has been unambiguously determined through experiments to examine the heterogeneity around defects in the material. It has enabled us to identify and isolate the nature of factors essential to the activation of specific mechanisms at the onset failure. The grain scale thus provides an ideal physical basis to understand the fundamentals of defect mediated damage and failure instilling trust in the predictive capabilities of models that incorporate the response of the grain structure. The generated datasets can be used to instantiate and calibrate such models at the grain level for higher fidelity.

1. INTRODUCTION

Defects in superalloys are unavoidable [1] and inherent to materials created through any manufacturing process. It is well acknowledged that such defects are discontinuities and weak links in the material that are extremely detrimental [2–7] to the performance and life of structures. The damage tolerant design [8] philosophy is based on the assumption that flaws will exist in any structure and such flaws will propagate with usage. Structures designed under this philosophy should therefore be damage tolerant in their ability to sustain defects safely until maintenance programs enable the detection of cracks and subsequent repair of the component. This design criteria, though effective, force tolerances, allowances, and redundancies that result in overdesigned structures and adoption of stricter maintenance and inspection regiments. These measures directly affect the cost and time of development, the safe and sustained operation of the structure, and are significantly limiting to performance of the system as a whole. The only solution is to understand the mechanism of defect mediated damage at an appropriate scale in order to assess the actual detriment of a defect to the performance of the structure.

Experimental studies which are focused to interrogate damage due to specific defect mechanism have to pave the way for improvement in understanding and assessment of these mechanisms. Macroscopic stress-strain curves and post-mortem fractography have been used extensively and helped immensely to reach the current level of understanding. Carburization and shot peening impart high residual stresses and hardness at the surface making sub-surface damage events more common. These events cannot be captured by surface inspection techniques [6,9–12]. Advanced characterization techniques need to be explored with the ability to generate local microscale information of the material as it is evolving with macroscopic loading and in the vicinity of defects in the bulk of the material. Thus, these techniques have to be performed (i) in-situ while loading the specimen, (ii) non-destructively to capture the evolving state of the material, (iii) illuminate the internal state within the bulk of the material, and (iv) at a resolution that can capture the microscale changes around the defect. The solution can be found in recently developed high-energy synchrotron X-ray characterization techniques.

The premise of this thesis is that the interaction between the defect and a very small region of the microstructure in the vicinity of the defect will help further our understanding of the damage mechanisms associated with the defects. Computed micro-tomography (μ-CT) delivers a solution

for revealing the morphology and location of the defect structure within the sample at the initial state before loading has commenced and the ability to track its evolution to capture the exact locations of failure. High energy diffraction microscopy (HEDM) offers a solution for characterizing the micromechanical state around the defects by revealing the underlying heterogeneous (i) grain structure (orientation maps), (ii) the stress state in each discovered grain, and (iii) the intragranular lattice curvature and lattice strain heterogeneity which accommodates the deformation within the grain. They are revealed through (i) near-field high-energy X-ray diffraction microscopy (NF-HEDM), (ii) far-field high energy X-ray diffraction microscopy (FF-HEDM), and (iii) reciprocal space mapping respectively. These datasets are consolidated to study the interaction of the defect and the evolving microstructure at the sites of failure. The hypothesis is that a grain scale description of the micromechanical state is useful and sufficient to identify and isolate the factors essential to the activation of specific mechanisms at the onset failure and thus provides an ideal physical basis to understand the fundamentals of defect mediated damage. Simulation tools are utilized to show the contribution of the identified factors on the mechanism of failure for each of these defects.

Three case studies are performed with specimens made of a Ni-based superalloy especially designed and fabricated to have internal defects in the form of: (i) an inclusion, (ii) a microscopic crack, and (iii) voids. In the following sub-sections, we will outline the motivation and expected contribution from each study.

1.1 Motivation and Contribution

1.1.1 Case Study 1: Inclusion driven failure

Crack nucleation at inclusions is an unavoidable, dominant and life-limiting failure mode as fatigue progresses to find the ‘weakest link’ in the material. Crack initiation accounts for a significant portion of the fatigue life [13]. After documenting fracture surfaces in a multitude of specimens subjected to cyclic loading, Caton et al. [2] exposed a clear bifurcation between two competing failure modes: crack nucleation at crystallographic facets and crack nucleation at inclusions. The inclusion driven failures showed correspondence with lower lifetimes to failure. Research into the effect of temperature [3], grain size [4], stress level [2], strain range [5] and size of non-metallic inclusions [14] has further demonstrated the prominence of inclusion driven failure

for applications in which superalloys find relevance. A robust understanding of the mechanisms and driving forces behind crack initiation at inclusions is, however, still elusive because most mesoscale characterization tools, available today, are destructive processes and cannot be used in-situ to capture evolution of critical state descriptors around sub-surface features.

Research Contributions:

In this study, we describe an experimental methodology, based on concurrent FF-HEDM and μ-CT, to characterize a large volume of a Ni-based superalloy with an embedded inclusion. The initial state of the sample is fully characterized and subsequently tracked spatially and temporally across an applied deformation schedule by periodically interrupting cyclic loading until a crack initiates. We use the evolution of the local microstructure throughout the volume, especially around the crack, to determine the factors contributing to crack initiation. Various failure metrics and parameters are discussed to understand and rationalize the stress distribution around the inclusion and its role in crack initiation. Finally, a 3-D elasto-viscoplastic (EVP) FFT model is used to comprehend the role of residual stresses and simulate the effect of debonding around the crack initiation site. Qualitative comparisons are performed to aid our understanding of these factors in recreating the observable conditions for crack initiation.

Highlights:

- Spatially, the heterogeneity in stress distribution is a product of a large rigid inclusion at an inclination to the loading axis, the residual stresses that it induces in the surrounding matrix and the bonding state at the inclusion-matrix interface.
- Temporally, the strains grow gradually with loading and stabilize very quickly in a few cycles, only to change locally upon crack initiation.
- The study reveals a gradient that exists in the magnitude of strain across the crack initiation site, a trend that is consistent across other micromechanical fields, and creates the necessary conditions for a crack to initiate.
- Debonding at the inclusion-matrix interface is established to play the pivotal role in creating a gradient in stresses; the sites of debonding were discovered through the experimentally characterized response of the material and the hypothesis of debonding was inferred through proof of principle 3-D EVP-FFT simulations.

1.1.2 Case Study 2: Short fatigue crack driven failure

Short fatigue cracks (SFC) show high variability in growth rates and propagation path as discussed by Pearson in 1975 [15] and has since been the focus of several reviews [16–19]. A SFC is representative of cracks with dimensions which are small in comparison to characteristic microstructural dimensions. The SFC regime, at a size which is practically undetectable during inspection and operating through mechanisms which cannot be predicted by linear elastic or elastic plastic fracture mechanics, can account for the majority of the life of a structure [20,21]. Microstructural attributes, such as grain orientations [22,23], grains sizes [24,25], distance from obstacles like grain boundaries [26–28], and local neighborhoods [29,30], are known to affect SFC. Existing theories and models cannot be accepted into practice until their underpinning assumptions are assessed and appraised with detailed experimental data at the appropriate length scale. The behavior of SFCs still remains elusive, because of the lack of experimental datasets which have been able to corroborate these findings by capturing the heterogeneity associated with the local micromechanical state ahead of the crack front in the bulk of a polycrystalline material under cyclic loading.

Research Contributions:

In this study, we leverage the advent of synchrotron based X-ray characterization techniques, developed in the past decade, to gather relevant micromechanical descriptors at the grain scale, in order to provide a physical basis to our understanding of the SFC regime. The crack, previously initiated, is propagated through the sample under cyclic loading while being experimentally tracked to study the path undertaken and rate of growth of the SFC in relation to the local microstructural state. The role of pertinent micromechanical stress-based fields is discussed to understand their relevance with respect to crack progression. A few representative grains are extracted and discussed in further detail to determine the crystallographic nature of the SFC by determining the alignment of the crack plane and direction of growth to the well-defined slip systems within a grain. The role of the associated normal and resolved shear stress on the crack growth rate is discussed. The evolution of the principal stresses and the resulting plasticity in the form of the lattice deformation within the grains ahead of the crack front are explored to understand their role in determining the SFC growth direction.

Highlights:

- The SFC was tracked from its initiation, as it propagated through ~50 grains in the bulk of the Ni-based polycrystalline sample within a region of interest comprised of ~1700 grains, all of which were characterized at ten different states through cyclic loading.
- The crack grew mostly in an intragranular nature along two parallel planes, during which the stress triaxiality and hydrostatic stresses exhibited high magnitudes, analogous to the opening stress on the crack.
- Low stresses and high values of the stress coaxiality metric were calculated in the grains in the vicinity of a sharp change in the crack path during which the crack grew in an intergranular fashion to form a bridge across low energy grain boundaries.
- During intragranular crack growth, the crack grows on slip planes and slip directions determined by the τ_{MRSS}; further the normal stress relative to the most active slip plane serves as an opening stress during intragranular crack propagation. The magnitude of the τ_{MRSS} shows a correlation with the crack growth rate within the grain.
- The crack front progresses in multiple directions through different grains; the direction of growth can be determined through the severity of the plasticity in the grains ahead of the crack front, in terms of the full width at half maximum (FWHM) measures for intragranular misorientation or lattice strain gradient for each grain. An association to either the arrest or propagation of the crack, in certain directions, is found through the conformance of the principal stress states in the grains ahead of the crack tip.

1.1.3 Case Study 3: Void growth and coalescence driven failure

Void growth and coalescence are the principal modes of ductile failure as tensile loading progresses to localize deformation around the void structure in a material. Ni-based superalloys produced via the additive manufacturing (AM) process are inherently associated with processing defects in the form of microporosity [31,32]. Rapid qualification strategies are becoming increasingly reliant on modeling and simulations, which have shown varying degree of success in the accurate prediction of even the macroscopic response of the material; for example: the peak load, the fracture strain, the path of failure, etc. are easily over-predicted as documented in the Sandia Fracture challenge [33]. The main limitation of the models is in a realistic description of

the intrinsic state of the material and the proper calibration of material properties at an appropriate length scale. The level of detail and the length scale that is requisite for this task is of an open question, but in order to comprehend void driven failure the complex anisotropic response of the material in the immediate vicinity of sites of eventual failure needs to be experimentally explored.

Research Contributions:

In this study, we will interrogate void growth and coalescence in a Ni-based superalloy, produced via an AM process, under tensile loading through in-situ characterization of the micromechanical state at the grain-scale through multi-modal X-ray experiments. A comprehensive dataset that traverses several length scales is employed to mediate a multi-scale analysis of the growth and coalescence of voids to assess the important contributions of each length scale, in terms of critical attributes and their limitations, in a comprehensive assessment of ductile failure. The results highlight the potential of a grain scale analysis. The ability to capture both the locations of coalescence and differentiate between the active mechanisms of failure, within the region of interest, through the generated microscale information is discussed. We offer perspectives on interpreting some intragranular measures that have been determined via reciprocal space mapping and seek their relevance for the regime of ductile failure.

Highlights:

- The size and shape of each void along with their positions, with respect to the surrounding voids in the region of interest, have been determined via μ-CT and tracked until coalescence was captured at several locations; the path of coalescence has been found to be indicative of the mechanism of coalescence prior to ductile failure.
- A specimen scale analysis of void growth, through the Rice and Tracey model implementation, has shown good correspondence with the aggregate geometric changes in porosity but is not representative of the evolution of individual voids.
- A linear elastic-plastic finite element simulation has been instantiated with the exact size, shape, and location of all the voids in the region of interest, which allows for an accurate description of the stress concentrations due to the interaction between voids and is able to precisely determine the sites of experimentally-observed void coalescence, however, the exact mechanisms of coalescence are not ascertained with a homogenized material model.

- The grain structure surrounding the voids has been characterized through far-field HEDM to determine the position, orientation, and lattice strains in each grain of the region of interest, and consolidated with the μ-CT information of the coalescence sites.
- The heterogeneity created in the material, due to the response of the grain structure to macroscopic loading, creates large variations in the micromechanical states, which are not captured by the homogenized material model.
- Two mechanisms of ductile failure were observed: (i) inter-void shearing, which corresponds to grains exhibiting low stress triaxiality and (ii) inter-void necking, which corresponds to grains exhibiting high stress triaxiality.
- High levels of plasticity and stress heterogeneity within the lattice of the grain(s) between voids provides the additional information, along with high stress triaxiality, to provide the necessary and sufficient criteria for inter-void necking based failure.

1.2 Outline

In summary, emerging in-situ, non-destructive characterization experiments based on high energy X-rays are used to

- Identify sites of failure around defects within bulk polycrystalline Ni-superalloys
- Quantify localization of the evolving micromechanical fields in the anisotropic grain structure of the region of interest
- Consolidate the data to discern the factors and active mechanisms that in-part lead to and result from the localization
- Establish and verify the contribution of the identified factors through simulations by incorporating them into the model or running models without their explicit integration (case studies 1 and 3 respectively)

The collected grain-scale information is found to be necessary and sufficient to identify and capture the factors behind the mechanisms of failure.

The dissertation is divided into six chapters; a quick road map of the thesis is as follows:

Chapter 1: The big picture overview of the motivation behind the thesis and the expected contributions of the inducted case studies.

Chapter 2: A synopsis of the experiments and simulations used in this thesis to provide the background necessary to follow the experiment.

Chapter 3, 4, and 5 are case studies on three distinct defect structures found in Ni-based superalloys which have been adapted from published manuscripts and may be read independently.

Chapter 3: Case study 1: Inclusion driven failure

Chapter 4: Case Study 2: Short fatigue crack driven failure

Chapter 5: Case Study 3: Void growth and coalescence driven failure

Chapter 6: The conclusion and broad outlook for future endeavors.

2. METHODS

High energy synchrotron X-ray techniques have enabled the rapid, non-destructive characterization of the internal structure and mechanical state of a test specimen, providing the possibility of tracking the evolution of critical state descriptors around sub-surface features under in situ mechanical loading. All experiments for this work were performed at beamline 1-ID of the Advanced Photon Source (APS) of Argonne National Laboratory [34,35].

2.1 Computed micro-Tomography (μ-CT)

This technique involves collecting X-rays that have been directly transmitted through a sample [36,37]. During passage, the X-rays are absorbed by the material and local variations in density within the material can be captured as an intensity contrast on the detector. This allows characterization in two very important ways. Firstly, inclusions and other impurities in the material have a different chemical composition and their exact location and morphology can be determined. Secondly, discontinuities in the sample, whether they are pre-existing voids, surface aberrations and cracks, can be observed once they nucleate and can be tracked thereafter. The basic setup of collimated-beam tomography consists of a single-axis goniometer perpendicular to the incident X-ray beam with a framing area detector placed downstream of the sample, as shown in Fig. 2.1. The μ-CT detector requires high spatial resolution *i.e.* small effective pixel size and field of view. A custom made high-resolution tomography detector with 3 mm field-of-view and 1.5 μm square pixel size is used at APS 1-ID.

Computed micro-tomography has been adopted in a few different variations: (i) Absorption contrast tomography is obtained when the detector is kept close to the sample, the variations in the intensity in the obtained projections are due to the difference in the mass attenuation coefficients of the different phases and lack of absorption by empty space in the material at cracks and voids; Beer-Lambert law:

$$I = I_o \exp(-\mu x) \tag{2.1}$$

where I and I_o are the intensity after and before passage through a material with an attenuation coefficient of μ and a thickness of x. (ii) Phase contrast tomography is obtained when the detector is kept further away (several times the specimen depth), coherent X-rays form interference fringes

at the transition between phases like at the (a) matrix-inclusion interface, (b) the crack-matrix interface, and (c) the void-matrix interface resulting in accentuated contrast and a sharper segmentation of the defect morphology. (iii) The focused beam passing through the sample and the beam stop, during NF-HEDM scans, also captures an intensity contrast due to the difference in the mass attenuation coefficient between the defect and the matrix, additional μ-CT reconstruction was performed using the beam projected onto the detector during the NF-HEDM scan through the beam-stop. The main challenge that needed to be considered during reconstruction is the low intensity and extra patterns present in the measured beam due to the uneven surface of the beam-stop.

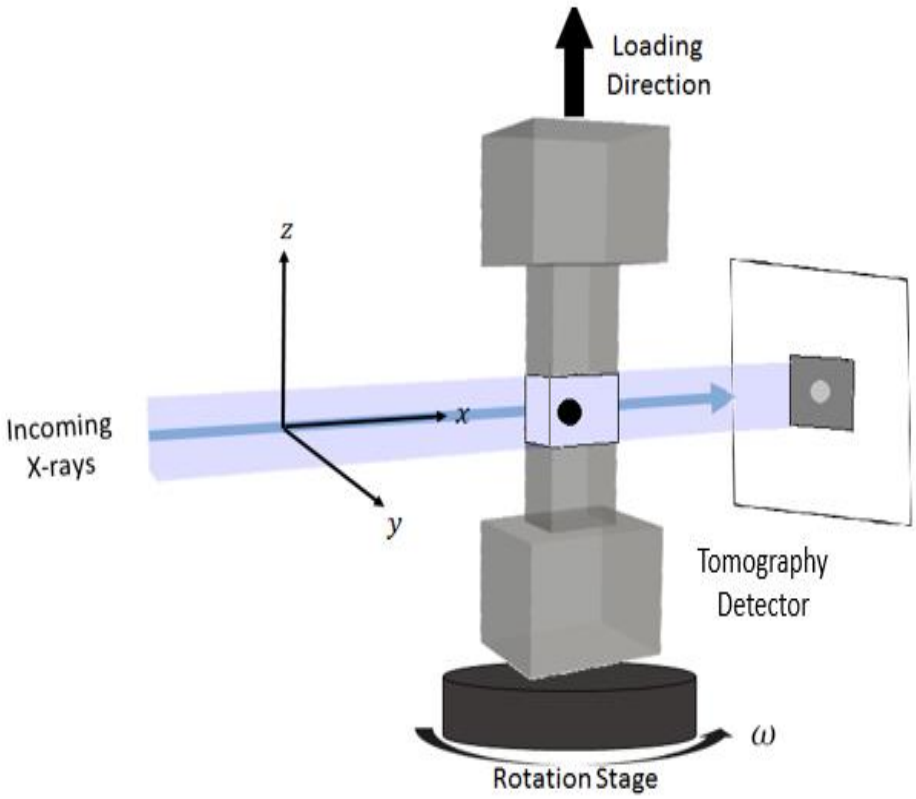

Figure 2.1 Schematic of experimental setup for computed micro-tomography (μ-CT)

The μ-CT scans are reconstructed using an in-house code out of APS [38,39], which uses the GridRec algorithm [40]. The reconstructions were optimized in this code and then post-processed using ImageJ [41], in order to clean up the tomography artifacts and remove noise. Ring removal was performed using an in-house code implemented in Matlab, based on the algorithm specified

in [42]. Segmentation from tomograms is performed via a trainable machine learning algorithm called WEKA segmentation [43], available as an ImageJ plugin. Attributes of the defect, based on its derivatives/gradients to detect edges, eigenvalues of the Hessian matrix to determine plate/line-like features, and structure tensor calculations with smoothing can be employed to extract the precise morphology of the defect.

The μ-CT measurements are complemented by a diffraction-based technique, HEDM, also known as three-dimensional X-ray diffraction microscopy (3DXRD), which can be utilized to gain information about the microstructure and micromechanical state [44].

2.2 High-energy X-ray diffraction microscopy (HEDM)

It is a non-destructive technique for 3-D characterization of bulk polycrystalline specimens around a millimeter in size using a monochromatic beam of X-rays [44–48]. The HEDM technique is essentially the classic rotation method adapted to high-energy X-rays (>50keV) and polycrystalline samples. The fundamental setup is identical to that required for collimated-beam tomography: a single-axis goniometer perpendicular to the incident X-ray beam with a framing area detector placed downstream of the sample. Depending on the type of detector used and specially its position, with respect to the sample, the HEDM technique can be tuned to be sensitive to angular or spatial resolution. Due to the constraints imposed by Bragg's law:

$$n\lambda = 2d_{hkl}sin\theta_{hkl} \tag{2.2}$$

where λ: wavelength of X-ray beam, *hkl*: Miller indices of the diffracting lattice plane, d_{hkl}: interplanar distance, $2\theta_{hkl}$: Bragg angle and n is 1. In the case of a monochromatic beam, a single crystal must be specifically oriented such that the crystallographic plane parameterized by the Miller indices (*hkl*) can diffract. Namely, $-\hat{G}_{hkl} \cdot \hat{k}_i = \sin\theta_{hkl}$, where $\hat{G}_{hkl}$ is a unit reciprocal lattice vector (*i.e.* crystallographic plane normal) and $\hat{k}_i$ is the unit wavevector (*i.e.* propagation direction) of the incident X-ray beam. Note that these equations describe a cone around the incident beam associated with each unique value of d_{hkl} for fixed λ; therefore, to observe diffraction from different planes of a single crystal, it must be rotated such that the specific plane normal lies on the associated cone. Because the observed Bragg condition is very sharp for well-ordered crystals, in practice the detector integrates, while the specimen is rotated over a small angular range, $\Delta\omega \approx 0.25°$, which can be done in a continuous "flying" mode for $\omega \in (0, 360^o)$ with modern area

detectors. In this way, a 3-D image series is formed from the frames integrated over equi-spaced Δω. If we parameterize a diffracted beam signal using polar coordinates ($\rho \rightarrow 2\theta, \eta$) and the ω position in the rotation image series of the measured peak, the coordinates (2θ, η, ω) of all the peaks produced by an orientation encode its crystallographic orientation, centroid in the specimen, and elastic strain. The central challenge of HEDM data analysis is the association of measured 3-D Bragg peaks in the image series to an orientation (grain) in the sample, a procedure referred to as indexation.

2.2.1 Far-field HEDM (FF-HEDM)

In the far-field (FF) configuration, when the detector is ~1 m from the sample, diffraction peaks from different families of crystallographic planes lie near the projection of the ideal Debye-Scherrer cones on the detector, as shown in Fig. 2.2. The diffraction peaks can be pre-sorted by $\{hkl\}$ up to degeneracy in d_{hkl} before associating/indexing them to the different grains that produced them. FF-HEDM technique requires high angular resolution (intermediate effective pixel size and large field of view). A GE-41RT amorphous silicon flat panel detector [49] with a size of 2048 X 2048 pixels at a pixel pitch of 200 μm is employed at APS 1-ID. High angular sensitivity allows resolution of elastic strains in the lattice but, because of large distance from the sample, spatial resolution is limited and only grain averaged values can be extracted. Note that because full elastic strain tensors are available for each grain indexed by the analysis, the corresponding stress tensors are determined unambiguously via the stiffness tensor using the generalized Hooke's law. For more information about FF-HEDM implementation and data reduction strategies, please refer to [46–48,50].

FF-HEDM scans were reconstructed in this work through the use of the Microstructural Imaging and Diffraction Analysis Software (MIDAS) [51,52], developed at the APS. Calibration of the experimental setup in terms of the sample to detector distance, the center of the X-ray beam, the detector tilts, and distortion parameters are very important and facilitated by a suite of calibration images using Ceria and single crystal Au. Far-field HEDM data is reconstructed to provide the grain centroid position (3 variables), an associated grain averaged orientation (3 variables), and a grain averaged elastic strain tensor (6 variables). A completeness value is calculated as the ratio of measured to expected diffraction spots for a given crystal orientation and position. A value of one implies that all the spots that are expected to be found for the grain were

measured. Spatial resolution of ~20 µm for the grain centroid positions, angular resolution within 0.1° for the crystallographic orientation, and a lattice strain resolution on the order of 1e-4 for the grain average value [52,53]. This error increases with uncertainty in determining the center of the spot, as it deforms due to the applied load, a rule-of-thumb error in grain centroid position is around 50 µm.

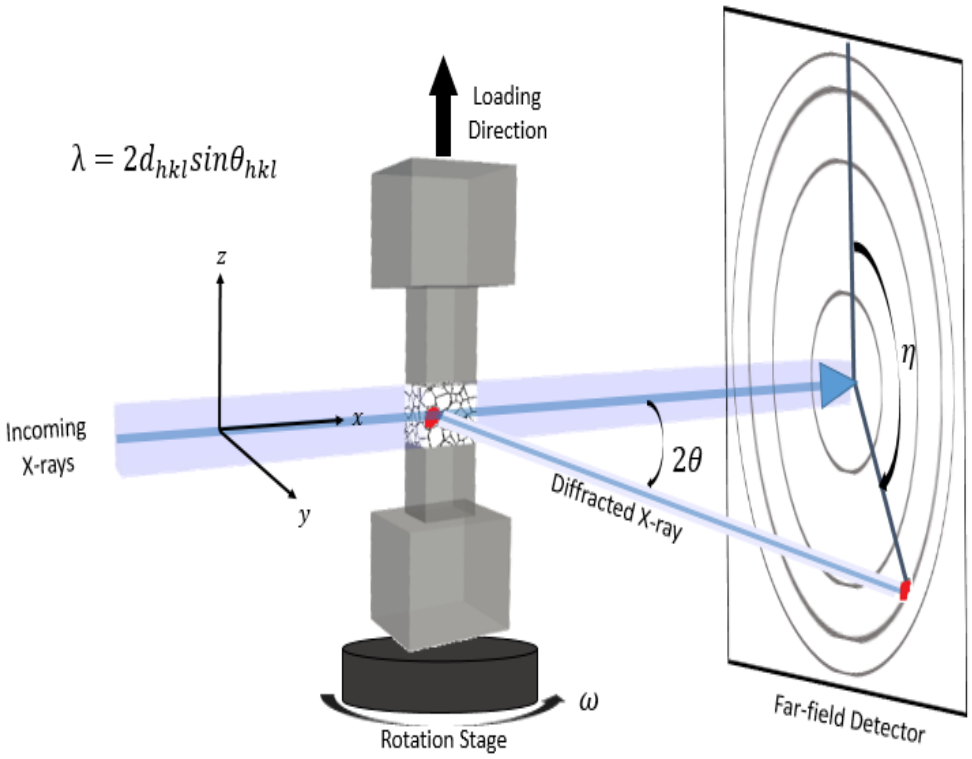

Figure 2.2 Schematic of experimental setup for FF-HEDM

2.2.2 Near-field HEDM (NF-HEDM)

In the near-field (NF) configuration the detector is placed ~ 5-15 mm from the sample, as shown in Fig. 2.3. The setup [35,46,54–56], similar to µ-CT, requires high spatial resolution *i.e.* small effective pixel size and field of view. Hence, the same high-resolution detector with 3 mm field-of-view and 1.5 µm square pixel size is used at APS 1-ID. It uses a line focused beam [34] for selecting a quasi-two-dimensional slice of the sample and a small beam-stop that blocks the very intense focused beam without compromising the diffracted beam from the grains. The diffraction peaks from different families of crystallographic planes do not lie near the projection

of the ideal Debye-Scherrer cones on the detector at this distance because the position of the diffraction event still dominates. Several detector distances are used to calculate the diffraction vector and determine the point of origin of diffraction. The higher spatial resolution allows further discretization of the diffraction spot, which, after indexing, can be associated to specific locations in the sample space and used to create detailed grain maps. This is however at the cost of angular resolution and strains cannot be resolved using this technique.

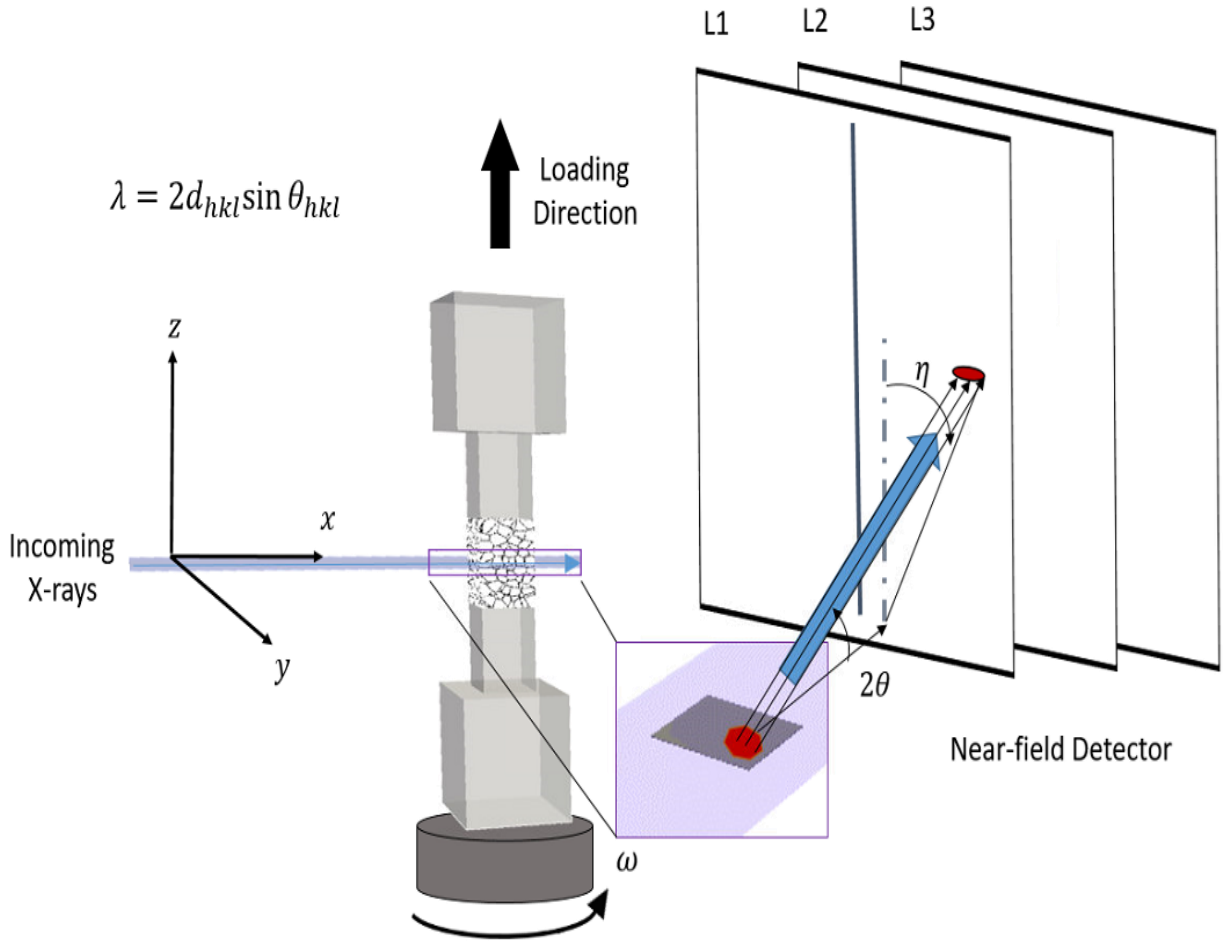

Figure 2.3 Schematic of experimental setup for NF-HEDM

Near-Field HEDM scans were reconstructed using an extension of MIDAS [51,52]. The reconstruction is performed with a triangular grid; an edge size of 2 µm was used to obtain a high signal to noise ratio for a detector pixel size of 1.5 µm. The orientation search space for forward modeling was seeded with orientations determined from FF-HEDM reconstruction, with a

tolerance of 2°. The tolerance in the orientation space allows for identification of intragranular orientations and grains with higher confidence. Any pixels and regions with a confidence of less than 40% were refit with all possible orientations from a gridded table representative of the FCC fundamental space. The triangular mesh is re-gridded onto a regular 3D co-rectangular mesh with a resolution of 1.5 μm and smoothed via a dilation and erosion procedure. A grain growth algorithm based on enabling a maximum misorientation of 2° of neighboring voxels was employed to segment the orientation maps into grains.

2.2.3 Reciprocal space mapping

Spot spreading is primarily due to the deformation of the lattice in the diffracting grain. The damage to the lattice can be broadly divided into two contributing, yet distinct, parts: the curvature in the lattice and the distribution of the lattice strains within the grain (i.e. an elastic strain gradient). Since X-ray diffraction measures the orientation of the lattice planes and the lattice spacing with high resolution, it is inherently able to capture these curvatures and heterogeneities within a grain. In an ideal case, the well order lattice within a grain will have perfectly aligned lattice plane normals and a lattice spacing that is consistent throughout the grain. This results in a sharp and well defined diffraction spot. As the sample is loaded, geometric deformation ensues and is accommodated by the lattice of the grains via plasticity and a stress field. The plasticity is accommodated through distortions in the lattice of the grains, in the form of geometrically necessary dislocations resulting in an intragranular orientation spread. Meanwhile, the stress fields, due to the dislocations or elastic mismatch between neighboring grains, are accommodated through lattice strain gradients. In essence, the degree of plasticity and lattice strain gradients accommodated in the grains can be quantified based on the spread of the diffraction spots.

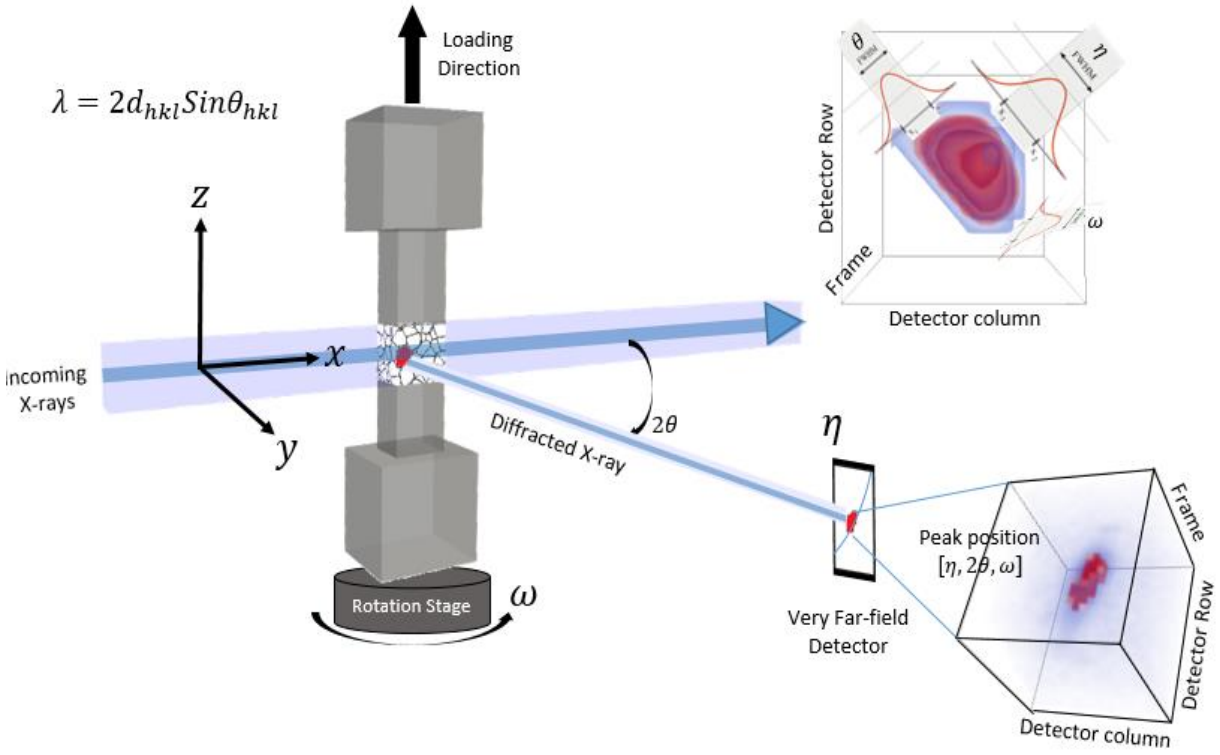

Figure 2.4 Schematic of experimental setup for reciprocal space mapping

The distortion to the lattice can be measured by calculating the full width at half maximum (FWHM) for a set of diffraction spots corresponding to the specified grain along two decoupled polar directions (η and θ), as shown in Fig. 2.4. Along 2θ or the radial direction, the FWHM corresponds to the heterogeneity in the lattice strains within the grain [57,58]. The FWHM along η (along the azimuth on the detector) or ω (across frames during rotation of the sample) corresponds to the curvature of the lattice planes within the grain [57,59]. In this polycrystalline sample, multiple grains accommodate the deformation in the region of interest. An in-house code was developed in an effort to quantify this damage within the grains via the FWHM measures on all diffracting planes. A virtual diffraction simulation, as described in [58], was adapted from algorithms in MIDAS and used to determine the peak positions from the reconstructed grains. The position, orientation, and lattice strains of the grains determined through FF-HEDM, via MIDAS, were used as an input, while the position of the diffraction spots in terms of the η, ω, and θ coordinates on the detector were obtained as the output from the diffraction simulator. The

simulator was coupled with an extraction and thresholding procedure, in order to determine the FWHM of all the spots indexed to a grain.

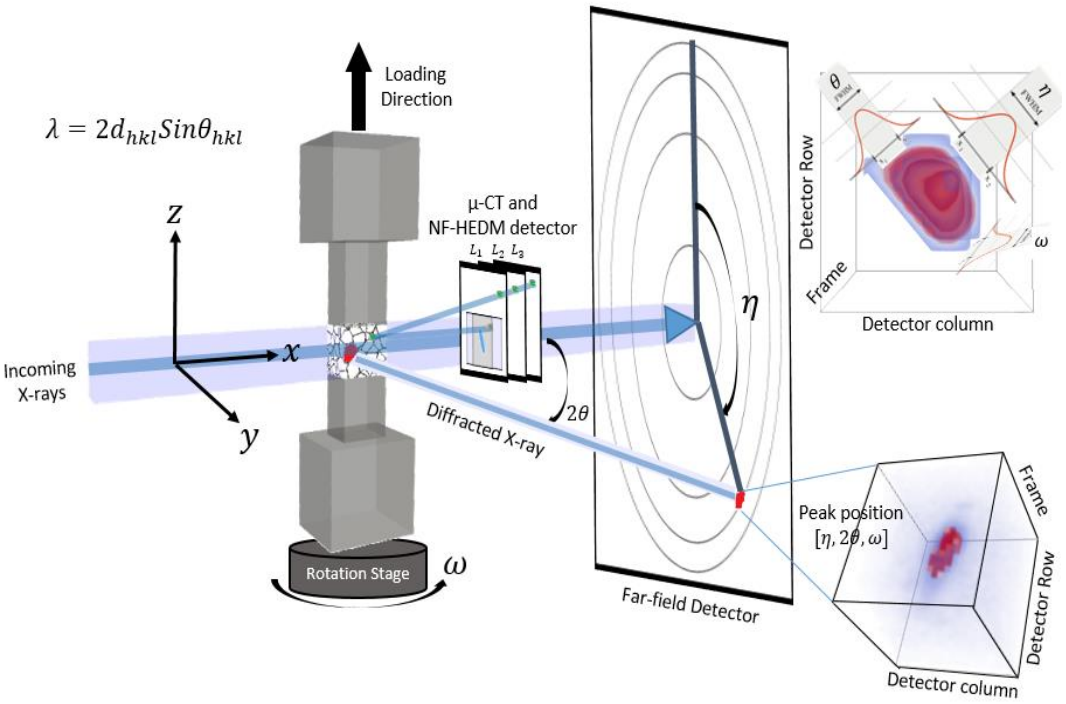

Figure 2.5 Schematic of experimental setup at APS 1-ID for in-situ combined μ-CT, NF-HEDM, FF-HEDM, and reciprocal space mapping

All the above X-ray characterization techniques can be performed concurrently using the setup in the schematic shown in Fig. 2.5. The following techniques were used to design and guide the X-ray characterization experiment.

2.3 Electron Back-Scatter Diffraction (EBSD) and Digital Image Correlation (DIC)

Electron backscatter diffraction (EBSD) is a material characterization technique capable of capturing individual grain orientations, local texture, spatial orientation correlations, and the phases present in the material. To achieve the mirror-like surface necessary for EBSD characterization, the surface of each specimen needs to be polished using sand paper, silica suspensions and then the contaminants need to be removed using sonication, for more details please see reference [60]. The scans are performed using an EDAX scanning electron microscope

and the in-built OIM analysis software to clean-up the raw orientations and output grain maps. These back-scatter electron (BSE) images and the grain maps are analyzed to reveal the underlying precipitate structure and the grain statistics on texture and size distribution in this work to inform the design of the X-ray diffraction experiment.

Digital image correlation is a technique to track features on a specimen's surface. With applied deformation these features move creating a displacement field. Within solid mechanics, these displacement fields are differentiated to obtain in plane strain. Many studies have been presented on DIC, please refer to review papers [61,62]. Strain localization with respect to microstructural features can be determined by combining DIC with electron backscatter diffraction [63]. DIC is a technique with many advantages; (1) simple set-up and data flow to combine EBSD-DIC, (2) scalable in terms of resolution, very dependent on optic setup and trackable features, (3) when combined with EBSD, sub-grain resolution for strain accumulation and good spatial resolution of microstructure. DIC also presents some drawbacks; (1) Only in-plane strain is captured, due to the single camera capture, (2) only surface strains are found, the bulk behavior is still uncertain, (3) strain found is only relative to a reference image or state and cannot capture manufacturing pedigree of the material. DIC is primarily used in this work during the X-ray experiment to determine the macroscopic strain due to the applied load and to determine the rigid body motion and re-center on the region of interest after each load increment, the procedure for re-centering can be found in [64].

2.4 Simulations

2.4.1 Finite element modeling

In an effort to model the response of a homogenized description of the material an isotropic material definition was used. A linear elastic and step wise plastic material model with J2 plasticity can be used with Abaqus. With this definition the Mises yield surface is used to define isotropic yielding. It is defined by giving the value of the uniaxial yield stress as a function of uniaxial equivalent plastic strain. This material model is used in a simple finite element framework in Abaqus.

2.4.2 Crystal plasticity FFT

A brief overview of the principal characteristics of the EVP-FFT formulation is provided below. For details please refer to [65]. The EVP-FFT image-based framework can directly use 3-D images of polycrystalline microstructures obtained via synchrotron based high energy diffraction microscopy (HEDM) as an input into the simulations. A macroscopic strain is imposed on the simulated volume through incremental steps at an imposed strain rate. Due to the mechanical boundary conditions, this applied strain rate results in a response to the stress and strain fields. The EVP-FFT algorithm is used to compute a compatible strain field and an equilibrated stress field, which satisfies the constitutive relation at every point in the volume. The constitutive crystal plasticity relations are then as follows:

$$\sigma(x) = C(x): \varepsilon^e(x) = C(x): \left(\varepsilon(\mathrm{x}) - \varepsilon^{\mathrm{pl}}(x)\right) = C(x): (\varepsilon(\mathrm{x}) - \varepsilon^{\mathrm{pl,t}}(x) - \varepsilon^{\mathrm{pl,t}}\Delta t) \quad (2.3)$$

where $\sigma(x), C(x), \varepsilon^e(x), \varepsilon(\mathrm{x}), \varepsilon^{\mathrm{pl}}(x)$ are the stress tensor, the fourth-order stiffness tensor, elastic, total and plastic parts of the strain tensor at spatially varying position, x. $\varepsilon^{\mathrm{pl,t}}$ is the plastic strain at time t, and Δt is the time increment.

$$\dot{\varepsilon}^{\mathrm{pl}}(x) = \sum_{\alpha=1}^{N} M^{\alpha}(x)\dot{\gamma}^{\alpha}(x) = \dot{\gamma}_0 \sum_{\alpha=1}^{N} M^{\alpha}(x) \left(\frac{|M^{\alpha}(x):\sigma(x)|}{\tau^{\alpha}_{CRSS}(x)}\right) sgn\left(M^{\alpha}(x):\sigma(x)\right) \quad (2.4)$$

where $\dot{\varepsilon}^{\mathrm{pl}}$ is the plastic strain rate, N is the number of slip systems, $\dot{\gamma}^{\alpha}$, τ^{α}_{CRSS}, M^{α} are the resolved shear strain rate, the critical resolved shear stress (CRSS), and the symmetric Schmid tensor associated with the slip system α. $\dot{\gamma}_0$ is a normalization factor and n is the rate sensitivity exponent.

In Fourier space, the convolution integral between Green's function of a linear reference homogeneous medium and a polarization field, which is needed to determine the displacement field of a nonlinear heterogeneous medium, is reduced to a simple tensorial product and hence can be solved efficiently.

A generalized Voce's hardening law based on shear strain accumulation on each slip system is used in the current formulation:

$$\tau^{\alpha}_{CRSS}\left(\Gamma^{\alpha}_{hard}(x,t)\right) = \tau_o + \left(\tau_1 + \theta_1 \Gamma^{\alpha}_{hard}(x,t)\right)\left[1 - exp\left(-\frac{\theta_0\, \Gamma^{\alpha}_{hard}(x,t)}{\tau_1}\right)\right] \quad (2.5)$$

where τ_o is the initial CRSS, $\tau_o + \tau_1$ is the CRSS related to the asymptotic behavior, θ_0 is the stiffness at the end of microscopic linear elastic zone, θ_1 is the asymptotic stiffness at high strain.

$\Gamma_{hard}^{\alpha}(x,t)$ is a weighted sum of the accumulated resolved shear strain of all the slip systems as a function of position, x, time, t and hardening interaction matrix, $h_{\alpha\beta}$:

$$\Gamma_{hard}^{\alpha}(x,t) = \sum_{\beta=1}^{N} h_{\alpha\beta} \int_{t=0}^{t} \dot{\gamma}^{\beta}(x)dt \tag{2.6}$$

where β, like α, also loops over all the slip systems.

The multiplicative decomposition of the deformation gradient $F = F^{*}.F^{p}$ is used to describe lattice rotations and complete the crystal plasticity framework. In this study, a parallelized version of the software is used as described in [66].

3. INVESTIGATION OF FATIGUE CRACK INITIATION FROM A NON-METALLIC INCLUSION VIA HIGH ENERGY X-RAY DIFFRACTION MICROSCOPY

A complete description of the chapter can be found in:

D. Naragani, M.D. Sangid, P.A. Shade, J.C. Schuren, H. Sharma, J.-S. Park, P. Kenesei, J. V. Bernier, T.J. Turner, I. Parr, Investigation of fatigue crack initiation from a non-metallic inclusion via high energy X-ray diffraction microscopy, Acta Mater. 137 (2017) 71–84. doi:10.1016/j.actamat.201707.027. [67]

3.1 Chapter Abstract

Crack initiation at inclusions is a dominant, unavoidable and life-limiting failure mechanism of important structural materials. Fatigue progresses in a complex manner to find the 'weakest link' in the microstructure, leading to crack nucleation. In this study, fully 3-D characterization methods using high-energy synchrotron x-rays are combined with in-situ mechanical testing to study the crack initiation mechanism in a Ni-based superalloy specimen. The specimen was produced via powder metallurgy and seeded with a non-metallic inclusion. Two x-ray techniques were employed: absorption contrast computed micro-tomography (μ-CT) to determine the morphology of the inclusion and its location in the gauge section of the specimen; and far-field high-energy diffraction microscopy (FF-HEDM) to resolve the centroids, average orientations, and lattice strains of the individual grains comprising the microstructure surrounding the inclusion. Sequential μ-CT and FF-HEDM scans were carried out at both peak and zero applied stress following schedules of cyclic deformation. The μ-CT data showed the onset and location of crack initiation, and the FF-HEDM data provided temporal and spatial evolution of the intergranular strains. Strain partitioning and the associated stress heterogeneities that develop are shown to stabilize within a few loading cycles. Elasto-viscoplastic fast Fourier transform simulations were utilized to supplement interpretation of the experimental stress distributions and compared with the experimental stress distributions. Appropriate conditions for crack nucleation in the form of stress gradients were demonstrated and created by virtue of the inclusion, specifically the residual stress state and local bonding state at the inclusion-matrix interface.

3.2 Introduction

Cracks Nickel-based superalloys find extensive application in nuclear reactors, gas turbine engines and propulsion systems that are subject to extreme environments. These alloys are produced via a variety of processes, the most prominent of which is a powder metallurgy (PM) route, chosen in order to generate superior properties through greater control over compositional ranges and microstructure [1]. The alloying elements and the manufacturing process, however, inherently introduce unwanted non-metallic inclusions into the otherwise optimized microstructure. Research into processing techniques and improvement in general purity and quality standards for the powder and processing route have had success in reducing, but not completely eliminating, their occurrence in structural alloys.

Crack initiation accounts for a significant portion of the fatigue life [13]. After documenting fracture surfaces in a multitude of specimens subjected to cyclic loading, Caton et al. [2] exposed a clear bifurcation between two competing failure modes: crack nucleation at crystallographic facets and crack nucleation at inclusions. The inclusion driven failures showed correspondence with lower lifetimes to failure. Research into the effect of temperature [3], grain size [4], stress level [2], strain range [5] and size of non-metallic inclusions [14] has further demonstrated the prominence of inclusion driven failure for applications in which superalloys find relevance. Conclusively, crack nucleation at inclusions is an unavoidable, dominant and life-limiting failure mode as fatigue progresses to find the 'weakest link' in the material. A robust understanding of the mechanisms and driving forces behind crack initiation at inclusions is, however, still elusive.

Towards the goal of an improved understanding of inclusion driven failures, many mesoscale characterization tools are available today for mapping the underlying deformation and damage in polycrystalline materials. For example, 2-D measurements on a specimen free surface through diffraction contrast in a transmission electron microscope [9] or high-resolution electron back-scatter diffraction (EBSD) [6,10–12] have been successful in revealing elastic mismatch and plastic deformation through dislocation density accumulation in the vicinity of inclusions at the surface. In most cases, however, crack initiation from inclusions occurs at sub-surface features, where the effect of surface stress relaxation and advantages of compressive residual stresses through surface treatments like shot-peening subside, and the underlying matrix-inclusion interactions become prominent. EBSD can be combined with serial sectioning techniques such as focused ion beam milling [68], femtosecond laser ablation [69] and mechanical polishing [70] to

collect data within the bulk of a sample. These processes, however, are destructive and cannot be used in situ to capture evolution of critical state descriptors around sub-surface features.

The effect of residual stresses on fatigue lifetimes has been well documented [71,72] but the quantification of these stresses on a grain by grain basis has been difficult until recently. Far-field HEDM measurements can capture the residual stress state in a specimen at this scale [64,73,74]. Recent studies utilizing FF-HEDM measurements demonstrated that the residual stress state at the beginning of an experiment had a significant influence on the grain level stress state of a specimen [64,73–75]. The FF-HEDM measurements are utilized in the current work to unravel the internal stress state of the sample, especially around the inclusion-matrix interface. Once measured, these stresses can be used to initialize simulations [73–77] and check the stress evolution due to applied load from an initialized state that incorporates processing and heat-treatments prior to that point. Fast Fourier transform (FFT) simulations [65] are particularly well suited for such studies since voxelized information from FF-HEDM results can be used as a direct input and compared [78] to experimental results. Frameworks have also been established to incorporate the residual state of the material by means of an Eigen stress [79].

In this chapter, we describe an experimental methodology, based on concurrent FF-HEDM and μ-CT, to characterize a large volume of a Ni-based superalloy with an embedded inclusion. The initial state of the sample is fully characterized and subsequently tracked spatially and temporally across an applied deformation schedule by periodically interrupting cyclic loading until a crack initiates. We use the evolution of the local microstructure throughout the volume, especially around the crack, to determine the factors contributing to crack initiation. Various failure metrics and parameters are discussed to understand and rationalize the stress distribution around the inclusion and its role in crack initiation. Finally, a 3-D elasto-viscoplastic (EVP) FFT model is used to comprehend the role of residual stresses and simulate the effect of debonding around the crack initiation site. Qualitative comparisons are performed to aid our understanding of these factors in recreating the observable conditions for crack initiation.

3.3 Material and specimen design

The material selected for this study is a super solvus heat treated coarse grain variant of RR1000, a polycrystalline Ni-based superalloy with a face centered cubic (FCC) crystal structure strengthened with a distribution of secondary and tertiary $L1_2$ γ’ precipitates. Details of the PM

route, extrusion, isothermally forging and two-step heat treatment process used to produce the samples can be found in [80]. This creates recrystallized, equiaxed grains with minimum substructure, which results in well separated and distinguishable diffraction spots on the detectors. The average grain size for this sample was around 30 μm [81].

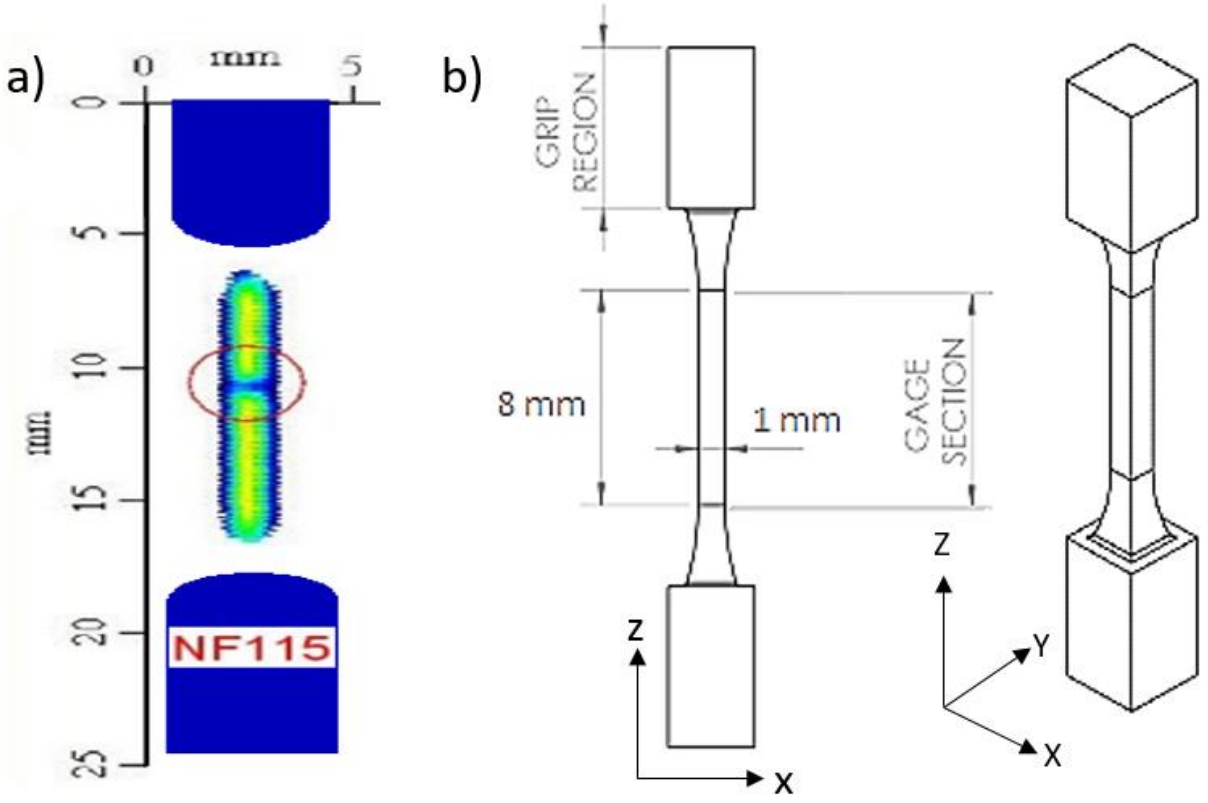

Figure 3.1 a) Ultrasonic inspection of the sample to ascertain presence of an inclusion in the gauge section and b) specimen geometry.

This particular batch was deliberately seeded with a controlled distribution of alumina inclusions of the same composition, but larger than those commonly observed in this alloy under typical processing conditions. Ultrasonic inspection was used to determine the location of an inclusion in the volume of the PM component. The use of ultrasonic inspection, and the associated resolution of this technique, limited us to only find larger inclusions. These are representative of ceramic inclusions that exist as either discrete particles or agglomerates of fine particles and originate from the melting crucible, pouring tundish or atomizing nozzle with aluminum as the

major metallic element [82]. Once found, electro-discharge machining was used to extract samples, such that the inclusion was located in the 1 mm x 1 mm cross-section gauge of the sample. The specimen geometry can be seen in Fig. 3.1. The 1 mm square cross-section of these samples was designed to allow high energy X-rays to penetrate the entire sample, while the rest of the specimen geometry is compatible with the in situ rotation and loading stage described in the next section.

3.4 Experimental setup

The experiment was conducted at beamline 1-ID [34,35] of the Advanced Photon Source (APS) at Argonne National Laboratory. High-energy X-rays at the hafnium K-edge of energy E = 65.351 keV or wavelength $\lambda = 0.018972$ nm allowed us to easily penetrate the 1 mm square cross-section of a Ni-based superalloy sample. The experimental setup and the coordinate system followed in this study are illustrated in the schematic shown in Fig. 3.2. We utilized a custom designed rotational and axial motion system (RAMS) load frame insert that was installed in a servo-hydraulic load frame that is available at the APS 1-ID beamline [83]. The RAMS load frame insert enables the sample to be rotated while independently applying tensile/compressive axial loading. This assembly offers the ability to perform scans that traverse a complete 360° rotation of the sample without blocking the X-ray beam at any point and allows the μ-CT detectors to be positioned close to the sample.

μ-CT and FF-HEDM require complementary instrument configurations; the difference lies in the beam configuration and the detector types and arrangements, which is chosen to obtain optimum quality measurement data for the associated techniques as described below:

1. With absorption contrast μ-CT, we aimed to scan large sections of the sample volume encompassing the inclusion and any crack that might initiate. An X-ray beam, 2 mm wide and 1.5 mm tall, was used for this purpose. This allowed the inclusion to be quickly located along the sample gauge length, as shown for example in the radiograph displayed in Fig. 3.3(a). A custom made high-resolution tomography detector with 3 mm field-of-view and 1.5 μm square pixel size was used. The detector was positioned 55 mm from the sample to enable phase contrast enhancement of features. The sample is rotated over 360° angular range and images are captured in 0.2^{o} steps. This enabled sufficient resolution in the reconstructions to detect minute cracks, if any, in the sample. After the initial characterization of the desired sample

volume, scans were only taken at maximum load where we anticipated the cracks to be open and thus easier to detect via μ-CT. A spatial resolution of ~3 μm was possible with this setup.

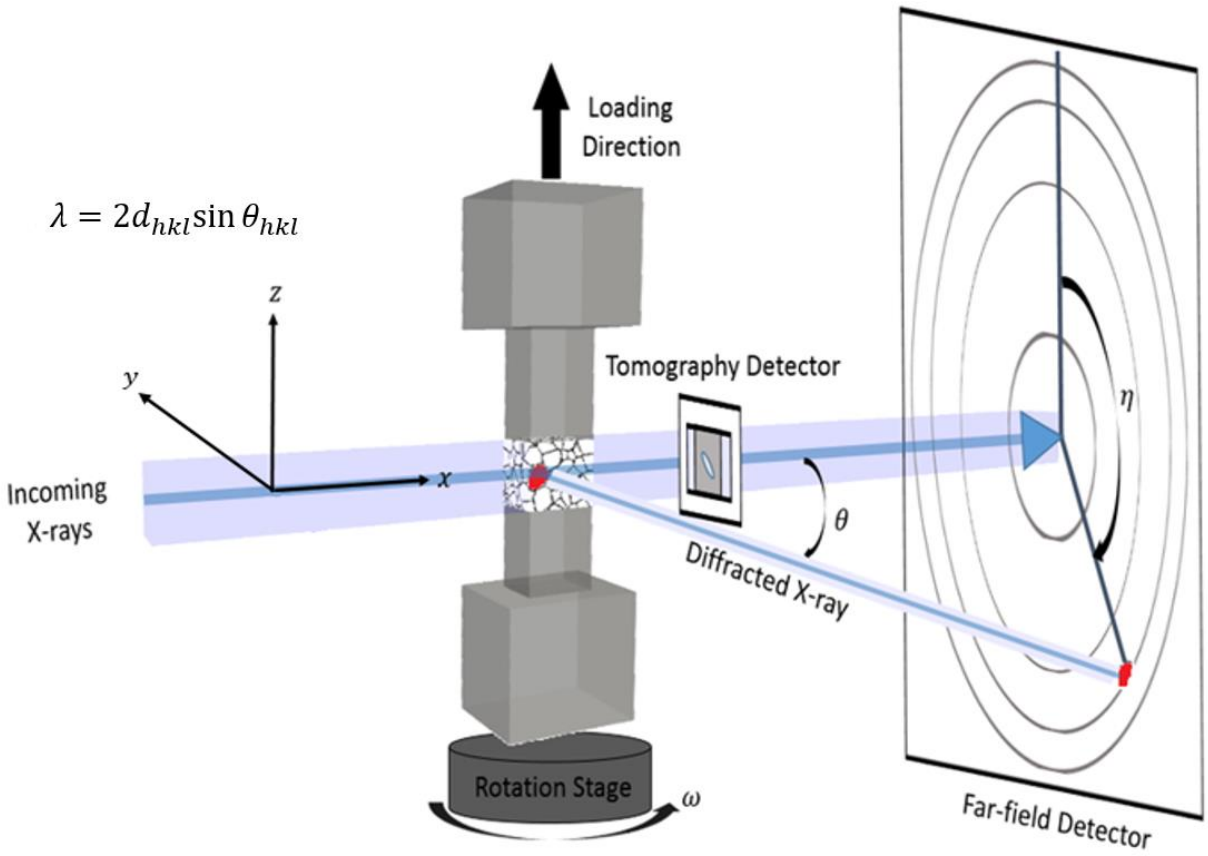

Figure 3.2 Schematic of the experimental setup at APS: 1-ID-E.

2. Reconstructing HEDM data relies on extracting the position of individual diffraction spots from the multitude of reflections originating from all the grains in the sample. Analyzing detector images for this purpose quickly becomes more difficult and time consuming as the volume probed increases. This is because as the number of grains illuminated and diffracting are increased, the possibility of multiple spots overlapping also increases, a problem that only worsens with spot spreading due to the applied deformation. Therefore, a 2 mm wide and 100 μm tall, X-ray beam was chosen in the present experiment. With this beam dimension, the diffraction patterns were assessed to have reasonably well separated spots. Since the crack initiation site could not be predicted in advance, we needed to probe the complete volume of

the sample containing the inclusion. To this end, it was necessary to take multiple scans to cover the desired volume, a total of 15 such scans were taken at each state to encompass the ~1300 μm tall inclusion with one 100 μm buffer on either end and no overlap between each scan volume.

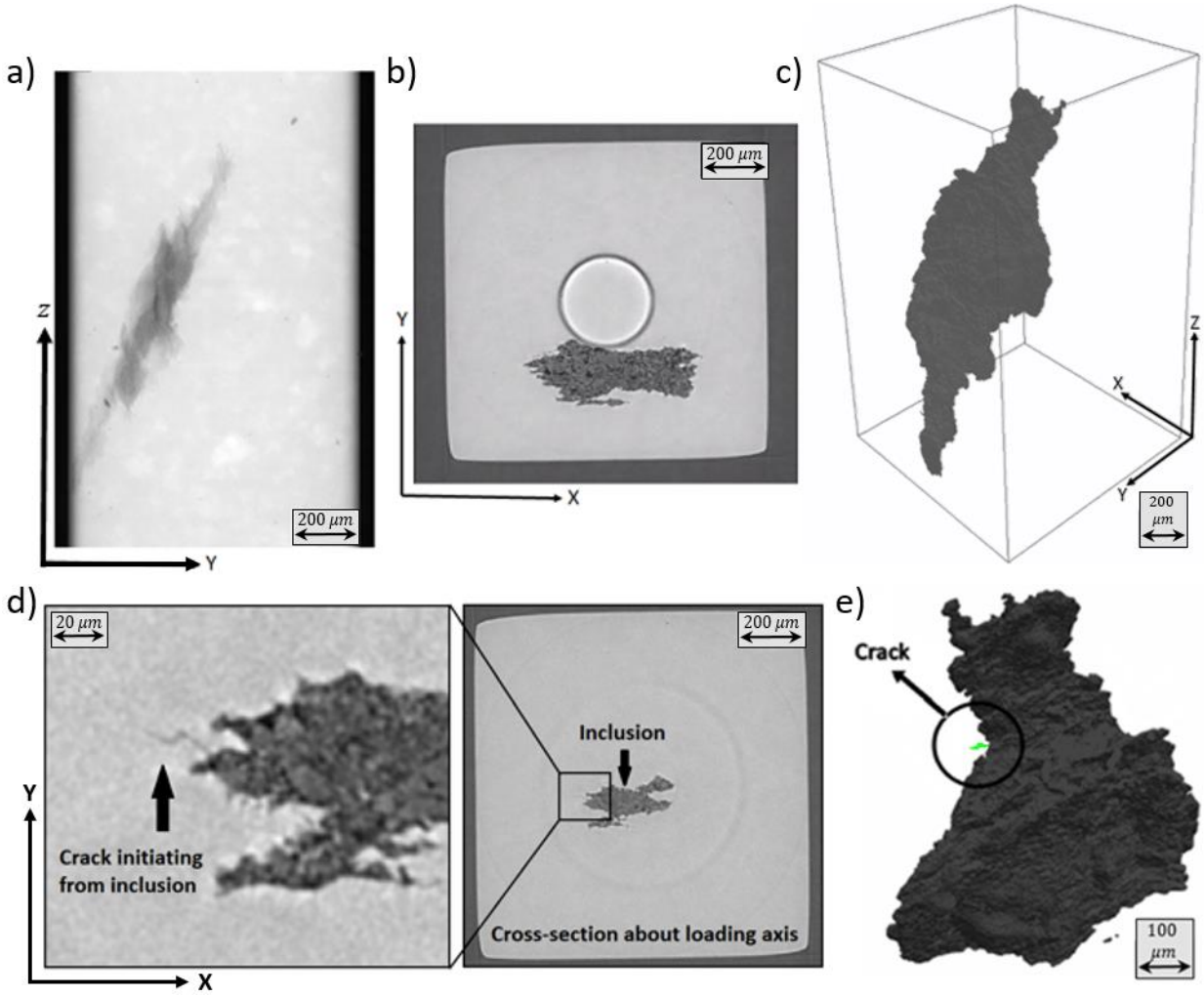

Figure 3.3 X-ray micro-computed tomography results, including a) radiograph displaying sample outline with embedded inclusion, b) reconstructed cross-section perpendicular to the loading direction, c) 3D rendering of the embedded inclusion, d) crack initiating at the matrix inclusion interface, and e) 3D rendering of crack juxtaposed to the inclusion.

A GE-41RT amorphous silicon flat panel detector [49] with a size of 2048 X 2048 pixels at a pixel pitch of 200 μm was employed. To extract strains from the grains to the desired resolution

of 1e-4 [53], the detector was placed at a distance of ~1 m from the sample. A suite of calibration images were obtained in the beginning and at the end of the experiment to determine the detector distance, tilts, and distortion parameters and check for any significant setup changes. From the sample, diffraction spots from five complete Debye-Scherrer rings ({111}, {020}, {220}, {131} and {222} planes) were captured on the detector at this distance. The sample was rotated along ω with 0.25° integration steps over a 360° angular range. To save time, scans during the minimum loading states within the fatigue experiment were conducted between omega (0, 180°) instead of omega (0, 360°). With the above setup a spatial resolution of ~20 μm for the grain centroid positions and angular resolution for crystallographic orientation within 0.1° was achievable. The lattice strain resolution was on the order of 1e-4.

With preliminary information from tomography, the maximum stress state for the test was set to ~60% of the yield strength of the matrix material determined from a similar sample with a large non-metallic inclusion seeded within the gauge section. The specimen was cyclically loaded under load control from zero to maximum load using the RAMS device and MTS load frame in laboratory air at room temperature at 1 Hz. In the beginning, the specimen was loaded to the maximum load value via 3 equi-spaced loading steps and both μ-CT and FF-HEDM scans were taken at each step. Following the first load-unload cycle the test was interrupted 3 times every decade (1, 2, 5, 10, 20, 50, 100 cycles …) and scans were taken only at zero and maximum load. The test was continued until crack initiation was observed. Details of the data captured for this experiment can be found in Fig. 3.4.

Dataset	Load	Cycle	Angle Range for HEDM	Tomography	Number of Grains found in 1 Layer
1	0	0	360	Yes	2148
2	200	0.33	360	Yes	2831
3	400	0.67	360	Yes	2281
4	600	1	360	Yes	2172
5	0	1.5	360	Yes	2156
6	600	2	360	Yes	2152
7	0	2.5	180	No	2134
8	600	5	360	Yes	2213
9	0	5.5	180	No	2192
10	600	10	360	Yes	2197
11	0	10.5	180	No	2159
12	600	20	360	Yes	2191
13	0	20.5	180	No	2171
14	600	50	360	Yes	2202
15	0	50.5	180	No	2156
16	600	100	360	Yes	2177
17	0	100.5	180	No	2140
18	600	200	360	Yes	2182
19	0	200.5	180	No	2132
20	600	500	360	Yes	2167
21	0	500.5	180	No	2134
22	600	1,000	360	Yes	2709
23	0	1,000.5	180	No	2605
24	600	2,000	360	Yes	2258
25	0	2,000.5	180	No	2228
26	600	5,000	360	Yes	2290
27	0	5,000.5	180	No	2220
28	600	10,000	360	Yes	2158
29	0	10,000.5	180	No	2234

Figure 3.4 Experimental details of characterization during interrupted cyclic loading. Note the number of grains found in the various datasets within the same illuminated volume changes slightly from scan to scan. This is due to fluctuations in illuminating X-ray flux and software reconstruction limits, among other things. Crack could be seen in tomography scans after 10,000 cycles.

3.5 Analysis methods and Results

3.5.1 High-energy X-ray computed micro-tomography

The immediate output of X-ray μ-CT data collection is a series of radiographs, which are basically projections of the sample on the tomography detector once X-rays pass through it. The radiographs show density contrasts in the sample as the X-rays are absorbed disparately by different parts of the sample. In Fig. 3.3(a), the contrast in a cross-section of the sample has been inverted to clearly show a tri-modal distribution of intensities representing the Ni-based superalloy

matrix with the brightest intensity, the alumina inclusion in the center of the sample, and the surrounding air.

It can immediately be inferred, in greater detail than that available with ultrasonic inspection, that a large inclusion is present in the sample, with a complex morphology. It is oriented at an inclination to the sample cross-section and more importantly to the loading direction, the effect of which will be discussed in the next section. The inclusion is broadest in cross-section at the center of the probed volume and tapers towards the ends. The top end is almost at the center of the sample's cross-section while the other end touches the free surface.

During the experiment this information was utilized to make quick calculations of the stress that the reduced cross-section of the Ni matrix would experience. Following the experiment, however, the μ-CT data was reconstructed using an in-house code of APS [38,39] based on the GridRec algorithm [40]. With unobstructed projections at 0.2° intervals for a complete 360° rotation of the sample, detailed reconstructions of the sample cross-sections were obtained. The effect of phase contrast could be observed from the reconstructions, an additional aspect of the setup that would help later with crack detection.

The reconstruction processes row after row of the radiographs, and so each cross-section of the sample is obtained as an image, as shown in Fig. 3.3(b). These images, after some image-processing to remove tomography artifacts like rings due to the detector imperfections (such as speckles or dust), can be stacked up to render the complete probed volume. In Fig. 3.3(c), an intensity filter was used to extract and depict in greater detail the spatial and morphological information of the inclusion in the sample. The rendering allows us to estimate that the inclusion was ~1300 μm tall along the tensile axis. Further details from the tomography reconstruction show the inclusion consists of an aggregate of small, yet tightly packed, particles.

Because of the nature of this technique and its resolution, a fine crack can only be seen in the sample when the crack is opened. Therefore, μ-CT scans were taken at maximum load every time cyclic loading was interrupted. Finally, in scans after 10,000 loading cycles, a small crack was observed in the cross-section shown in Fig. 3.3(d). A few details that warrant discussion at this point from Fig. 3.3(e) are that the crack did not initiate at the broadest cross-section of the inclusion. It also did not originate, as traditional thinking would suggest, at the sharpest features on the inclusion or where the inclusion is connected to the free surface of the specimen. It initiates at a fairly narrow cross-section of the sample towards the top of the probed volume, where the inclusion

is at the center of the cross-section. Hence, local microstructure details need to be obtained to explain the crack initiation event.

3.5.2 High energy X-ray diffraction microscopy

The second part of the experiment helped us in characterizing the microstructure surrounding the inclusion using high-energy X-ray diffraction. The initial calculations are performed using a pure Ni structure (FCC crystal structure, a=b=c=0.3524 nm, $\alpha=\beta=\gamma=90°$); but since the sample is an alloy of Ni this structure results in skewed mean grain strain in the loading direction at the unloaded state, when it should be centered around zero to ensure equilibrium at this state. The lattice constants were optimized to 0.3592 nm [84], a value at which the average grain strain in the loading direction was symmetrically distributed around zero.

The output of HEDM reconstruction (performed using Microstructural Imaging and Diffraction Analysis Software (MIDAS) developed at the APS [51,52]) is visualized in Fig. 3.5(a), where each box corresponds to an individual scan. In each layer, every single point of the scatter plot represents the center of mass position of a grain discovered in the scanned volume and has associated information about its orientation and strain state. The color of the scatter plot corresponds to the layer number, which ranges from 1 to 15. Approximately 2,500 grains were found in each layer, varying primarily due to the location of the layer and the space in it occupied by the inclusion.

A completeness threshold was set at 60% and any grain that did not meet this cut-off was not considered in the analysis that will follow. A completeness value is calculated as the ratio of measured to expected diffraction spots for a given crystal orientation and position. A value of one implies that all the spots that are expected to be found for the grain were measured. Using this value, we retain many of the smaller grains that are otherwise difficult to index with high confidence because they produce spots of weaker intensities. These low intensity spots are sometimes barely above the background and are systematically absent due to being either below the minimum threshold or overlapped by higher intensity spots from bigger grains. Since we are using five rings (116 expected spots) for indexing in this work, it still results in at least 70 spots indexed per grain. Most grains in the volume were above this threshold before loading. The completeness value worsens with deformation as the defects in the lattice results in spot spreading.

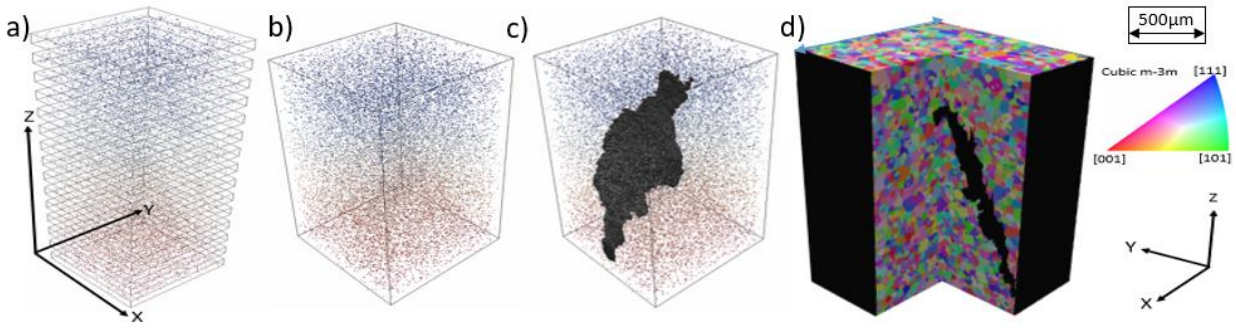

Figure 3.5 Far-field HEDM results, including a) scatter plots of 15 box scans across the region of interest, the color of the scatter plot corresponds to the layer number which ranges from 1 to 15, b) consolidated volume representing the region of interest, c) registering between the far-field HEDM results and tomography and d) rendering the complete microstructure (denoted with the inverse pole inverse pole figure color map), using Laguerre tessellations.

All the 15 layers can be stacked together as shown in Fig. 3.5(b) to create a consolidated volume, which can then be registered with the tomography results, as shown in Fig. 3.5(c) to render the complete sample volume. Almost 40,000 grains were found in the complete scanned volume. After indexing all the spots to a grain, the integrated intensity of the spot can be used to give an approximation of the grain volume. With this additional information provided by MIDAS, we can fill in the volume of the grains in the sample by performing Laguerre tessellations. This form of tessellation uses grain volume to weight the growth of a grain from its spatial center and thus results in a more accurate picture of the microstructure than obtained via regular tessellation (e.g. Voronoi) algorithms [85]. The tessellations were performed using DREAM3d [86] and can be seen in Fig. 3.5(d), where each grain is colored according to its orientation in the inverse pole figure format.

3.6 Discussion

3.6.1 Micromechanical evolution

In Fig. 3.6(a) we can see the grains color-coded according to their elastic strain component in the loading direction at maximum load after 10,000 cycles (representing the measurement after crack initiation was observed). Due to the small sizes of the crystallites forming the inclusion

aggregate it was not possible to reconstruct the grain-averaged strain in the inclusion. Thereby only the elastic strains in the Ni-based superalloy matrix are available and the inclusion is just colored for zero strains. In Fig. 3.6(a), we can clearly see the heterogeneity associated with the spread of strains in the grains surrounding the inclusion. Despite differences in orientation of adjacent grains, it can be seen that large regions of the microstructure have developed high strains upon loading while other neighborhoods happen to develop low strains. More discussion on the strain distribution will be pursued in the later sections. The amount of information in the full volume becomes too difficult to follow, so to simplify the analysis for the reader, we will be focusing on two specific cross-sections of the sample. In Fig. 3.6(b,d), we consider a cross-section of the sample perpendicular to the loading direction, specifically, a slice in which the longest part of the crack is observed. And in Fig. 3.6(c,e), we consider a vertical cross-section of the sample, in which the inclination of the inclusion is explicitly captured.

The lattice plane spacing for various atomic planes is the direct output of the HEDM analysis, which can then be used to calculate an elastic strain tensor, ε_{ij}^{e}. This information can be combined with the single crystal stiffness tensor, C_{ijkl}, to determine the corresponding stress, σ_{ij}, in each grain using Hooke's law:

$$\sigma_{kl} = C_{ijkl} : \varepsilon_{ij}^{e} \tag{3.1}$$

We can then use the average stress tensor within each grain to calculate all other commonly used damage variables and assess traditional failure metrics. In Fig. 3.6(b,c), we have plotted the stresses in the loading direction for each grain found during initial characterization of the sample right after gripping it. These are the residual stresses in the sample due to processing and, as shown, can be quite significant. The importance of residual stresses has long been understood, especially with respect to its influence on fatigue life. The 33-component of stress is highly compressive adjacent to the inclusion, while it is more tensile in the regions further away from the inclusion. Similar to the 33-component of stress, the directions transverse to loading, i.e. the 11 and 22 components of stress, also show the same kind of stress field distribution. To understand this distribution, we explore the manufacturing process, which involves powder consolidation at high temperature, followed by heat treatment processes to generate the desired microstructure. When we account for the lower thermal expansion coefficient of alumina (~ 6.6 ppm /°C) as compared to that of Ni (~13 ppm /°C) [87], upon cooling from the processing and heat treatment steps, the Ni matrix is contracting more than the inclusion, thereby forcing the matrix adjacent to the

inclusion into a compressive stress state. The outer regions are then in tension to maintain mechanical equilibrium.

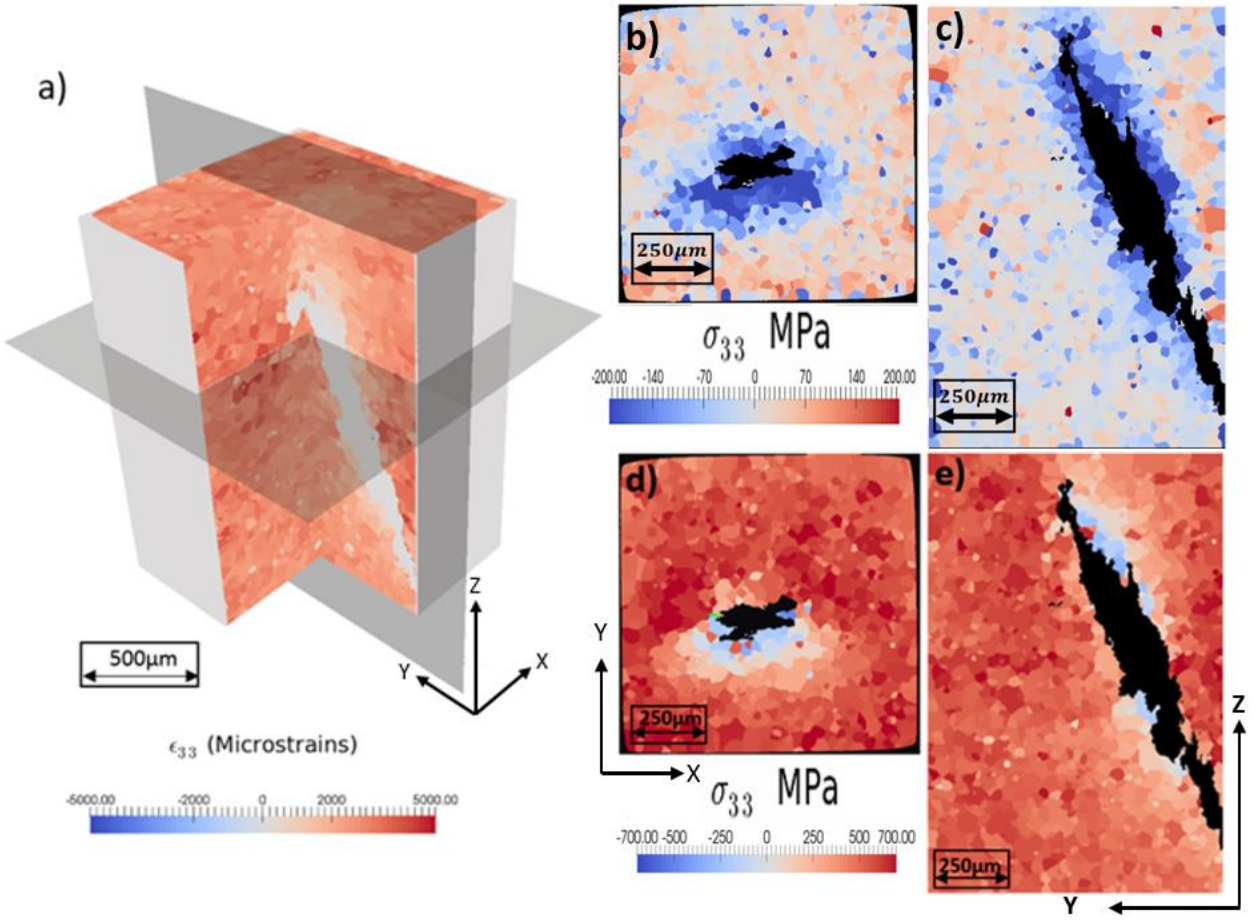

Figure 3.6 a) Micro-strains in the loading direction for the complete microstructure. The inclusion has not been colored because strain information is absent. Cross-section perpendicular to the applied loading in which the crack is present (b,d), and cross-section capturing the inclination of the inclusion (c,e) with respect to the loading direction, have been colored according to stresses found at initial characterization (b,c) and stresses after experiment (d,e), all stresses are in the loading direction.

In Fig. 3.6(d, e) the stresses in the loading direction are plotted for each grain at the end of the experiment. This state corresponds to cycle 10,000 at peak load. Before making further comments about the stress distribution, we want to explore the other states for which data was collected and understand the evolution of stresses till this point. In Fig. 3.7 (a-d), various failure metrics are plotted including a) strain component in the loading direction, b) stress component in the loading

direction, c) maximum principal stress and d) von Mises effective stress. A complete summary of the failure metrics is given in the Supplementary A. The trends in the plot that follow can be summarized through 5 of the 30 loading states that were captured. The first column corresponds to the reference/initial state of the microstructure, once the sample was gripped and before loading commenced. The load up to a maximum value of 600 MPa corresponds to column 2. Columns 3, 4 and 5 represent scans after cycles 2,000, 5,000 and 10,000 at maximum load of 600 MPa.

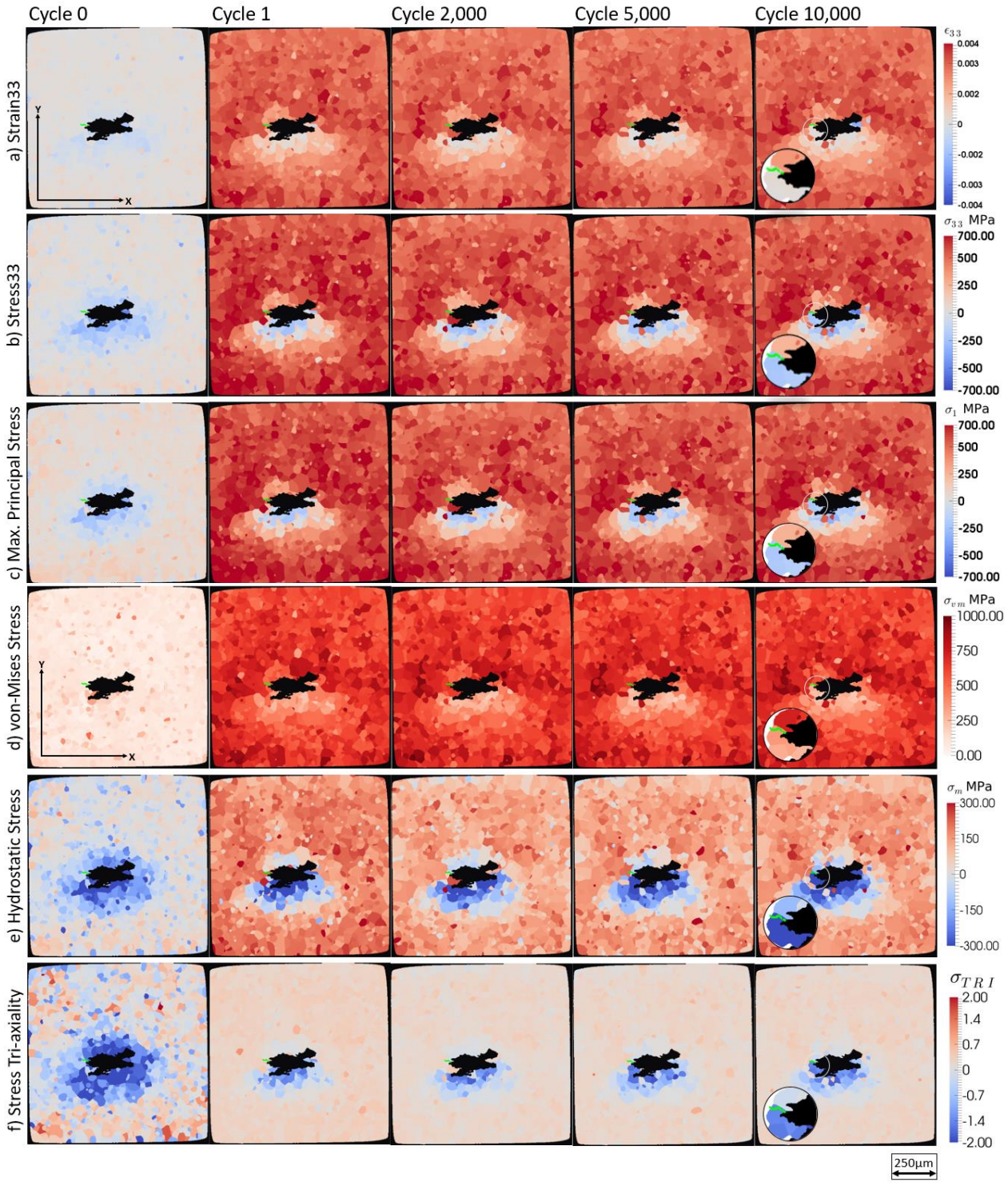

Figure 3.7 Cross-section perpendicular to the loading direction with a spatial map of a) elastic strain component about the loading direction, b) stress component in the loading direction, c) maximum principal stress, d) von Mises stress, e) hydrostatic stress, f) stress triaxiality. The left to right columns correspond to different loading states. The leftmost column, Cycle 0, was collected at 0 MPa. All other loading states were collected at 600 MPa.

Fig 3.7 continued

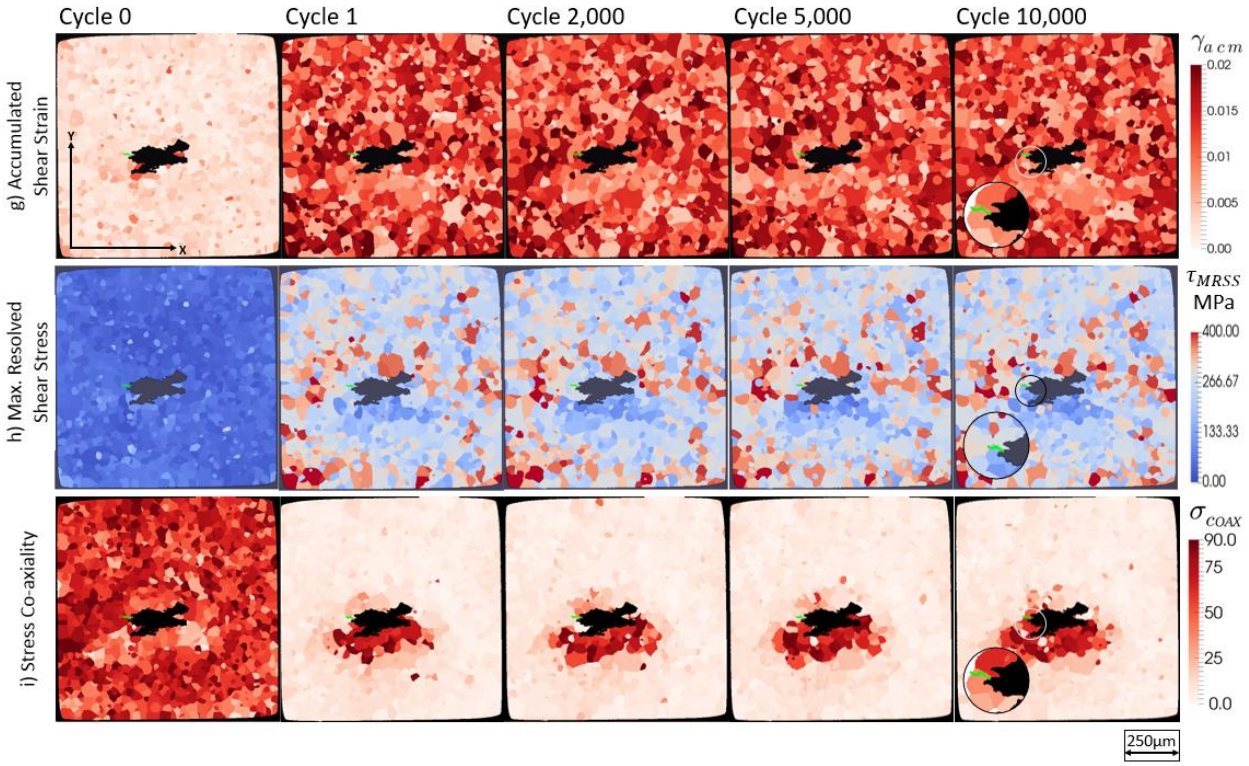

Fig 3.7 Cross-section perpendicular to the loading direction with a spatial map of g) accumulated elastic shear strain (summed over the slip systems), h) maximum resolved shear stress, and i) stress co-axiality. The left to right columns correspond to different loading states. The leftmost column, Cycle 0, was collected at 0 MPa. All other loading states were collected at 600 MPa.

The failure metrics considered in this study are summarized in Table 1 as follows:

Table 3.1 Summary of the names, equations, and image locations of the associated failure metrics employed in this study.

Name	***Failure Metric***	***Corresponding Figure Number***
Strain 33	ε_{ij}^{e}	Fig. 3.7a
Stress 33	$\sigma_{kl} = C_{ijkl} : \varepsilon_{ij}^{e}$	Fig. 3.7b
Maximum Principal Stress	$max.\, eigen\ value\ \lambda_1\ where\ \lvert\sigma_{ij} - \lambda\delta_{ij}\rvert = 0$	Fig. 3.7c
Von-Mises Stress	$\sigma_{vm} = \sqrt{\frac{3}{2}\sigma^{dev} : \sigma^{dev}}$, where stress deviator tensor, $\sigma_{ij}^{dev} = \sigma_{ij} - \frac{\sigma_{kk}}{3}$	Fig. 3.7d
Hydrostatic Stress	$\sigma_m = \frac{\sigma_{kk}}{3}$	Fig. 3.7e
Stress Tri-axiality	$\sigma_{TRI} = \frac{\sigma_m}{\sigma_{vm}}$	Fig. 3.7f
Accumulated Shear Strain	$\sum\lvert m_i n_j \varepsilon_{ij}^{e,crystal}\rvert$, where slip plane normal: m_i and slip direction: n_j	Fig. 3.7g
Maximum Resolved Shear stress	$MRSS = max(\ \lvert\tau^{mn}\rvert\ ) =$ $\max(\lvert m_i n_j \sigma_{ij}^{crystal}\rvert)$, where slip plane normal: m_i and slip direction: n_j	Fig. 3.7h
Stress Co-axiality	$COAX\ \angle = cos^{-1}\left(\frac{\sigma_{macroscopic} : \sigma_{grain}}{\lVert\sigma_{macroscopic}\rVert\lVert\sigma_{grain}\rVert}\right)$	Fig. 3.7i

It can be seen that two separate regions in terms of strain magnitudes are seen to form as soon as the sample is loaded in tension; most of the sample is high in strain/stress with expected local variations due to the microstructure, however, there is also a small region right below the inclusion, which can be associated in all four plots with low or negative strain/stress values. As highlighted in Fig 3.3(d), the location of the crack was drawn into the micromechanical plots in Fig. 3.7 to aid in visualization. After the initial state, the strain/stress distribution in the sample saturates quickly, within a few cycles and remains almost the same until maximum load in load cycle 2000, shown in column 3. The subtle changes in the plots can be associated to the fact that each state has been tessellated from a separate FF-HEDM reconstruction that alters the grain boundaries very slightly. Load cycle 5,000 corresponds to the data point captured right before the crack was observed in the sample and load cycle 10,000 corresponds to the scan after the crack was detected. After cycle

2,000, the region below the inclusion with low or negative strain/stress values starts growing left towards the location of crack initiation. These changes are large enough to not be shadowed by grain boundary changes between different tessellated states. At cycle 10,000 the regions of high and low strain are separated right at the crack with grains on either side of the crack at completely different strain states (shown clearly in the magnification).

Gradients between adjacent regions of high and low stress values have been cited as a precursor for crack initiation [88]. To assess this possibility in the present experiment, we plot the hydrostatic stresses (Fig. 3.7(e)) and stress tri-axiality (Fig. 3.7(f)), which is the ratio between the hydrostatic and von Mises stress. The von Mises stress distribution is responsible for shape change, while the hydrostatic stress is a measure of the volume change. It can be seen that the region right below the inclusion has very low von Mises stresses and low hydrostatic stresses, which implies that this region is almost elastically loaded. While in the region right above the crack, the von Mises stresses are high, which indicates plastic deformation or dislocation motion in this region. The tri-axiality plots show how there are two adjacent grains at the location where the crack initiated, across the stress gradient - one grain indicates a state of plastic deformation and the adjacent grain has low elastic strains. This grain configuration is susceptible to dislocations impinging upon the grain boundary and resulting in a pile-up, thus providing a driving force for crack initiation. Next, we aim to determine why such conditions were created at a particular location in the sample.

The elastic strain on each grain is resolved onto the slip systems and the sum of the elastic shear strain across each slip system is shown in Fig. 3.7(g). Similarly, in Fig. 3.7(h), the stress on each grain is resolved onto individual slip systems, based on the orientation of each grain, and the maximum resolved shear stress among all the slip systems is plotted. The critical resolved shear stress for this material [89] is plotted as white in the colorbar in Fig. 3.7(h), hence grains that have plasticized are shown in red and grains remaining elastic are in blue. These plots take into account the stress/strain state within each grain and also factors in the orientation of the grain in the sample. They show that there is a very heterogeneous spread in deformation, not only due to the orientation of the grains, but also due to the elastic and plastic anisotropies of the respective neighborhoods. The only conclusive remark that can be made is on how the grains directly below the inclusion are elastically loaded. The sample consists of a large alumina inclusion. The strain state of the microstructure within the sample is affected by the orientation of the inclusion in this sample. Consider the co-axiality plots in Fig. 3.7(i), which is defined as follows [90–92]:

$$Coaxiality\ angle = cos^{-1}\left(\frac{\sigma_{macroscopic}:\sigma_{grain}}{\|\sigma_{macroscopic}\|\|\sigma_{grain}\|}\right) \quad (3.2)$$

The plot shows how the region directly below the inclusion, in this cross-section, is loaded perpendicular to the macroscopic loading direction. Thus, this region is in a totally different stress state, one potential explanation is the inclination of the large inclusion in the specimen resulted in macroscopic bending, which is investigated in the next section.

3.6.2 Simulations

The final stress state of the microstructure is due to a combination of factors, including the orientation of the inclusion, residual stress state, and decohesion. A simple 3-D EVP-FFT simulation was performed on the volume of the sample, as characterized by the experiment shown in Fig. 3.5(d). The description of the EVP-FFT formulation is discussed in detail in ref [65] and the relevant constitutive equations are briefly presented in Supplementary B. In this case, the model is used to investigate the effect and contribution of each of the aforementioned factors (orientation of the inclusion, residual stress state, and decohesion) on the resulting micromechanical fields.

The volume was loaded vertically in tension (along the z-direction) to the maximum macroscopic strain levels observed in the experiment, thereby the displacement boundary conditions were prescribed in the z-direction (and were free elsewhere, i.e. not explicitly prescribed in the other directions) for a single monotonic loading path. The Ni-based superalloy was prescribed elastic and plastic parameters by creating a statistically equivalent microstructure (without an inclusion) and fitting to RR1000 tensile test data. The inclusion was prescribed the elastic properties of alumina [93], and due to the inclusion's structure as revealed by phase contrast tomography, was assumed to be elastically loaded. The critical resolved shear stress of the alumina phase was set to a high value, so that in effect the inclusion was loaded elastically. One advantage of the EVP-FFT simulation is it offers a spectral method, whereas the spatial material points obtained by tessellating the FF-HEDM results of the RR1000 consolidated with micro-tomography results of the inclusion can be directly used as input into the simulations.

The perimeter of the volume in the directions perpendicular to loading had a buffer of a dummy/gas phase (all associated properties/values are zero) such that the simulated region could be periodically repeated in all three directions to satisfy the EVP-FFT boundary conditions. The padding ensured the periodic boundary conditions would not influence the micromechanical fields

in the region of interest. For a strain increment of 0.33e-4 per time step, the simulations initially converged after ~20 iterations and afterwards reached convergence after ~13 iterations. The simulation reached the desired macroscopic strain value in ~80 steps. The results can be seen in Fig. 3.8(a, e), the stresses in the loading direction have been plotted and it is fairly homogenous throughout the sample. The local variations are small and are not visible with the chosen color scale compared to large inhomogeneity illustrated in Fig. 3.8(d, h). To understand the difference, we need to look at the effect of decohesion and residual stresses.

Inclusion decohesion from the matrix has been discussed in literature as an effect of loading [94] and an immediate precursor to crack initiation [11,82]. Here we propose decohesion as an initial state before loading has begun due to processing. It has been reported previously how the partially bonded state of the inclusion causes the worst possible stress concentrations [94–96]. To determine where the inclusion was initially debonded, we used the HEDM strain distribution after loading. It was hypothesized that regions with low or no strain were a product of prior debonding, since this represents a traction free boundary and therefore load cannot be transferred from the matrix.

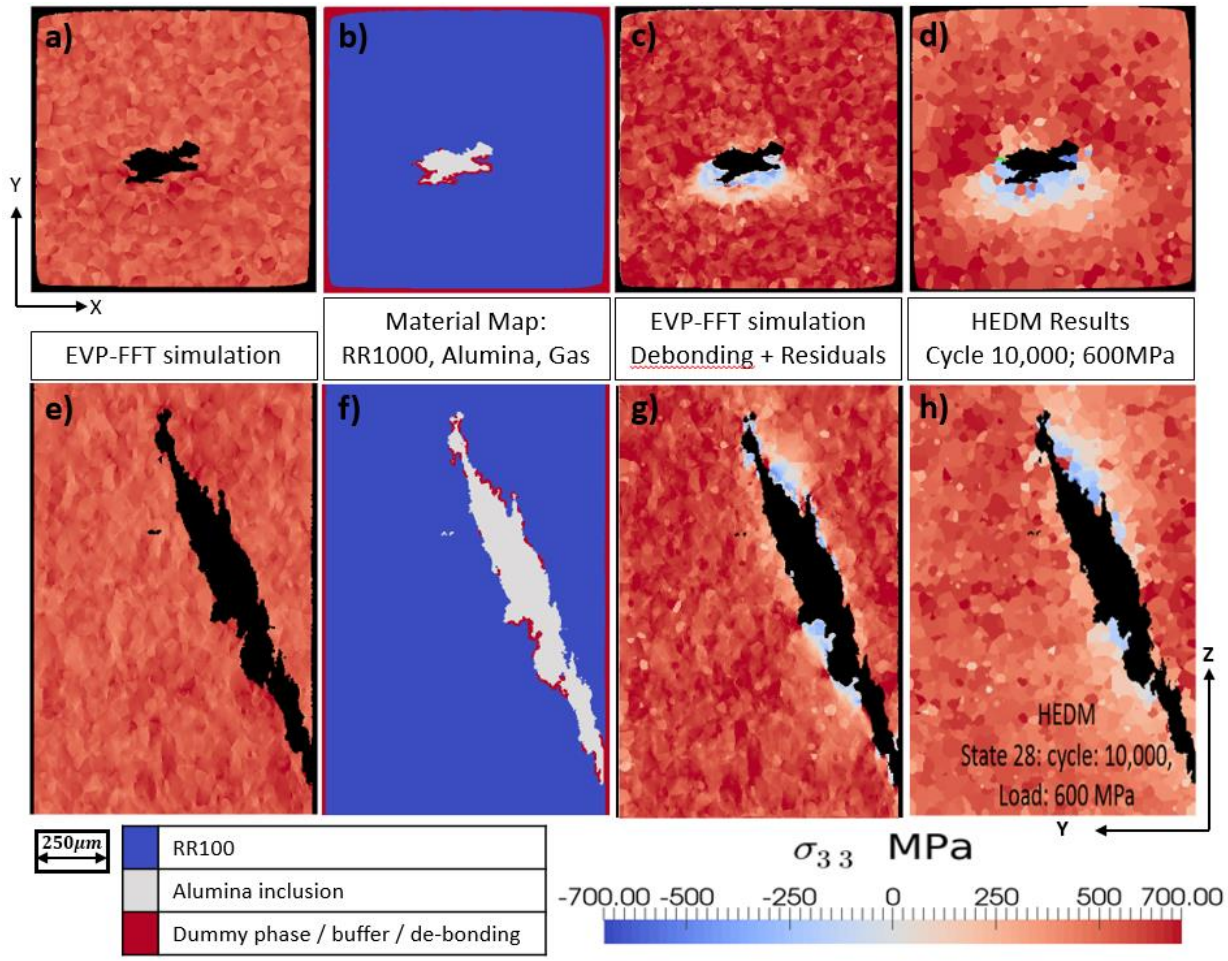

Figure 3.8 Stress component in loading direction via a) and e) EVP-FFT simulation to study effect of inclination of the inclusion, b) and f) Material maps used in the EVP-FFT simulation depicting location of de-bonding (highlighted in red) in the sample determined based on the HEDM results, c) and g) EVP-FFT simulation results of the partially bonded inclusion superimposed with residual stresses, d) and h) HEDM at peak load after 10,000 cycles of loading. Top row (a, b, c, d) correspond to cross-section perpendicular to loading direction; bottom row (e, f, g, h) correspond to a cross-section parallel to loading direction. The legend for the material can be associated with (b, f) and the color map for σ_{33} corresponds to the rest of the plots.

To recreate this effect, the boundary voxels were cached and then the strain at every voxel was determined based on the associated grain in the tessellation. All voxels located at the inclusion-matrix interface below a certain threshold in strain were considered to be debonded and were assigned high compliance properties, i.e. they were treated as a gas phase (all associated properties/values are zero). The selection has been shown in Fig. 3.8(b, f). An EVP-FFT

simulation with 3 phases corresponding to the Ni matrix, alumina inclusion and the debonded interface voxels was performed. This residual stress state plays a significant role in creating the initial stress state of the sample, which is traditionally not included in the simulation. It should be noted that the grain averaged residual stresses, determined via FF-HEDM, cannot be readily used to initialize the EVP-FFT simulations. Some implementations [97] ensure equilibrium in the simulation is not violated, due to an initialization method, but these are beyond the scope of the current work. Therefore, to understand the effect and role of residual stresses, they have been superimposed on the final results after loading.

This addition of a partially bonded inclusion immediately creates stress concentrations in the EVP-FFT results that correspond very closely to the HEDM results. Finally, the combined effect of the orientation of the inclusion, the residual stress state and de-cohesion at the matrix-inclusion interface can be seen in Fig. 3.8(g, h). These results are extremely close, qualitatively, to experimental HEDM results (Fig. 3.8(d)) and thereby the three aforementioned factors are collectively asserted to cause the stress gradient at the location in which the crack initiated.

3.7 Summary and Conclusions

Crack initiation at inclusions is a dominant and unavoidable failure mechanism in Ni-based superalloys, effectively comprising the ‘weakest link’ to component lifetimes. In this study we employed a pair of techniques, based on high energy synchrotron X-ray radiation that allowed us to track the evolving microstructure and micromechanical state in a sample of a Ni-based superalloy, with a deliberately seeded alumina inclusion, subject to cyclic uniaxial deformation. The initial characterization of the sample was performed using absorption contrast μ-CT to determine the spatial and morphological information about the inclusion. FF-HEDM was also performed to map the microstructure surrounding the inclusion, including the orientations and 3-D intergranular strain states of each grain. The cyclic loading was sequentially interrupted to conduct HEDM scans to elucidate temporal and spatial strain evolution in the grains, while also collecting μ-CT scan to determine when, and more importantly where, the crack initiated.

Spatially, the heterogeneity in strain/stress distribution is a product of a large rigid inclusion at an inclination to the loading axis and the residual state that it induces in the surrounding matrix. Temporally, the strains grow gradually with loading and stabilize very quickly in a few cycles, only to change locally upon crack initiation. The study reveals that a gradient exists in the

magnitude of strain across the crack initiation site, a trend that is consistent across other micromechanical fields. This gradient creates the necessary conditions for a crack to initiate.

Debonding at the inclusion-matrix interface is established to play the pivotal role in creating a gradient in stresses; the hypothesis of debonding has been inferred through proof of principle 3-D EVP-FFT simulations. It is noteworthy that the partially debonded inclusion and the associated residual stress state created a large stress gradient within the matrix, which resulted in crack initiation at the location. This phenomenon is demonstrated for a large inclusion within a matrix, but the mechanism is qualitatively applicable to the general case of inclusion driven crack initiation and could only be captured and measured by employing a combination of HEDM and μ-CT techniques.

4. X-RAY CHARACTERIZATION OF THE MICROMECHANICAL RESPONSE AHEAD OF A PROPAGATING SHORT FATIGUE CRACK IN A NI-BASED SUPERALLOY

A complete description of the chapter can be found in:
D. Naragani, P.A. Shade, P. Kenesei, H. Sharma, M.D. Sangid, X-ray characterization of the micromechanical response ahead of a propagating short fatigue crack in a Ni-based superalloy, (2019) under review.

4.1 Chapter Abstract

The short fatigue crack (SFC) growth regime in polycrystalline alloys is complex due to the heterogeneity in the local micromechanical fields, which result in high variability in crack propagation directions and growth rates. In this study, we employ a suite of techniques, based on high-energy synchrotron-based X-ray experiments that allow us to track a nucleated crack, propagating through the bulk of a Ni-based superalloy specimen during cyclic loading. Absorption contrast tomography is used to resolve the intricate 3D crack morphology and spatial position of the crack front. Initial near-field high-energy X-ray diffraction microscopy (HEDM) is used for high-resolution characterization of the grain structure, elucidating grain orientations, shapes, and boundaries. Cyclic loading is periodically interrupted to conduct far-field HEDM to determine the centroid position, average orientation, and average lattice strain tensor for each grain within the volume of interest. Reciprocal space analysis is used to further examine the deformation state of grains that plasticize in the vicinity of the crack. Analysis of the local micromechanical state in the grains ahead of the crack front are used to rationalize the advancing short crack path and growth rate. Specifically, the most active slip system in a grain, determined by the maximum resolved shear stress, aligns with the crack growth direction; and the degree of microplasticity ahead of the crack tip helps to identify directions for potential occurrences of crack arrest or propagation. The findings suggest that both the slip system level stresses and microplasticity events within grains are necessary to get a complete description of the SFC progression. Further, this detailed dataset, produced by a suite of X-ray characterization techniques, can provide the necessary validation, at the appropriate length-scale, for SFC models.

4.2 Introduction

The high variability in growth rates and propagation path of short fatigue cracks (SFC) was discussed by Pearson in 1975 [15] and has since been the focus of several reviews [16–19]. The behavior of SFCs still remains elusive, because very few experimental datasets have been able to capture the heterogeneity associated with the local micromechanical state ahead of the crack front in the bulk of a polycrystalline material under cyclic loading. Existing theories and models cannot be accepted into practice until their underpinning assumptions are assessed and appraised with detailed experimental data at the appropriate length scale. In this study, we leverage the advent of synchrotron based X-ray characterization techniques, developed in the past decade, to gather relevant micromechanical descriptors at the grain scale, in order to provide a physical basis to our understanding of the SFC regime.

In the past, researchers have focused on adapting classical approaches, including linear elastic fracture mechanics, elastic plastic fracture mechanics, or similitude concepts, through additional terms fit via empiricism in an attempt to capture the behavior of the SFC regime [25,98–101]. A unified theory to reconcile the regimes of long and short cracks has not been identified, which is most likely attributed to the fact that, in the SFC regime, several fundamental assumptions pertaining to long crack theories and the associated continuum descriptors are violated [102–104]. Since, a stress intensity factor is not applicable in the SFC regime, researchers have started to query the stress state in the grains ahead of the propagating crack, albeit without experimental measurements, these approaches have been primarily contained to the modeling communities. In this paper, the relevance of these stress-based metrics is interrogated at the grain scale with respect to the propagating crack.

Past experimental studies have focused on only a limited number of factors which affect the nature of SFC response in polycrystalline alloys. Studies that use electron microscopy, fractography or high resolution tomography are useful at extracting the crack path morphology [105–107]. Microstructural attributes, such as grain orientations [22,23], grains sizes [24,25], distance from obstacles like grain boundaries [26–28], and local neighborhoods [29,30], are known to affect SFC. Studies that use electron backscatter diffraction and focused ion beam [108–110], diffraction contrast tomography [111], and near-field HEDM [112,113] are able to elucidate the grain structure around the SFC. Interferometry [114], digital volume correlation [115], and 3D X-ray diffraction [116] are useful at determining the stress state or plasticity ahead of the SFC front.

In many studies, the experiments are limited to surface observations, without the ability to resolve the microstructure or the stresses at the crack front. Sometimes, they are constrained to post-mortem observations and analysis. The SFC problem is 3D in nature, and due to the cyclic loading, the micromechanical state ahead of the crack tip is dynamic and evolving with number of cycles and the corresponding grain neighborhood around the crack tip. Hence, it is necessary to capture, concurrently, the sub surface orientation of a propagating SFC with respect to the grain structure and the micromechanical state surrounding it, during in-situ cyclic loading, which has not been reported in literature to date. In this study, we employ multiple pertinent X-ray characterization techniques, concurrently, to determine the grain structure and complete micromechanical state ahead of an evolving SFC. Please see the schematic in Fig. 4.1 for an overview of the techniques used, which have been described in detail in later sections.

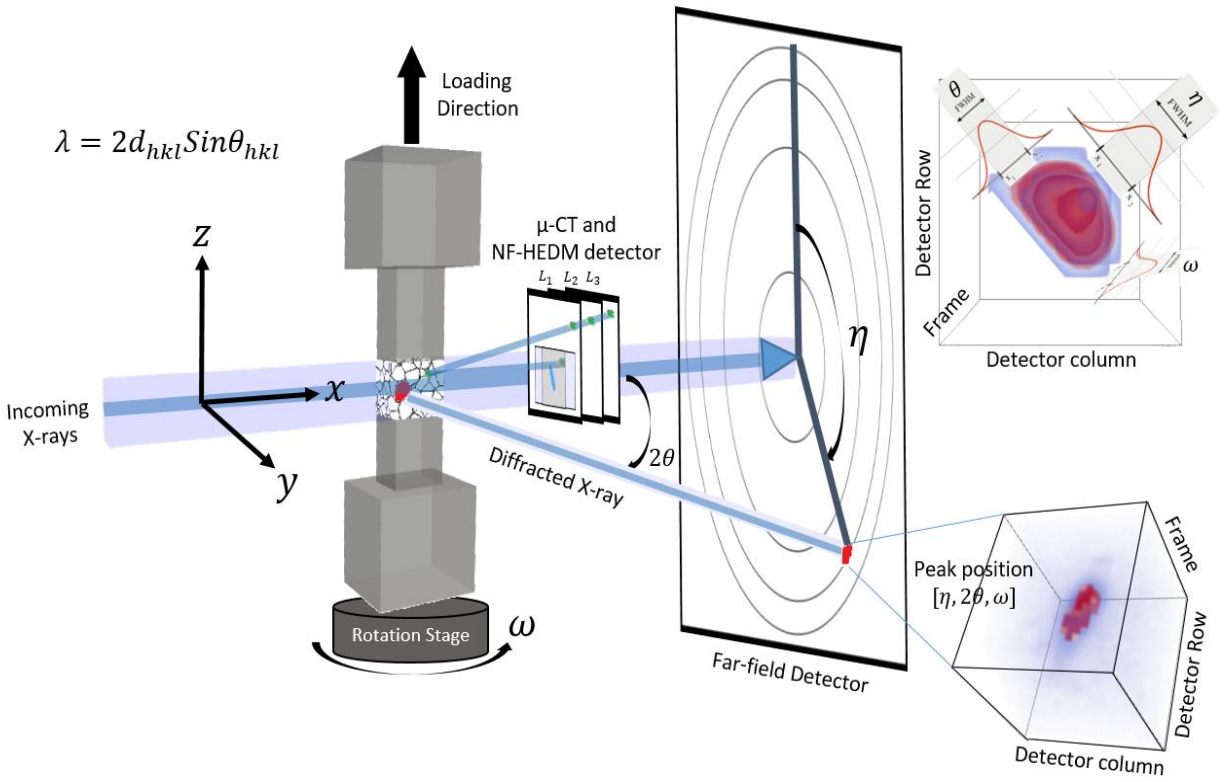

Figure 4.1 Schematic of the experimental setup featuring a suite of X-ray characterization techniques which include μ-CT, NF-HEDM, FF-HEDM, and reciprocal space mapping.

Current state of the art modeling efforts are based on 3D representations of the microstructure and resulting micromechanical fields and employ a crystal plasticity approach [117–121] [122], which relies on the assumption of a crystallographic dependency of the crack growth path in the SFC regime. In the past, crack propagation has been described theoretically as a slip-mediated process [123–125], advocating the importance of a slip system level analysis. Several crack driving forces are described in terms of the resolved shear stresses [126] on slip systems and normal stresses on the critical plane [127,128]. These theories and formulations have to be corroborated through experimental observations. In this study, we determine the relationship between the plane and direction, in which SFCs propagate with respect to the underpinning crystallography and explore the dependence of the growth rate on the maximum resolved shear stress and normal stress.

Past researchers have focused on the deformation at the crack front, through measures like crack tip plasticity [102], strain energy [129], stored energy [117], dissipated energy [130], irreversibilities at the crack tip [88,131], and crack tip opening displacements [132], to identify the crack path. When the crack size is small, on the order of the grain size, the entire plastic zone may be confined within a single grain [28]. Previous work has suggested a correlation of deceleration and potential arrest in the crack growth with localized micro-plasticity [133]. The aforementioned measures are surrogates for micro-plasticity, which results in lattice deformation within the grains. This deformation, to the ordered lattice within the grain, presents curvature in the lattice and a spread in lattice strains, both of which can be captured via reciprocal space mapping of X-ray diffraction spots [134]. In this study, we calculate and associate these measures to crack growth in specific directions along the crack front.

The paper is broadly divided into two main parts, in Sections 4.3-4.5 the experimental methodology behind the concurrent, in-situ cyclic loading and different modalities of X-ray characterization is elaborated. These include absorption contrast micro-computed tomography (μ-CT), near-field high-energy X-ray diffraction microscopy (NF-HEDM), far-field high-energy X-ray diffraction microscopy (FF-HEDM), and reciprocal space mapping scans. The registration, between these techniques, through different cyclic loading states, is described in detail. In Section 4.6, we discuss the evolution of the pertinent micromechanical stress-based descriptors and their relevance with respect to crack progression. A few representative grains are extracted and discussed in further detail to determine the crystallographic nature of the SFC behavior, by determining the crack alignment with respect to the well-defined slip systems. The critical slip

system, in each grain, is determined based on the stress state and the role of the associated normal and resolved shear stress on the crack growth rate is discussed. Finally, the evolution of the principal stresses and the resulting plasticity in the form of the lattice deformation within the grains ahead of the crack front are explored to understand their role in determining the SFC growth direction.

4.3 Materials and in-situ fatigue crack growth

In this study, a polycrystalline Ni-based superalloy, RR1000, produced via a powder metallurgy (PM) process by Rolls-Royce plc has been used. The material was seeded with Alumina particles, in order to investigate the role of non-metallic inclusions on fatigue crack initiation, as discussed in a previous study [67]. The material underwent an isothermal forging followed by a super-solvus heat treatment and two-step aging process to allow static recrystallization and grain growth [81]. The results produced a coarse grain variant of RR1000, with a face centered cubic (FCC) crystal structure with lattice constant, calibrated in a previous study [67], of 0.3592 nm and a nominal grain size of 23-32 μm. The composition and details of the manufacturing process are described in detail by Buckingham et al. in [81]. The material's random texture and equiaxed grain structure results in sharp and distinct diffraction spots making it an ideal candidate for high-energy X-ray diffraction microscopy experiments.

Ultrasonic inspection was used to detect inclusions in the material and a sample was machined around a given inclusion using electrical discharge machining. In this manner, an alumina inclusion, which is larger than typically observed but is still found in Ni-based superalloys [82], was extracted in the specimen gauge section as shown in Fig. 4.2 (a). The specimen was manufactured with a 1 mm X 1 mm cross-section and 8 mm gauge length for the X-ray characterization experiments. The specimen and grip design were compatible with the rotational and axial motion system [135], which serves as an insert in a servo-hydraulic MTS load frame to facilitate, with a high degree of accuracy and precision, motion control during in-situ X-ray experiments.

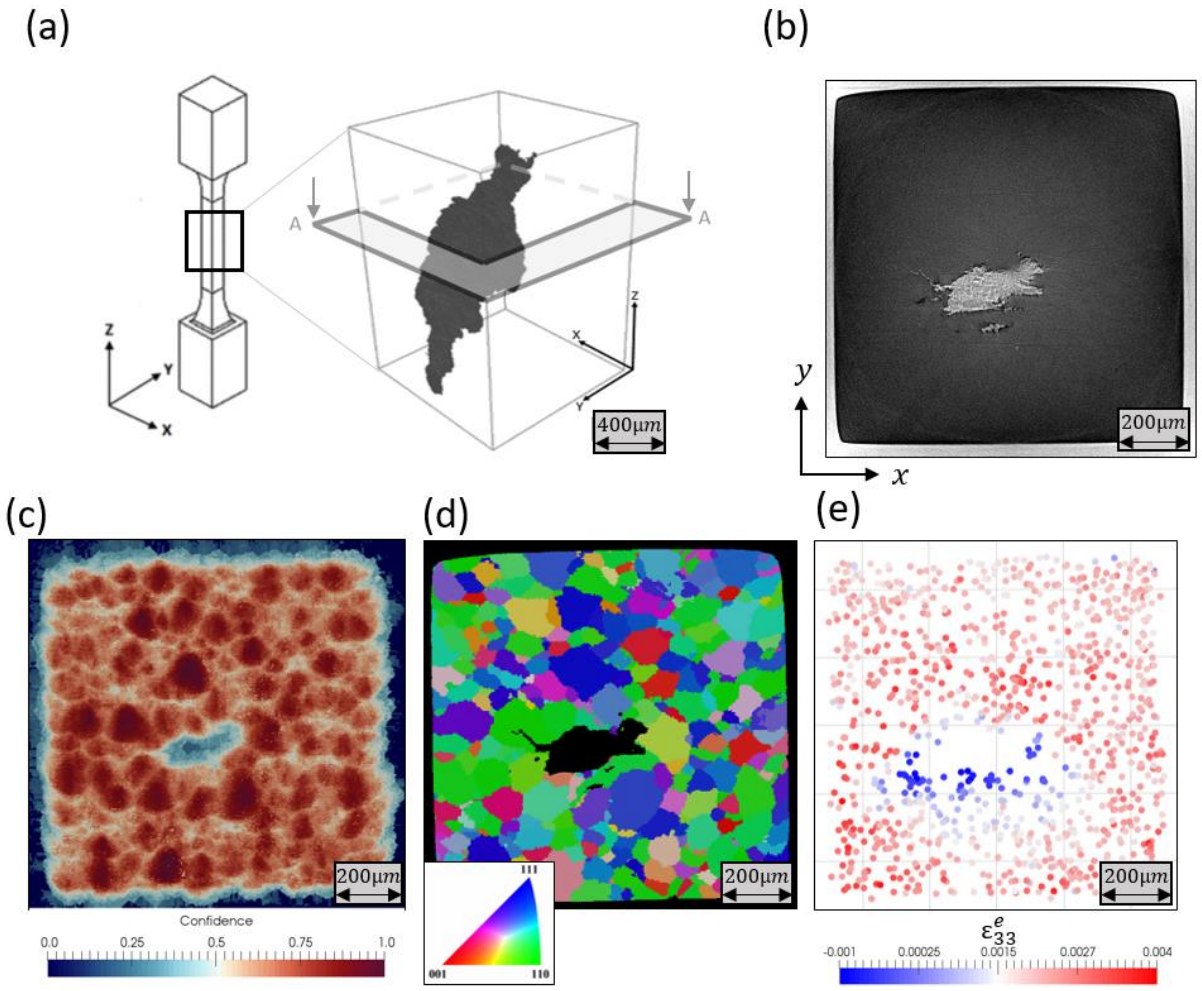

Figure 4.2 (a) Specimen geometry in region of interest with highlighted cross-section showing, (b) the reconstructed μ-CT image, (c) the confidence maps from the NF-HEDM reconstruction, (d) the grain map after registration with μ-CT results, and (e) the grain centroid positions showing distribution of elastic strains in the loading direction obtained from the FF-HEDM results.

This specimen was cyclically loaded in the MTS load frame under load control. The specimen was cycled between a lower bound of -0 MPa and a maximum stress, set to 60% of the yield stress for RR1000. The experiment was performed in laboratory air at room temperature and a loading frequency of 1 Hz. In a previous study by the authors [67], cyclic loading was performed on this sample, until crack initiation was captured. After 10,000 cycles of loading, a crack initiated from the matrix-inclusion interface. A gradient detected in the magnitude of the elastic strain field was responsible for the incipient crack initiation. This gradient was pronounced in the other analyzed micromechanical fields, particularly the stress triaxiality. The gradient was generated, primarily,

due to partial de-bonding at the local matrix-inclusion interface, as well as the residual stresses in the grains surrounding the inclusion, and the geometry of the inclusion (inclination to the loading axis, size, and morphology).

In this study, the naturally initiated crack from the matrix-inclusion interface located in the bulk of the specimen, was grown through the early stages of fatigue crack growth, known as the SFC regime. The same cyclic loading conditions were followed and loading was periodically stopped after small intervals to capture the progress of the crack. The corresponding developments in the local micromechanical fields were captured through X-ray characterization scans, which were taken during these interruptions. During these pauses, the sample was held at the prescribed maximum load. Scans were taken at ten states corresponding to 20,000; 21,000; 23,000; 26,000; 30,000; 36,000; 38,000; 41,000; 45,000; and 52,000 total cycles, respectively.

4.4 X-ray characterization setup

The experimental setup used during the X-ray characterization experiment with in-situ loading has been described through the schematic in Fig. 4.1. The experiment was performed inside the 1-ID-E end station of the Advanced Photon Source. A monochromatic X-ray beam at the Yb K-edge corresponding to an energy, E: 61.332 keV and wavelength, λ: 0.20215 Å was selected to scan the Ni material system under consideration [136]. All 3D techniques used in this paper are an implementation of the classic rotation method with a collimated beam: a single axis goniometer perpendicular to the incident X–ray beam and a framing area detector placed downstream of the sample [137]. The coordinate systems followed in this study can be found in Fig. 4.1. The loading axis of the MTS load frame and the rotation axis (ω) of the sample coincide with the z-axis in the lab frame. Characterization was performed through three techniques employing different beam and detector configurations but otherwise similar setups.

The crack path morphology and crack front position were captured through its progression, due to cyclic loading, via μ-CT. Scans were performed by the use of a 1 mm tall and 2 mm wide X-ray beam centered around the location of the initial crack in the sample. A detector with a 3 mm field-of-view and 1.5 μm square pixel size was used. The detector was positioned 12 mm away from the sample. The detector could not be moved further away from the sample, which would have permitted the use of phase contrast to elucidate the crack more clearly, due to spatial constraints of the setup. The sample was rotated over a 360° angular range and radiographs were

captured after every 0.2° increment. A μ-CT scan was performed each time cyclic loading was halted (specific states are aforementioned). The sample was held at the maximum applied load, since it is easier to detect the crack when it is fully open. A final scan in the phase contrast configuration with a more optimized setup for μ-CT (detector to sample distance was increased) was taken at 52,000 cycles after the end of the experiment when the space constraints were removed during the experimental teardown.

The grain structure including the orientations, morphologies, and grain boundary positions were determined in the region of interest in conjunction with the propagating crack via NF-HEDM [54,55]. NF-HEDM requires a setup that is almost identical to that of parallel beam tomography with a framing area detector with high spatial resolution, i.e. small effective pixel size and large field of view. However, it uses a line focused beam [34] for selecting a quasi-two-dimensional slice of the sample and a small beam-stop that blocks the very intense focused beam without compromising the diffracted beam from the grains. The same detector was used for both techniques. The sample to detector distances were nominally around 5.5, 7.5, and 9.5 mm to maximize the spatial resolution of this technique. Several detector distances were used to calculate the diffracted beam direction, corresponding to each spot, and determine the point of origin of diffraction, in order to index the position and orientation in the sample and subsequently reconstruct a detailed orientation map. A reciprocal space of 9 $Å^{-1}$ was covered at the largest detector distance. The sample was rotated over a range of $\omega \in (0, 360°)$ and images were captured after integrating over 0.25° $\Delta\omega$ intervals. Fifty scans with a line focused beam (1 μm tall and 2 mm wide) were taken, at a spacing of 4 μm, to cover a 200 μm region, as highlighted in Fig. 4.3 (c). Calibration images were obtained with a gold cube with a known and well-defined grain structure before the sample of interest was characterized. The calibration was refined by using grains in the actual sample in an optimization procedure based on points in all four quadrants and at grain boundaries until sharp and well-defined grain boundaries were obtained without any biases. The focused beam passing through the sample and the beam stop also captures an intensity contrast due to the difference in the mass attenuation coefficient between the inclusion and the matrix. This was used for registration purposes as described in the next section. The NF-HEDM characterization scan was taken at 20,000 cycles.

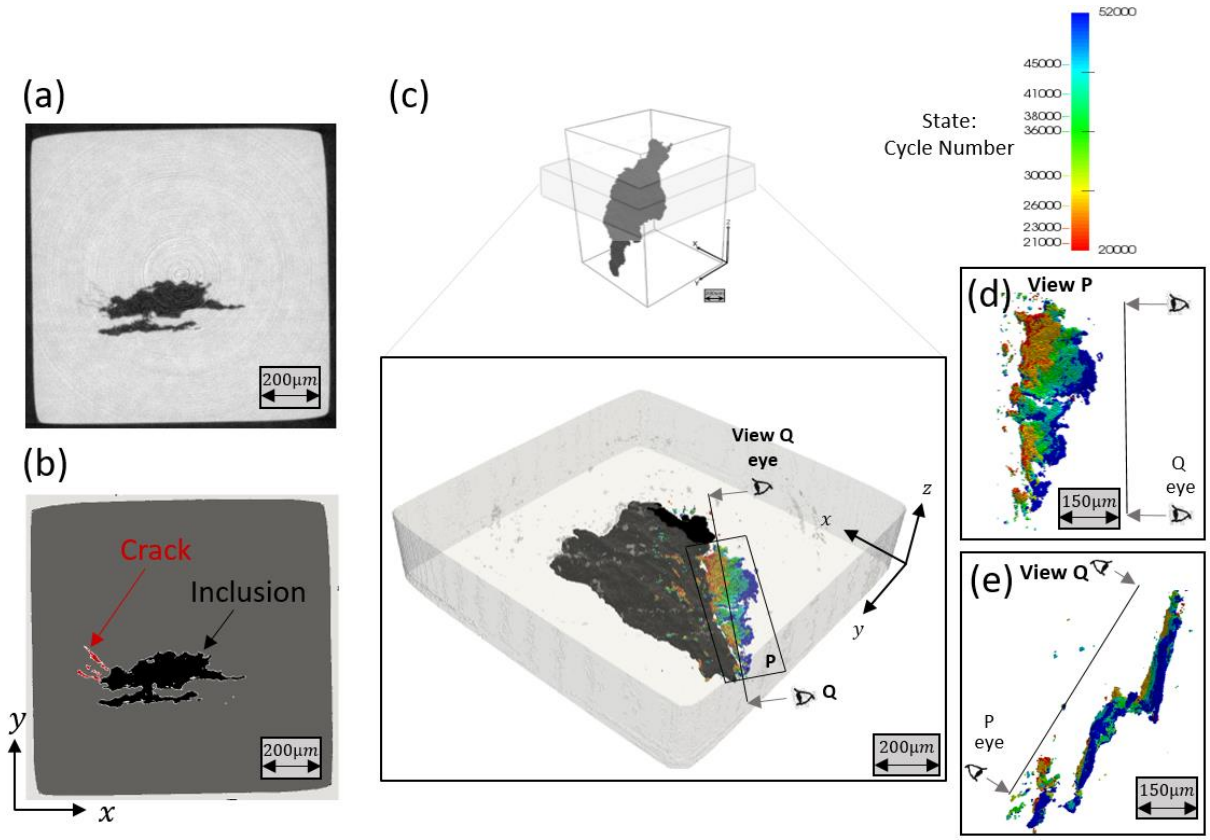

Figure 4.3 (a) Cross-section from μ-CT reconstruction juxtaposed with (b) results of segmentation of the different phases: matrix, inclusion, and crack. (c) Specimen with inset showing the crack growing from the inclusion between 20k and 52k cycles. (d) View of the crack along plane P (as defined in c), displaying crack growth relative to the cycle number. (e) View of the crack from vantage point Q (as defined in c), showing a bridge in the crack structure.

The lattice strain in the grains in the probed volume and especially at the crack front were determined via FF-HEDM [47,50]. A GE-41RT amorphous silicon flat panel detector with a size of 2048 X 2048 pixels at a pixel pitch of 200 μm was placed far away from the sample, around ~765 mm. At 20,000 cycles, 50 scans with a line focused beam (1 μm tall and 2 mm wide) were taken to cover a 200 μm region, coincident with the NF-HEDM scans. These scans were used to seed the NF-HEDM reconstructions thus ensuring registration of the initial state of the sample between the two techniques. At the remaining states, two scans with box beams (100 μm tall and 2 mm wide) were used to cover the 200 μm tall region of interest, in order to expedite data acquisition. A box beam with 100 μm height was found to irradiate an appropriate number of grains, to avoid overcrowding of diffraction spots within a diffraction ring on the area detector

(which is undesirable due to spot overlap that would result in a bias towards identifying larger grains during reconstruction and complicate the process of reciprocal space mapping). Eight complete Debye-Scherrer rings corresponding to {111}, {020}, {220}, {131}, {222}, {040}, {331}, and {240} planes in the FCC material were captured on the detector. Due to the limited dynamic range of the detector, a lead foil was adhered to the detector and positioned to attenuate the two inner diffraction rings in order to collect higher intensities in the outer diffraction rings, improving strain resolution of the measurement. The sample was rotated over an angular range of 360° and frames were saved after integration over $\Delta\omega$ intervals of 0.25°. The full rotation enables the measurement of all the Friedel pairs, which facilitate higher accuracy fitting of the grain positions and strain tensors [138]. Far-field HEDM was performed at each loading interruption, and the sample was held at the maximum applied load. A suite of calibration images were obtained using Ceria and Au at the beginning and at the end of the experiment to determine the detector distance, tilts, and distortion parameters and check for any significant setup changes [139,140]. The calibration was refined by using grains in the actual sample.

4.5 Reconstruction methodology and Registration Results

The μ-CT scans were reconstructed using an in-house code out of APS [38,39], which uses the GridRec algorithm [40]. A spatial resolution of ~3 μm according to the Nyquist theorem was achievable with the current detector setup. The reconstructions were optimized in this code and then post-processed using ImageJ [41], in order to clean up the tomography artifacts and remove noise. Ring removal was performed using an in-house code implemented in Matlab, based on the algorithm specified in [42]. The reconstruction from the final scan configured for phase contrast, at 52,000 cycles, has been shown in Fig. 4.2(b) and results in sharper gradients between phases, thus making it easier to segment the crack. In Fig. 4.3(a), the grayscale color bar has been inverted to show the intensity differences between the different phases in the specimen. The SFC experienced a range of intensity values, thus making it difficult to extract the crack morphology. Specifically, the SFC had a dark intensity, similar to the inclusion, when the crack was wide open and a light intensity, similar to the Ni-matrix, near the crack tip. Therefore, segmentation tools, based on mere intensity thresholds, fail to extract the crack properly. Instead, the crack was segmented from tomograms via a trainable machine learning algorithm called WEKA segmentation [43], available as an ImageJ plugin. Attributes of the crack, based on its

derivatives/gradients to detect edges, eigenvalues of the Hessian matrix to determine plate/line-like features, and structure tensor calculations with smoothing were employed to extract the precise morphology of the crack. The phase-contrast μ-CT scan at 52,000 cycles was segmented first and used as a template, while segmenting previous states of the crack identified through absorption contrast μ-CT characterization. Each state was segmented to determine the crack front and consolidated to capture the progression of the crack, in Fig. 4.3 (c). The SFC is observed to initially grow along the matrix-inclusion interface, moving downward on the left side of Fig. 4.3 (d), and subsequently moving rightward into the matrix. The progression of the SFC will be discussed in greater detail in Section 4.6.

FF-HEDM scans were reconstructed using the Microstructural Imaging and Diffraction Analysis Software (MIDAS) [51,52], developed at the APS. Far-field HEDM data is reconstructed to provide the grain centroid position (3 variables), an associated grain averaged orientation (3 variables), and a grain averaged elastic strain tensor (6 variables). The FF-HEDM reconstruction, in terms of the lattice strain in the loading direction, for a line scan taken at 20,000 cycles is shown in Fig. 4.2(e). Far-field HEDM reconstructions used data collected from the 3rd through 8th diffraction rings of the Ni-based superalloy and resulted in a spatial resolution of ~20 μm for the grain centroid positions, angular resolution within 0.1° for the crystallographic orientation, and a lattice strain resolution on the order of 1e-4 for the grain average value [52,53]. The errors in the lattice strain are relatively higher for grains which exhibit low lattice strains, close to the resolution value mentioned above. A completeness threshold, which is the ratio of the measured to expected diffraction spots, was set at 60%, and any grain that did not meet this cut-off was not considered in the reconstruction. Approximately 2500 grains were found in the 200 μm region of interest.

Near-Field HEDM scans were reconstructed using an extension of MIDAS [51,52]. The reconstruction was performed with a triangular grid; an edge size of 2 μm was used to obtain a high signal to noise ratio for a detector pixel size of 1.5 μm. The orientation search space for forward modeling was seeded with orientations determined from FF-HEDM reconstruction, with a tolerance of 2°. The tolerance in the orientation space allows for identification of intragranular orientations and grains with higher confidence. Any pixels and regions with a confidence of less than 40% were refit with all possible orientations from a gridded table representative of the FCC fundamental space. The low confidence index was primarily necessary to reconstruct the grain boundary regions, as seen in Fig. 4.2(c), considering this sample was subjected to cyclic loading

prior to NF-HEDM characterization. The triangular mesh is re-gridded onto a regular 3D co-rectangular mesh with a resolution of 1.5 μm and smoothed via a dilation and erosion procedure. A grain growth algorithm based on enabling a maximum misorientation of 2° of neighboring voxels was employed to segment the orientation maps into grains.

Registration was performed between the crack determined via μ-CT, the grains determined via NF-HEDM, and the lattice strains determined via FF-HEDM. To assist in the registration, between the crack position and the grains, an additional μ-CT reconstruction was performed using the beam projected onto the detector during the NF-HEDM scan through the beam-stop. The main challenge that needed to be considered during reconstruction is the low intensity and extra patterns present in the measured beam due to the uneven surface of the beam-stop. The purpose of this μ-CT reconstruction was not to achieve a high resolution, but to identify the shape of the inclusion, which was correlated to the correct slice in the μ-CT reconstruction. In-plane registration was done using a binarized version of the confidence map like the one shown in Fig. 4.2 (c) using the corr2 function within Matlab along with visual inspection. After registration, tomography slices were used as a mask to rectify ill-fit voxels as shown in Fig. 4.2 (d). The grains surrounding the crack were subsequently extracted from the complete grain map as shown in Fig. 4.4(a). In the vicinity adjacent to the crack, around 50 grains were identified, and the corresponding attributes to these grains are shown (Fig. 4.4 (b)). Specifically, the grains along both the front and the back face of the crack are depicted, according to the vantage point P as described earlier in Fig. 4.3 (d). From such a depiction, if the crack was intragranular in nature, the same grain would appear on the front and back faces. Conversely, an intergranular crack path would show distinct grains on the front and back faces of the crack at a particular location. Using such a methodology, we will determine intergranular and/or intragranular parts of the crack path in the subsequent sections of this paper.

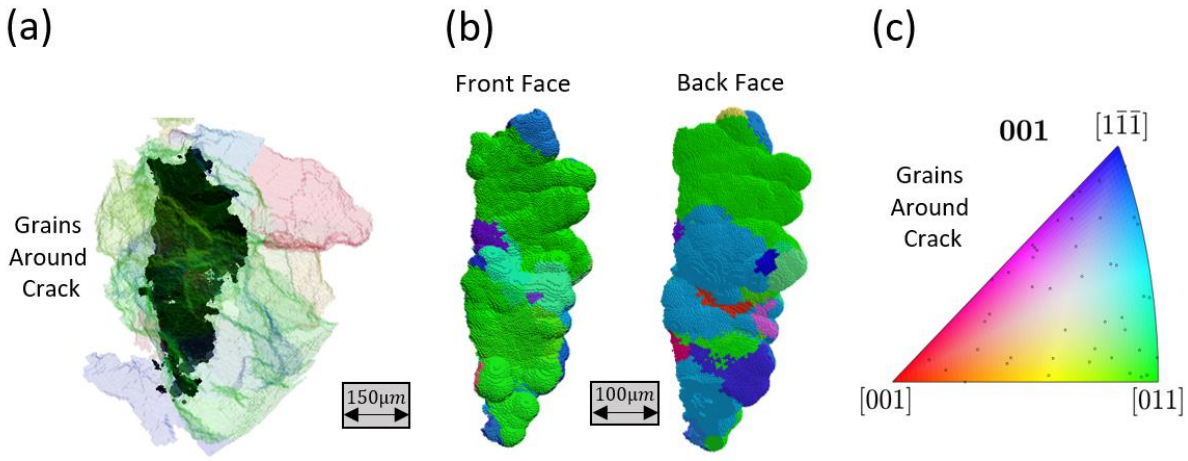

Figure 4.4 (a) Grains of interest surrounding the crack path extracted after registration between NF-HEDM and μ-CT. (b) Grains adjacent to the crack, as shown from the front and back faces (see view P of Fig. 4.3 (d)). (c) Stereographic triangle for reference to the colors of the grains and the orientation distribution of the grains adjacent to the crack.

Based on the aforementioned reconstruction techniques, the registration between the NF-HEDM and FF-HEDM reconstructions was straight forward. The diffraction spots for each grain in the NF-HEDM reconstruction were simulated (discussed in next paragraph) and compared to those indexed to the grains found through FF-HEDM, and thus grains were registered across the different modes of characterization. Since the full elastic strain tensor (ε_{ij}^{e}) is available as shown in Fig. 4.5 (a), the corresponding stress tensor (σ_{kl}) can be determined unambiguously using the stiffness tensor (C_{ijkl}) via the generalized Hooke's law:

$$\sigma_{kl} = C_{ijkl} : \varepsilon_{ij}^{e} \tag{4.1}$$

For RR1000, the values of C_{ijkl} were adopted from [11]. Moreover, during cyclic evolution, FF-HEDM characterization was performed multiple times, for which this form of registration was repeated between grains found through FF-HEDM across different states. Grains are matched across states with a mean misorientation of ~0.5° and a mean centroidal distance of ~25 μm. The micromechanical state of the grains determined in conjunction with the progressing crack front will be used to further explore the SFC regime in Section 4.6.

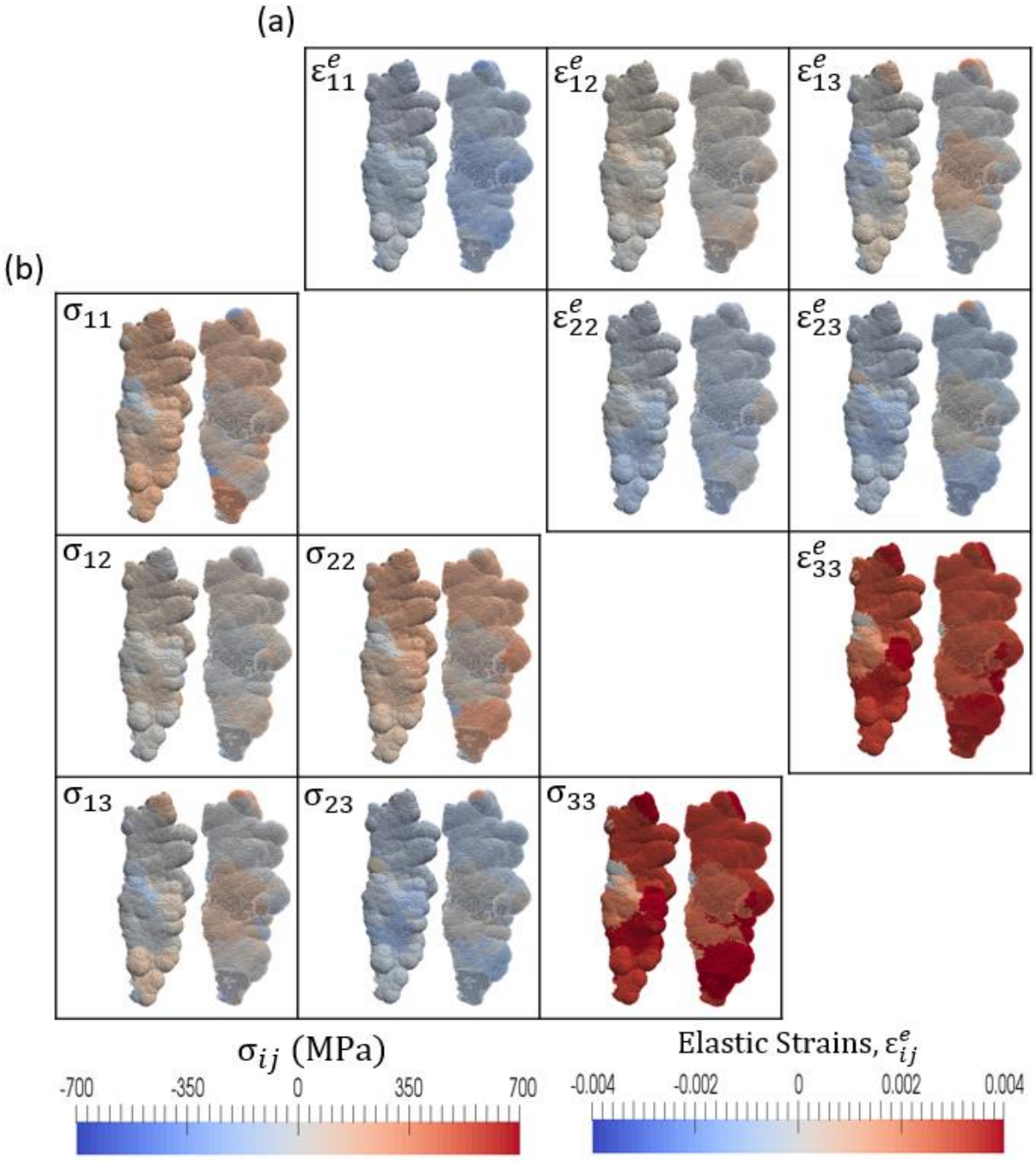

Figure 4.5 (a) Grain average elastic strain tensor for each grain adjacent to the crack on the front and the back face, measured through FF-HEDM, at 20,000 cycles. (b) Grain average stress tensor calculated for each grain adjacent to the crack (see Fig. 4.3 (d) for crack view perspective).

Damage within the microstructure, due to an approaching crack front, manifests via plasticity and a stress field. The plasticity is accommodated through distortions in the lattice of the grains, in the form of geometrically necessary dislocations resulting in an intragranular orientation spread. Meanwhile, the stress fields, due to the crack and the dislocations, are accommodated through lattice strain gradients. In essence, the degree of plasticity and lattice strain gradients accommodated in the grains, ahead of the crack front, can be quantified based on the spread of the diffraction spots. A schematic of the distortion to the lattice of a grain due to an approaching crack front has been depicted in Fig. 4.6. The distortion to the lattice can be measured by calculating the full width at half maximum (FWHM) for a set of diffraction spots corresponding to the specified grain in two polar directions (η and θ), as shown in the schematic. The FWHM, in polar coordinates, along 2θ or the radial direction corresponds to the heterogeneity in the lattice strain within the grain [57]. The FWHM along η (along the azimuth) or ω (across frames during rotation of the sample) corresponds to the curvature of the lattice planes within the grain [57,59]. In an effort to quantify this damage within the grain via the FWHM measures on all diffracting planes, an in-house code was developed. A virtual diffraction simulation, as described in [58], was adapted from algorithms in MIDAS and used to determine the peak positions from the reconstructed grains. The position, orientation, and lattice strains of the grains determined through FF-HEDM, via MIDAS, were used as an input, while the position of the diffraction spots in terms of the η, ω, and θ coordinates on the detector were obtained as the output from the diffraction simulator. The simulator was coupled with an extraction and thresholding procedure to determine the FWHM of all the spots indexed to a grain. In the Supplementary, the histograms of the radial (displaying the lattice strain gradients) and azimuthal (displaying the intragranular misorientation) FWHM values are plotted for grains near and away from the crack front. Histograms of the FWHM on the {220} and {222} planes within individual grains show an increasing FWHM value from 20k to 52k cycles. This evolution of the histogram is indicative of deformation on specific planes within the specified grains. In the remainder of the paper, we have focused on presenting these reciprocal mapping measures on specific planes for selected grains ahead of the crack tip, in order to further understand the failure mechanism associated with SFCs.

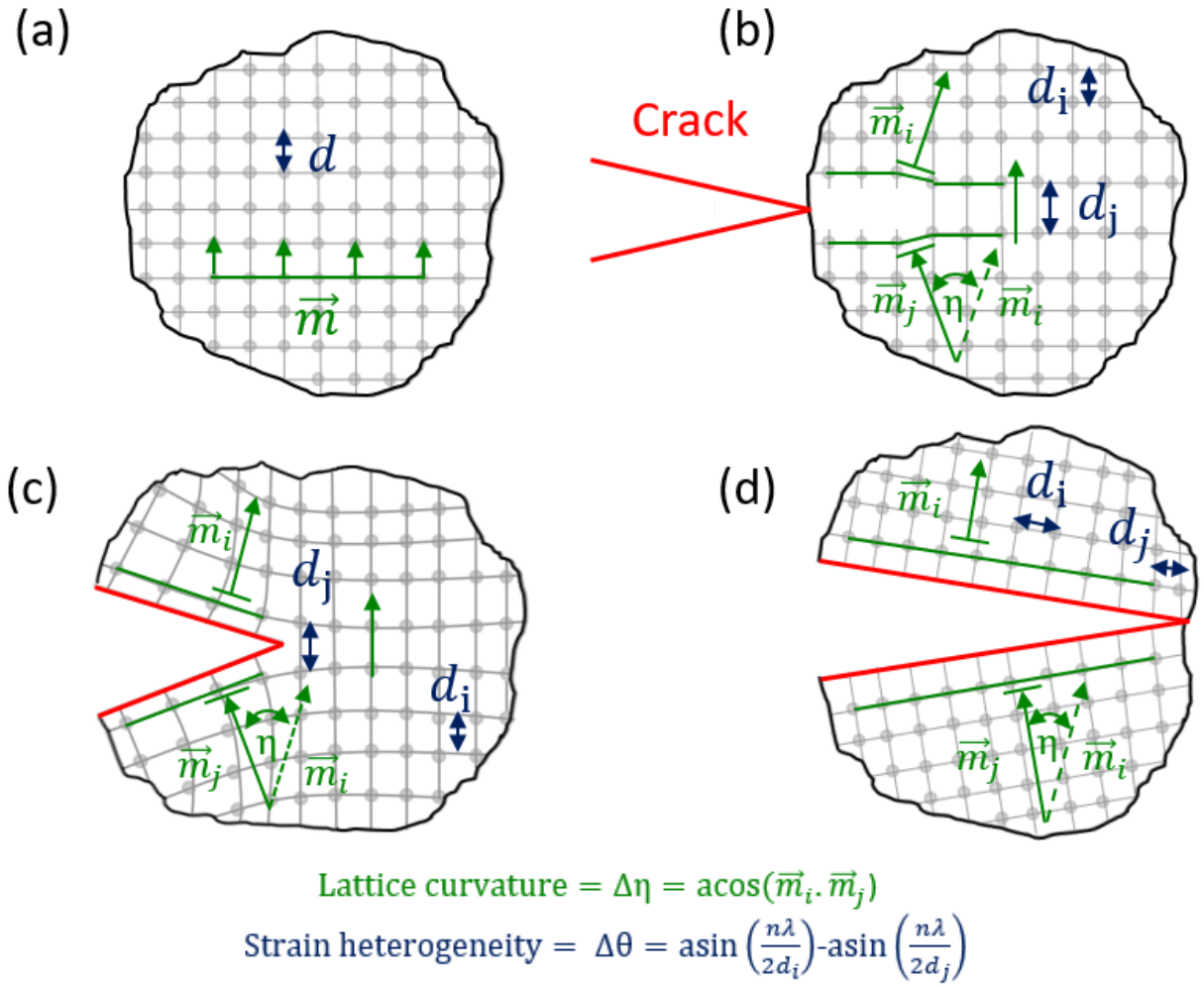

Figure 4.6 The evolution of the deformation in the lattice due to an approaching SFC is described through four stages (a) grain is away from the crack, shown with an idealized lattice as a reference case, (b) crack is impinging on the grain and emitting dislocations, (c) crack is propagating through the grain, (d) crack has propagated through the grain bifurcating it into two sub-grains. Lattice distortion is measured via two metrics: curvature in the planes of the lattice and the heterogeneity in the spacing of the lattice. The lattice plane normals are denoted by 'm' and the difference between the normal of a plane (because of distortion) is captured along the azimuth, η. The lattice plane spacing is denoted by 'd' and the difference between lattice spacing in different regions of the grain is captured along the radial direction, θ. In the images shown, the loading axis is along the vertical direction.

4.6 Discussion

The goal of this paper is to assess the SFC regime, in terms of crack path and growth rate, through a grain scale description of the micromechanical fields around the crack. Towards this objective, in Fig. 4.7, we have outlined the progression of the crack through the first few grains, with reference made to the grains that will be considered in greater depth throughout the discussion. For the aid of the reader, we will first explore the progression of the crack, in more detail, and reference this progression in the remainder of the discussion.

From the results of crack initiation in the preceding study [67], it is well understood that the matrix-inclusion interface serves as a preferred site for decohesion. This has been understood as an amalgamation and interplay of three primary factors, specifically the intensified stress created by partial debonding at the interface due to thermo-mechanical processing, the residual stress state created by the inclusion in the surrounding matrix, and the geometric factors of the inclusion (orientation, size, and morphology). Partial debonding between the matrix and the inclusion has also been surmised as a significant contributor towards undesirable stress concentration in steels [94,96]. For this specimen, we have found that the confluence of the three factors created a necessary gradient in the micromechanical fields, particularly the stress triaxiality. These gradients in the micromechanical fields also affect the SFC progression between 10,000 to 21,000 cycles. Between these initial stages, the crack grows vertically down the sample, primarily along the matrix-inclusion interface. In Fig. 4.7 (a), the initial progression of the crack has been overlaid on the full profile of the crack at 52,000 cycles (the complete crack profile shown in a lighter hue). The initiation point and the direction of crack growth, between these stages, has been marked on the left, which is along the inclusion-matrix interface.

The growth of the SFC, into the matrix, starts from 21,000 cycles. Between 21,000 and 30,000 cycles the crack grows, tortuously, but on two fairly well-defined, almost parallel, crack planes. This has been shown in Fig. 4.7 (b), and the silhouettes of these planes are highlighted. Details of the minor tortuosity of the SFC on these crack planes will be discussed in the following sub-sections. A major deviation in the SFC, however, occurs after 30,000 cycles, where the crack starts to become fully developed. An important segment of the SFC regime is the mechanism of micro-cracks coalescing to form a dominant crack [16]. After 30,000 cycles, as shown in Fig. 4.7 (c), the two halves of the crack coalesce on a distinct plane, almost perpendicular to the loading axis, which we will refer to as the crack bridge.

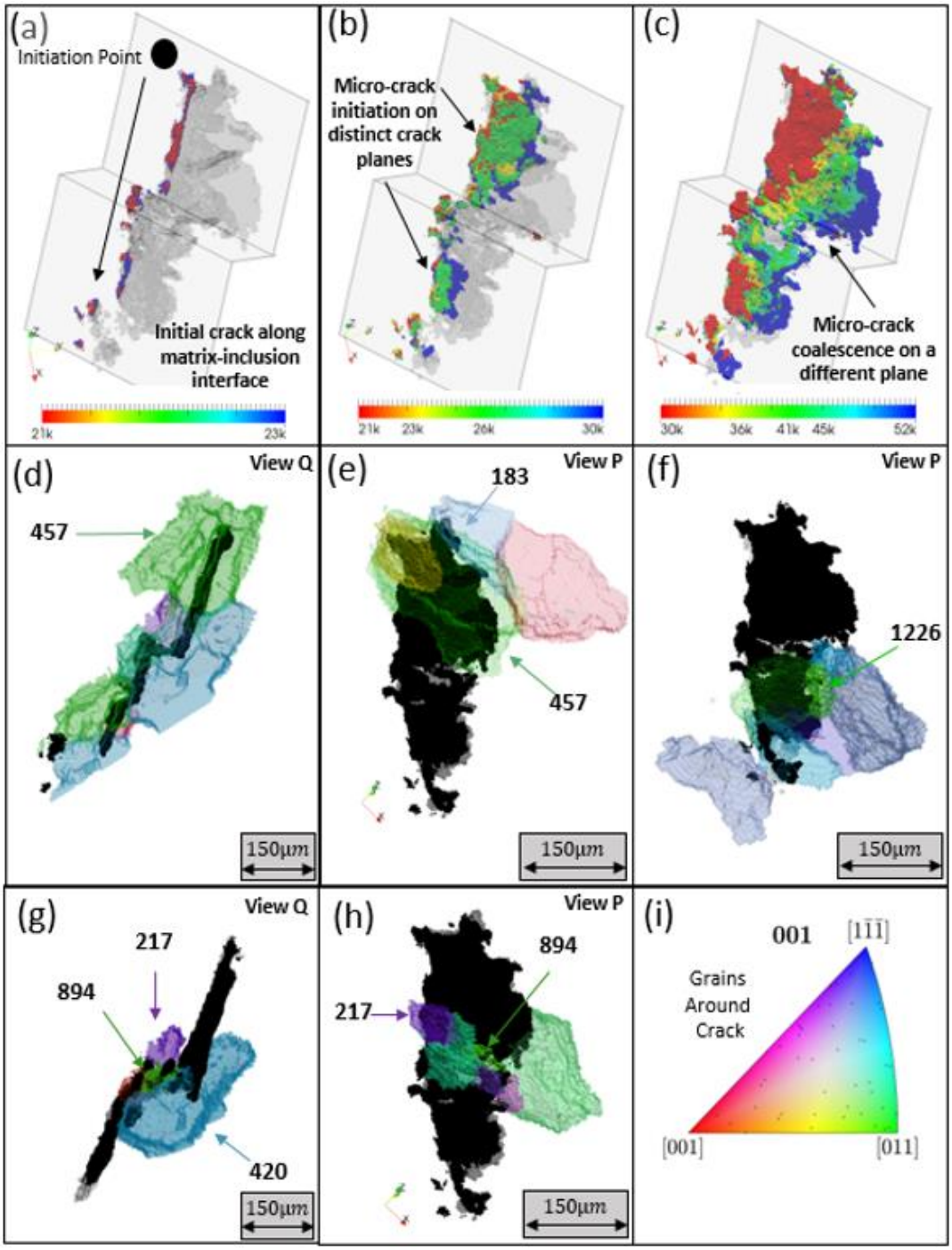

Figure 4.7 Division of the crack progression into three parts, (a) growth along the inclusion-matrix interface, (b) micro-cracks growth on two distinct planes between 21k and 30k cycles, (c) micro-cracks coalescence and growth on a bridge between 30k to 52k cycles. Selecting specific grains for further discussion: (d) intragranular SFC growth in Grain 457, (e) crack arrest at Grain 183, and (f) crack propagation along Grain 1226. Intergranular crack growth as shown in two views (Q and P, see figure 4.3(d) and 4.3(e) corresponding to (g) and (h), respectively. (i) Stereographic triangle displaying orientations for grains depicted in (d-h).

To further interrogate the progression of the SFC with respect to the micromechanical state of the grains, the discussion has been divided into three sections. In Section 4.6.1, the evolution of pertinent stress metrics is explored to ascertain their relevance in the SFC regime. In Section 4.6.2, the crystallographic nature of the crack path and rate have been investigated through tortuosity observed in the crack plane within a specific grain. Finally, in Section 4.6.3, the role of the plasticity ahead of the crack front and its influence on the crack progression have been discussed.

4.6.1 Micromechanical evolution

We have chosen three classically used stress based metrics, at the grain scale, to understand their role in crack propagation in the SFC regime: the deviatoric part (σ^{dev}) of the stress tensor (σ_{ij}) in the form of von Mises stress (σ_{vm}), an opening stress inspired term based on the dilatational component of the stress tensor in the form of the hydrostatic stress (σ_{Hyd}), and a combination of these two factors, to understand their relative roles, through the stress triaxiality (σ_{TRI}). They have been defined as follows:

$$\sigma_{vm} = \sqrt{\frac{3}{2}\sigma^{dev} : \sigma^{dev}}\ , where\ \sigma_{ij}^{dev} = \sigma_{ij} - \frac{\sigma_{kk}}{3} \tag{4.2}$$

$$\sigma_{Hyd} = \frac{\sigma_{kk}}{3} \tag{4.3}$$

$$\sigma_{TRI} = \frac{\sigma_{Hyd}}{\sigma_{vm}} \tag{4.4}$$

These stress metrics have been calculated at each state characterized during the experiment, in terms of grain-averaged values from FF-HEDM. Their values for each of the grains adjacent to the crack are shown in Fig. 4.8, with the views shown for the front and back face of the crack. The columns of Fig. 4.8 correspond to the micromechanical fields at 21,000; 30,000; 41,000; and 52,000 cycles, respectively. The progression of the crack (as indicated in black relative to the full crack profile at 52,000 cycles in gray) has been presented in the first row for reference. In the first column, at 21,000 cycles, the crack is primarily limited to progression along the matrix-inclusion interface. Despite which, there is a high amount of heterogeneity in the stress metrics for each of the adjacent grains to the crack front. A complex loading environment is created due to the inherent granular microstructure and local grain neighborhoods [28–30], which are poised to have an effect on the propagating crack.

Figure 4.8 Grain averaged stress metrics plotted against the cyclic loading state. (a) crack progression at each state added for reference, (b) von Mises Stress, (c) stress triaxiality, (d) hydrostatic stress, (e) stress coaxiality, (f) maximum resolved shear stress, and (g) normal stress on plane corresponding to the most active slip system.

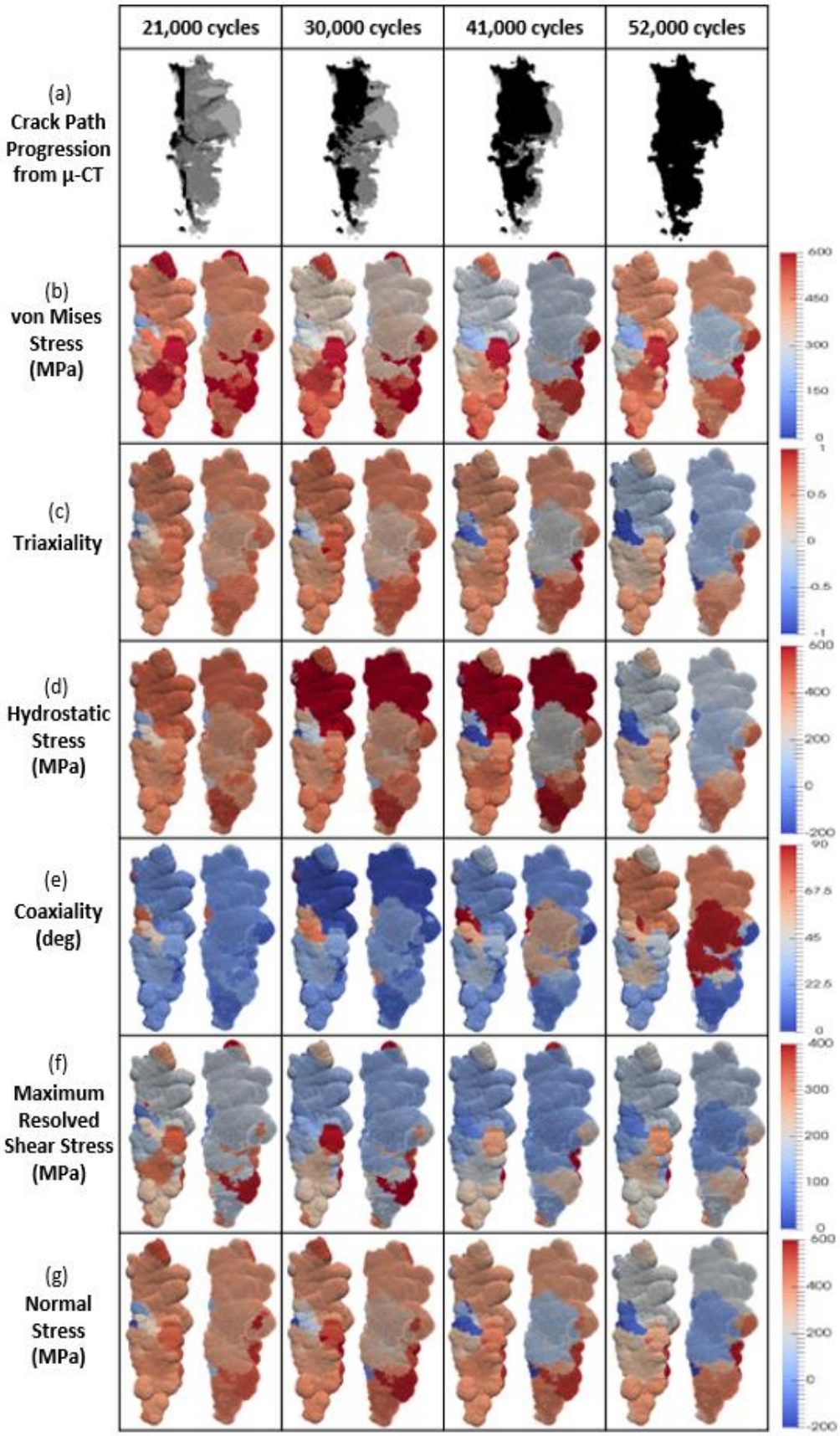
21,000 cycles
30,000 cycles
41,000 cycles
52,000 cycles
(a) Crack Path Progression from μ-CT
(b) von Mises Stress (MPa)
600
450
300
150
0
(c) Triaxiality
1
0.5
0
-0.5
-1
(d) Hydrostatic Stress (MPa)
600
400
200
0
-200
(e) Coaxiality (deg)
90
67.5
45
22.5
0
(f) Maximum Resolved Shear Stress (MPa)
400
300
200
100
0
(g) Normal Stress (MPa)
600
400
200
0
-200

For all of the grains shown in Fig. 4.8, we highlight three sets of grain neighborhoods, corresponding to the top grains (Fig. 4.7 (e)), middle grains (Fig. 4.7 (g)), and bottom grains (Fig. 4.7 (f)) around the crack. In the top grains surrounding the crack, the contribution of the von Mises stress versus the hydrostatic stress becomes apparent. The crack is mainly intragranular at this location, through grain 457 in Fig. 4.7 (e). During propagation through this region, between 30,000 and 40,000 cycles, the von Mises stress reduces, while the hydrostatic stress increases. The stress triaxiality captures the competing roles of the dilatational and deviatoric stress measures, and a high value of the stress triaxiality indicates the dominance of the hydrostatic stress during intergranular crack propagation. After propagation through the grain 457, at 52,000 cycles in the last column of Fig. 4.8, the von Mises stress increases, while the hydrostatic stress and correspondingly stress triaxiality drop in magnitude. This is partly attributed to the crack approaching a neighborhood of grains that are smaller in size. In the grains adjacent to the lower part of the crack, the crack is propagating through many smaller grains, as shown in Fig. 4.7 (f), which makes it difficult to capture the intragranular nature of the crack progression in this segment. Despite this, the dominant role of the hydrostatic stress, during the intragranular propagation through the grains at the bottom of the crack is captured.

The grains adjacent to the middle part of the crack display a different behavior, as the crack is progressing in an intergranular nature. The crack bridges between the top and bottom halves after 30,000 cycles in this region. It is determined that the crack, within registration errors, is propagating along grain boundaries, as shown in Fig. 4.7 (g) and (h). It should be noted that intergranular crack propagation in Ni-based superalloys is known to be highly unlikely at room temperature and in ambient lab environments [16,17,141].

To highlight the heterogeneity offered by the grains surrounding the crack, a stress coaxiality metric (σ_{CoAX}) [91,92] is employed, as defined below:

$$\sigma_{CoAX}\angle = cos^{-1}\left(\frac{\sigma^{Macroscopic}:\sigma^{Crystal}}{\|\sigma^{Macroscopic}\|\|\sigma^{Crystal}\|}\right) \tag{4.5}$$

The σ_{CoAX} is a measure of the alignment of the stress state within the grain to the macroscopic applied stress state. A small angle implies that the stress state of the grain conforms to the macroscopic loading. A non-zero coaxiality value, indicating a misalignment with respect to the macroscopic loading, is expected due to the complex interaction of grains in their local neighborhoods, as confirmed by the observations shown in Fig. 4.8 (e) at 20,000 cycles.

The stress calculated for the grains in the middle region, on both the front and back of the crack plane is much lower than the surrounding grains. This is clearly visible for grain 420, seen on the back face and grains 217 and 894, on the front face. The grains on the front face (217 and 894) have low values of all stress metrics throughout the crack progression and high stress coaxiality. After 41,000 cycles, the stress in the grain on the back face (grain 420) reduces and becomes completely misaligned to the applied loading, with respect to the stress coaxiality metric. Further analysis reveals that the grains in this region have special low energy grain boundaries, determined according to the process outlined by Sangid et al [142]. Grains 420 and 217 have a $\sum 27$ grain boundary between them, while grains 420 and 894 are joined by a $\sum 3$ boundary. Because of their low energy configuration, these boundaries typically impede crack growth [143]. But in this case, after the SFC grew significantly on through the top and bottom set of grains, a bridge formed through the middle grains along the low energy grain boundaries, which are prevalent in this material [142]. One possible explanation for this intergranular behavior of the crack is the low stress and high coaxiality values exhibited by these grains. Lastly, we note, once the crack progresses past these grains (e.g. the grains are located at the crack flanks), the stress in each of these grains significantly reduces, because of the physical discontinuity in material created by the crack.

To understand the crystallographic nature of the SFC, the stress tensor (σ_{ij}) is transformed into the crystal coordinate system ($\sigma_{ij}^{Crystal}$) and then resolved onto each of the 12 FCC slip systems. The maximum resolved shear stress (τ_{MRSS}), identifying the critical slip system, and consequently, the normal stress (σ_n) on the associated critical plane are determined as follows:

$$\tau_{MRSS} = \max_{\forall m,s}(|\tau^{ms}|) = \max_{\forall m,s}\left(\left|m_i s_j \sigma_{ij}^{Crystal}\right|\right) \tag{4.6}$$

$$\sigma_n = (\sigma_{ij}^{Crystal} . m_i) \, . m_j \tag{4.7}$$

where m_i is the slip plane normal and s_j is the slip direction. The values for τ_{MRSS} and σ_n for each of the grains surrounding the crack have been plotted in the last two rows of Fig. 4.8. It is determined that the normal stress, similar to the hydrostatic stress, is high for most of the grains around the propagating crack, except in the middle of the crack, in which intergranular growth is observed. Normal stress has been proposed in models for crack growth by past researchers, including Fatemi and Socie [127] and McDowell and co-workers [132]. The τ_{MRSS} shows a less definitive trend in these plots, but to further explain this behavior a slip system level analysis is

performed to consider the crack path with respect to the crystallographic slip planes and directions in the encountered grains. To this end, in the next sub-section, we zoom into a particular grain to study the crystallographic nature of SFCs.

4.6.2 Crystallographic nature of SFC

The material modeling community has several crystallographic-based models of SFC behavior that need experimental datasets for validation. Crystal plasticity modeling is primarily based on the assumption of plastic deformation being restricted to slip in particular crystallographic directions on particular crystallographic planes, mediated by resolving the stress state onto the corresponding slip systems. McDowell and co-workers have demonstrated that the micromechanical results of crystal plasticity simulations can be used to formulate fatigue indicator parameters to describe the SFC regime [118,132]. Additionally, Rovinelli et al. used an X-ray dataset in companion with crystal plasticity simulations to identify the appropriate driving force for SFC growth [122,144]. In their studies, they relied on simulations to obtain the stress state relative to the microstructure, while in this study, through the combination of FF-HEDM and reciprocal space mapping, the resolved stress on slip systems and the associated slip activity is experimentally identified in each grain ahead of the advancing crack.

A slip system level analysis has been carried out for grain 457 in Fig. 4.9 to identify the crystallographic nature of the SFC with the associated slip activity directly ahead of the crack tip. Grain 457 has been chosen since the crack progresses tortuously within this grain, between 20,000 and 52,000 cycles. The crack path, through this grain, can be broadly divided onto three distinct segments which are associated with different crack planes. These stages have been depicted in Fig. 4.9 (a) to (c).

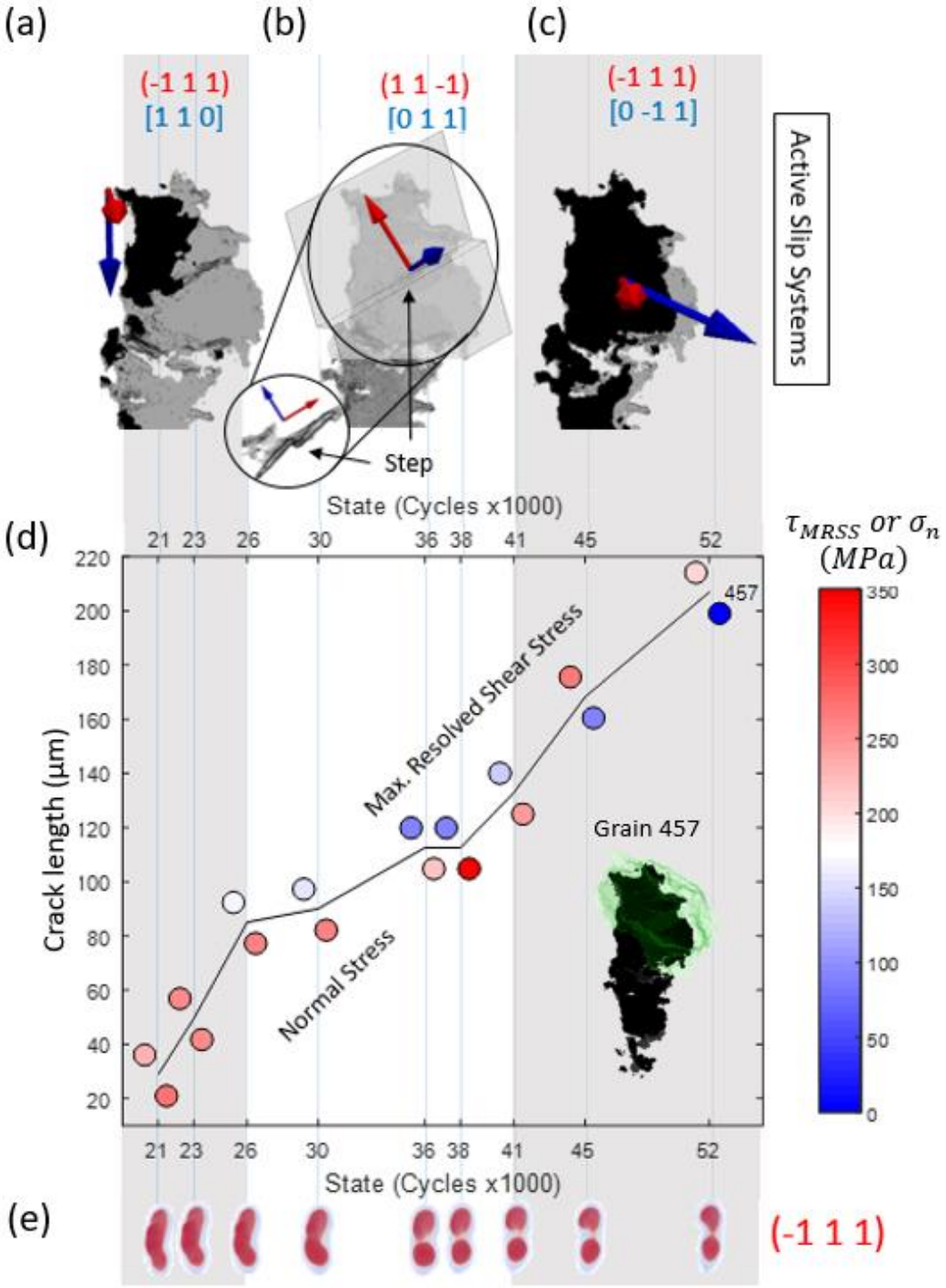

Figure 4.9 Crack path alignment with the most active slip system in (a) the first segment between 20k and 26k cycles, (b) the second segment between 26k and 41k cycles, and (c) the third segment between 41k and 52k cycles. (d) Graph between the crack length and the cyclic loading state along with the τ_{MRSS} and σ_n plotted at each state characterized through FF-HEDM. (e) Spread of the diffraction spot corresponding to the $(\bar{1}11)$ crystallographic plane capturing the bifurcation of the grain into two sub-grains by the propagating SFC.

During the first segment shown in Fig. 4.9 (a), the crack progresses on the initial plane until 26,000 cycles, towards the bottom and right directions, relative to the image shown. The crack plane is observed to be parallel to the $(\bar{1}11)$ plane in grain 457 (the normal is indicated with a red arrow). Next, by calculating the τ_{MRSS} for this grain, we identify the most active slip system which is on the $(\bar{1}11)$ plane and along the [110] direction (blue arrow pointing vertically downward in Fig. 4.9 (a)). For this segment, the crack is predominantly growing in the direction and plane corresponding to the most active slip system in this grain, since the initial growth of the crack is along the matrix-inclusion interface. This characteristic is observed repeatedly in the present analysis and represents a driving force that dictates the crack path, as further discussed below. During the second segment, the crack changes directions and represents a step in the total crack path. Between 26,000 and 41,000 cycles, part of the crack is growing on the step (corresponding to the $(11\bar{1})$ slip plane (red arrow) and [011] slip direction (blue arrow) via the τ_{MRSS} analysis) representing the second segment, but it is important to note that the crack progression on these segments is not sequential, thus the crack grows simultaneously on several segments. The initial crack plane, the step, and the final crack plane have been depicted in Fig. 4.9 (b) through their silhouettes for clarity. For the third segment, after 41,000 cycles, the most active slip system is determined by the τ_{MRSS} analysis for this grain, which corresponds to the $(\bar{1}11)$ slip plane (red arrow) and $[0\bar{1}1]$ direction. The crack plane of the third segment is parallel to that of the first segment, but the crack growth path is primarily in a different direction, as shown in Fig. 4.9 (c). The implications of this analysis are twofold. First, the τ_{MRSS} analysis is capable of demarcating the most active slip system in the grain of interest [145]. Secondly, and more applicable to this study, the crack path, in terms of direction and plane, aligns with the most active slip system in the grain that encompasses the crack tip.

This alignment of the crack propagation direction to the most active slip system in the grain directly ahead of the crack tip would indicate that the crack path is dictated by the stresses ahead of the crack tip, but in the case of SFC, those stresses are confined to the stress state of the grain that encloses the crack tip. For the SFC case, Mode II fracture dominates the mechanism for the crack advancement and is commonly attributed to the shear stresses in the grains ahead of the crack tip [146]. In many of the fatigue indicator parameters, a term is included to capture the maximum shear stress as a surrogate metric to determine the crack path [118]. Via a Bayesian network to identify correlations with experimental data, Rovinelli et al. found that the τ_{MRSS} is the second

most indicative value to determine the crack growth direction [126]. Unlike the study by Rovinelli et al. [126], in this analysis, τ_{MRSS} is directly obtained from the experimental data, as opposed to inferences from modeling, thus removing any ambiguities or model form error in the subsequent analysis for the crack driving force. Hence, this study corroborates many of the surrogate fatigue metrics proposed that emphasize the τ_{MRSS} of the grains directly ahead of the crack tip to dictate the crack direction.

Beyond determining the crack path, a similar analysis explores the role of τ_{MRSS} on the growth rate in the SFC regime. The length of the crack was measured, through its progression within this grain, at each of the ten states characterized by FF-HEDM. The length of the crack was measured based on the magnitude of a vector between the initiation point and the furthest point of the crack within grain 457. In Fig. 4.9 (d), the crack length is plotted with respect to the cycle number at which it was measured. The slope of this curve determines the crack growth rate through this grain. The magnitude of the τ_{MRSS} and σ_n have been plotted above and below the curve in Fig. 4.9 (d), respectively. The σ_n on the critical plane plays the role of an opening stress-like term and its value is high throughout cyclic loading, with the exception of the last two points corresponding to the crack propagating through almost the entirety of the grain. Likewise, surrogate models for SFC advancement have included a term for σ_n [127,132], with the present measurements confirming the importance of σ_n on the SFC rate. The magnitude of the τ_{MRSS} is initially high until 26,000 cycles, and the crack growth rate (i.e. slope of the curve in Fig. 4.9 (d)) is high as well, while between 26,000 and 41,000 cycles, τ_{MRSS} has a lower magnitude, when the crack is simultaneously growing on the two parallel $(\bar{1}11)$ planes and along the step connecting these planes. The crack growth rate also slows down during this period. After 41,000 cycles, both the magnitude of the τ_{MRSS} and the crack growth rate increase. It can be inferred from this trend that a correlation between the maximum resolved shear stress and the crack growth rate exists. The shear stress on the active slip system influences the crack growth rate, as it controls and enables slip processes which affect crack growth as proposed by Neumann [124] (originally for long cracks) and has been identified in surrogate models for SFC [127,132] and in the functional relationship expressed by Rovinelli et al. [126].

Finally, the most prominent crack plane, i.e. the $(\bar{1}11)$, representing the first and third segments of crack growth in this grain, as discussed earlier, is analyzed through reciprocal space mapping in Fig. 4.9 (e). A diffraction spot for the $(\bar{1}11)$ plane in this grain is shown, in which

spreading of the spot indicates intragranular misorientation, presumably due to slip processes and cracking. At the beginning of the experiment, a crack is already present in this grain; as the crack progresses during the experiment, the grain is transitioning between the states described in the schematic represented in Fig. 4.6. (c) and Fig. 4.6. (d). The spot spreading is seen to increase until 26,000 cycles, after which the crack starts bifurcating and cleaving the grain into two sub-grains, which is apparent in the gradual formation of two well-defined distinct spots (see Fig. 4.6(d) for schematic). This is presented as an exaggerated case of deformation to the lattice, due to opening of the crack tip, that can be quantified through the FWHM measures of the diffraction spot to capture the plasticity in the grain ahead of the progressing crack. From a continuum standpoint, the plastic zone ahead of the crack front has been found to be important in the past and is still used to understand crack growth phenomenon [102], while here we are able to determine the degree of plasticity in each grain ahead of the crack tip. In the last section, we explore the results of reciprocal space mapping to identify the role of plasticity in the grains ahead of the crack front on the SFC growth and arrest in distinct directions along the crack front.

4.6.3 Plastic zone ahead of SFC

Several researchers have found the necessity of transmission of plasticity to adjacent grains, ahead of the crack tip, for the propagation of a crack [133,147]. To place the plasticity ahead of the crack front into perspective, the mechanical stress state of the local grains ahead of the crack front and their evolution with respect to the approaching crack is interrogated first. A principal stress jack is a simple way of visualizing the complete stress state within a grain and has been advantageously used in the literature [64,148]. In a stress jack, the arrows point along the direction of the eigenvector and the color of the arrows represent the eigenvalues of the stress tensor. In this way, the maximum principal stress and direction are captured, which also provides information of the reorientation of the stress tensor during crack advancement. In particular, two grains have been selected for analysis in Figs. 4.10 and 4.11. In the first case, as shown in Fig. 4.10, the crack reaches grain 183, at 36,000 cycles, but with additional loading cycles, the crack does not propagate through this grain. In the second case, the crack advances in a constant direction through grain 1226, as shown in Fig. 4.11. In the SFC regime, the crack is on the order of the grain size and the entire plastic zone can be confined within a single grain at the crack front without extending to the neighboring grains. Grains adjacent to the selected grains (grains 183 and 1226) were

analyzed and found to have a very stable stress state and negligible evolution in their lattice deformation. In the next paragraphs, only the evolution of the selected grains will be discussed.

In Figs. 4.10 (a) and 4.11 (a), we visualize the orientation of the maximum principal stress vector with the loading axis. In Figs. 4.10 (b) and 4.11 (b), the principal stress jacks have been shown. In both of the grains analyzed here (grains 183 and 1226), the crack does not impinge upon the grain until 36,000 cycles. Prior to 36,000 cycles, the principal stress jacks are fairly stable; their stress state is constant due to the local grain neighborhoods. After 36,000 cycles, as the crack tip interacts and influences the grains of interest, the stress states in the corresponding grains start to evolve, which this stress state evolution will act to facilitate or resist crack propagation through this grain. For grain 183, the evolution in stress state is minimal with the magnitude of the maximum principal stress reducing after 36,000 cycles. Potentially, the reduction of stress in grain 183, as the crack interacts with this grain, leads to a crack arrest mechanism, whereas the crack does not further propagate through grain 183 during the entirety of the experiment. For grain 1226, the stress state significantly evolves, which presumably facilitates crack propagation, as the crack progresses through grain 1226 along a consistent direction. We observed a correlation with the principal stress states in grains ahead of the crack tip and the conformance of the crack to either arrest or continue to propagate in these directions. Similar observations have been made in [126], in which the principal stress metric was discussed as an opening stress on a SFC and the necessity to transition the SFC path to that of Mode I fracture with the applied loading. Moreover, the authors observed the highest correlation between the direction of crack propagation with the alignment of the principal stress [126], which is in agreement with the present study.

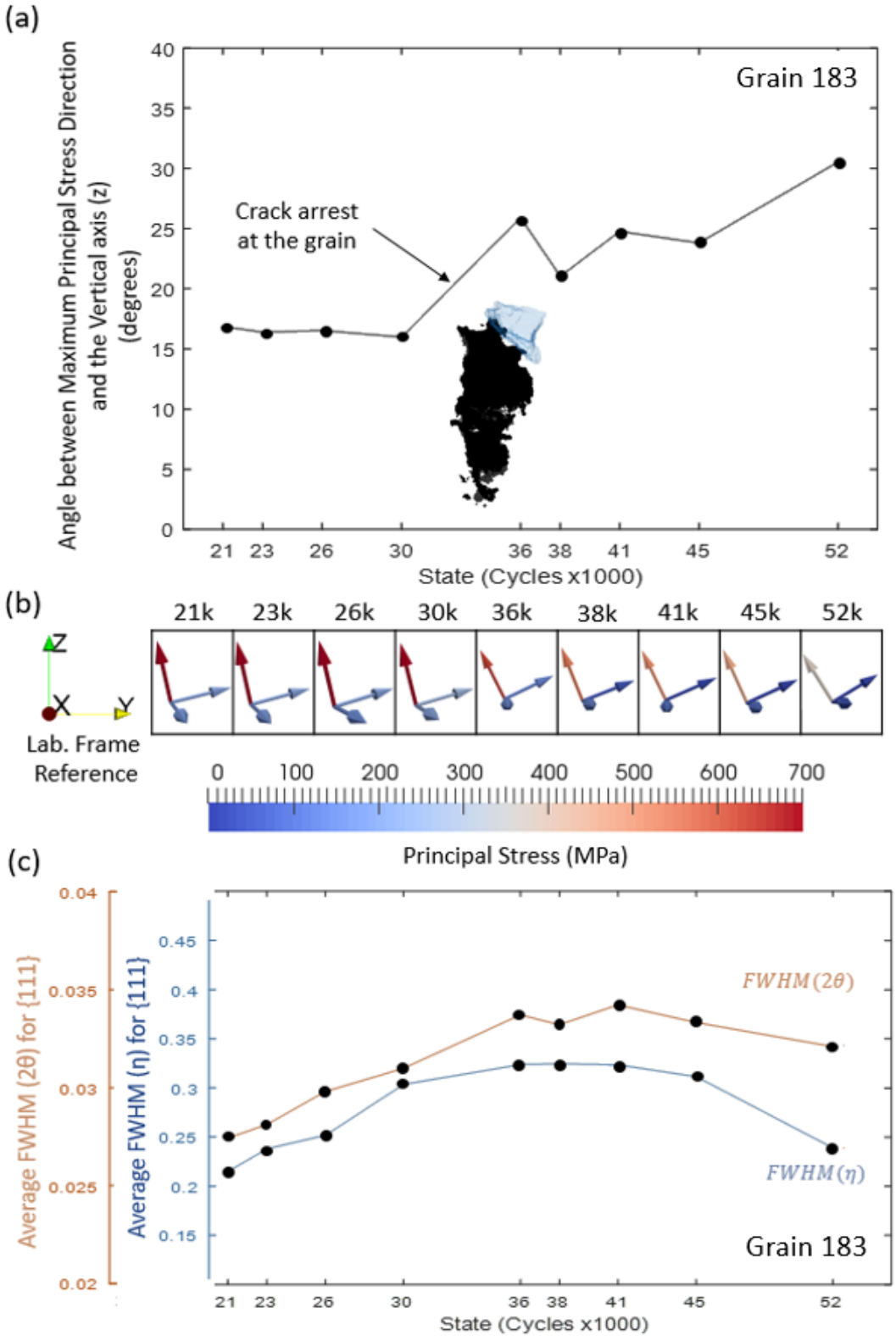

Figure 4.10 Grain 183: (a) the angle between the maximum principal stress direction and the loading axis, (b) the evolution of the stress jacks as the SFC approaches and impinges on the grain, (c) the plasticity in the grain measured through average FWHM along η and 2θ for {111} planes.

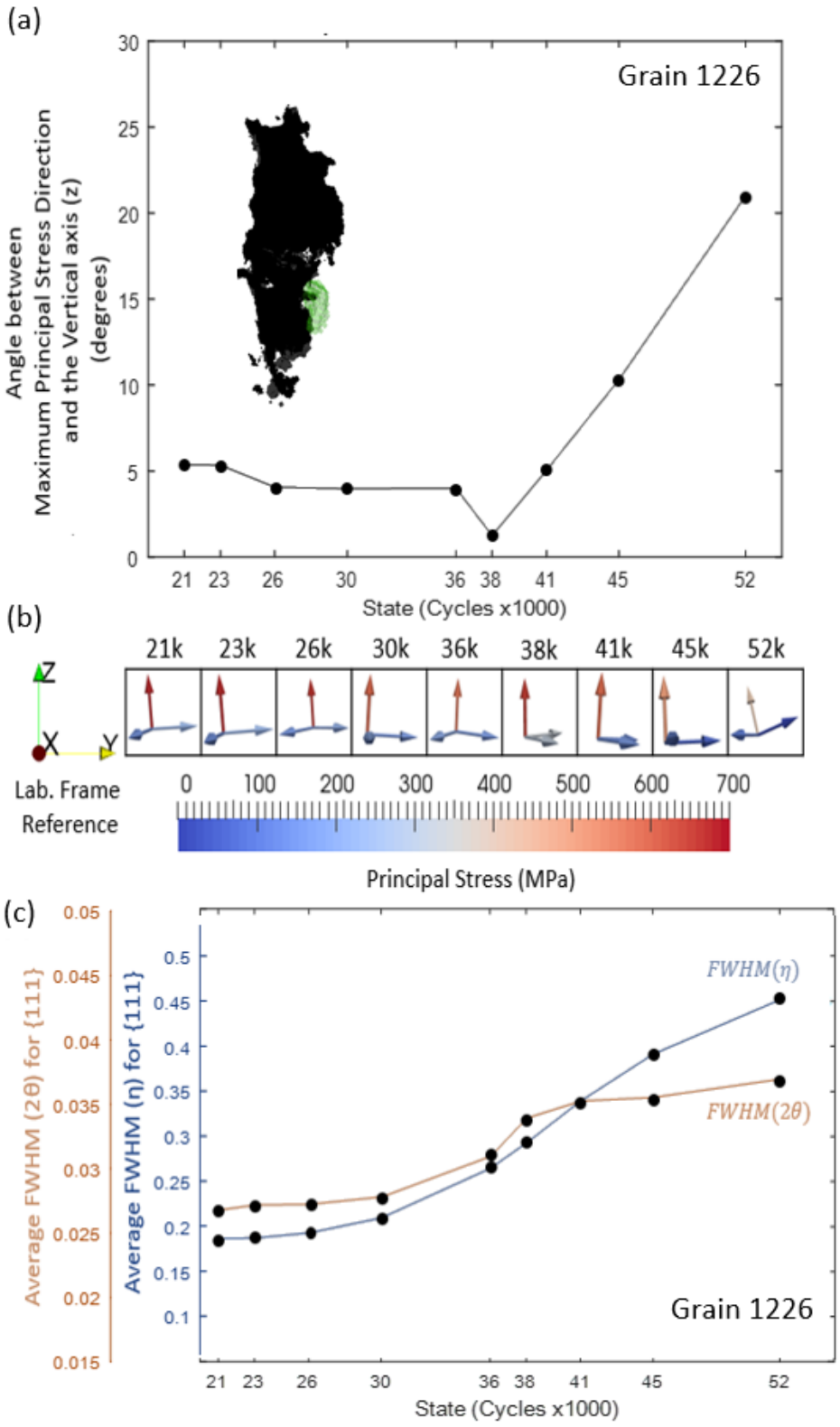

Figure 4.11 Grain 1226: (a) the angle between the maximum principal stress direction and the loading axis, (b) the evolution of the stress jacks as the SFC approaches and impinges on the grain, (c) the plasticity in the grain measured through average FWHM along η and 2θ for {111} planes.

The deformation accommodated in the lattice of the analyzed grains, ahead of the crack front, show a much more interesting trend. The FWHM measures, of the corresponding diffraction spots, for grains 183 and 1226 have been quantified along two polar directions. An average FWHM value along η, which is a measure of lattice curvature, as a surrogate for intragranular misorientation, and average FWHM value along 2θ, which is a measure of heterogeneity in the lattice strains, as a surrogate for the stress gradient at the crack front are calculated. The average FWHM values are calculated from all the spots belonging to the {222} family of planes that were indexed for each grain. Average FWHM are reported, instead of distinct FWHM measures for each individual spot, so that the results are not biased by the direction of the diffraction vector and a single value of the distortion to the lattice is obtained for each grain at each state. Both these measures have been plotted in Figs. 4.10 (c) and 11 (c). It is expected that the damage accommodated in these grains will rise as the crack approaches. For grain 183, the crack starts impinging on it around 36,000 cycles and there is a corresponding increase in damage (please see schematic in Fig. 4.6 (b)). But after 41,000 cycles, with no progression of the crack through this grain, the crack is seen to arrest and both FWHM measures start to decrease (corresponding to a decrease in the intragranular misorientation and stress gradient in this grain as shown in Fig. 4.10 (c)). While for grain 1226, both FWHM measures keep increasing as the crack progresses through this grain in a constant direction (see schematic in Fig. 4.6 (c)). It should be noted again that all the states were characterized, while holding the specimen at the same macroscopic load, so a reduction in the severity of the intragranular misorientation and stress gradients in distinct grains directly ahead of the crack front is unexpected. Obstalecki, et al., observed a decrease in the intragranular misorientation for a specimen subjected to fully reversed loading [57]. In this study, it is expected that the grains directly ahead of the crack tip will be driven into compression when the sample is unloaded (for R=0 loading), which is in agreement with the findings presented in [57]. Typically, the plastic zone ahead of the crack tip is a continuum metric, which is essential for the description of a long crack and associated fatigue crack growth, as discussed in [88,102,117,129–132]. With the present study, emphasizing SFC, we can determine the degree of plasticity and directionality of plasticity in each grain ahead of the crack tip and associate this plastic behavior with the advancement, in terms of both crack path and rate, of the SFC.

All the stress values used in this study have been obtained as grain-average values, with supplemental information provided by reciprocal space mapping, to obtain orientation and strain

gradients within each grain. Lattice strain measurements at higher spatial resolution, within a grain ahead of the crack tip, will become possible with development of future measurement techniques. The subsequent analysis of crack propagation would benefit from techniques that allow us to further zoom into the region of interest through a point focused X-ray beam in a raster schema or dark field X-ray microscopy [149] to retain intragranular spatial fields of orientation and lattice strains.

4.7 Summary and Conclusion

The high scatter in crack propagation rates and high variability in the propagation path and direction makes the short fatigue crack regime extremely difficult to model and predict. And, in the absence of experimental observations, impossible to validate and corroborate. In this paper, we present a dataset at the grain scale; created from careful registration between multiple X-ray characterization techniques to provide a physical basis and scale to our understanding of the short fatigue crack regime. These techniques were pertinently chosen, in order to target and determine the crack path tortuosity and progression with respect to the local microstructural features. The techniques have elucidated the heterogeneity in the evolving mechanical stress fields in conjunction with the deformation state in the grains around the SFC. The SFC was tracked from its initiation, as it propagated through the bulk of the Ni-based polycrystalline sample with ~1700 grains characterized at ten different states through cyclic loading. The interaction of the SFC with ~50 adjacent grains has been studied in detail in regard to these heterogeneous micromechanical fields.

Grain-level stress metrics, such as the von-Mises stress, hydrostatic stress, stress triaxiality and coaxiality of local grains were interrogated with respect to the propagating SFC. In particular, three parts of SFC progression were identified. In two of these parts, the crack grew in an intragranular nature along two parallel planes, during which the stress triaxiality and hydrostatic stresses exhibited high magnitudes, analogous to the opening stress on the crack. Afterwards, the crack formed a bridge across these two crack planes. Low stresses and high values of the stress coaxiality metric were calculated in the grains in the vicinity of the crack bridge, as a result the crack grew in an intergranular fashion to form the bridge. Of note, the intergranular SFC growth was along low energy grain boundaries, which was primarily attributed to their prevalence in this material.

The crack plane and the crack growth direction were observed to align with the most active slip system in a grain. Slip system activity was determined unambiguously by establishing the maximum resolved shear stresses based on the crystallography and the stress-state determined within the individual grains by FF-HEDM. During intragranular crack growth, the crack grows on slip planes and slip directions determined by the τ_{MRSS}; further the normal stress relative to the most active slip plane serves as an opening stress during intragranular crack propagation. The magnitude of the τ_{MRSS} shows a correlation with the crack growth rate within the grain, although more data would be necessary to substantiate this observation.

Throughout this experiment, the crack front progresses in multiple directions through many grains. The SFC path can be determined through the severity of the plasticity in the grains ahead of the crack front, in terms of the FWHM measures for intragranular misorientation or lattice strain gradient for each grain. An association to either the arrest or propagation of the crack, in certain directions, is found through the conformance of the principal stress states in the grains ahead of the crack tip. Arrest in distinct directions is observed, along the crack front, for grains that display a decreasing evolution of the local micro-plasticity.

4.8 Supplementary

The results of the reciprocal space mapping for the grains in the region of interest have been included in the supplementary. In Fig. 4.12, the average FWHM along the η and the 2θ directions have been presented for the {220} family of planes in the top row and for the {222} family of planes in the bottom row. These two families of planes were selected because they correspond to the slip plane and slip direction for the FCC crystal system. Each line in these plots represents the evolution of the FWHM for a specific grain through cyclic loading between 21,000 and 52,000 cycles. On the left, for both FWHM measures, the grains adjacent to the crack are plotted. While on the right, for the FWHM along both η and 2θ, a random sampling of the grains away from the SFC have been plotted. These grains have been plotted to provide a baseline for comparison with the grains that are being influenced by the SFC. It is found that the grains ahead of the SFC front show an increasing trend in both the FWHM measures, as they start being influenced by the SFC. These grains, which show an increasing trend in both FWHM measures, are undergoing plastic deformation and subjected to a stress gradient due to the SFC. The plot

permits the easy identification of the grains directly ahead of the SFC and can be used to define the extent of the plastic zone ahead of the SFC front.

However, the values being plotted in Fig. 4.12, are averaged for all the symmetric planes defined by the families of the {220} or {222} planes. As described in Section 4.6.2, the slip processes are limited to a select set of slip systems, depending on their alignment with the SFC and the macroscopic loading axis. To determine these slip systems, the histograms of the FWHM measures along η and 2θ have been plotted for each individual plane in the {220} and {222} families of planes in Fig. 4.13. For both FWHM measures, the histograms at 21,000 cycles have been plotted in the left column, while in the right column, the histograms for the FWHM measures at 52,000 cycles have been plotted. Thus, the evolution of lattice deformation in the grains around the SFC between 21,000 and 52,000 cycles can be inferred. In the histograms for FWHM along η, we find that the tails of the curve move rightwards to higher FWHM values. This serves as additional proof that only a few select slip systems are activated due to their alignment with the SFC and the macroscopic loading direction. For the FWHM measures along 2θ, we find that the histogram broadens rightwards, to higher values of FWHM. This implies that the elastic strain due to the SFC propagating through these grains is accommodated on multiple planes. In conclusion, from such Figs. 4.12 and 4.13, we can determine the grains ahead of the crack front that are plastically deforming, and more specifically, the select planes that undergo slip activity and the planes, in which elastic strain energy is being accommodated, due to the approaching SFC.

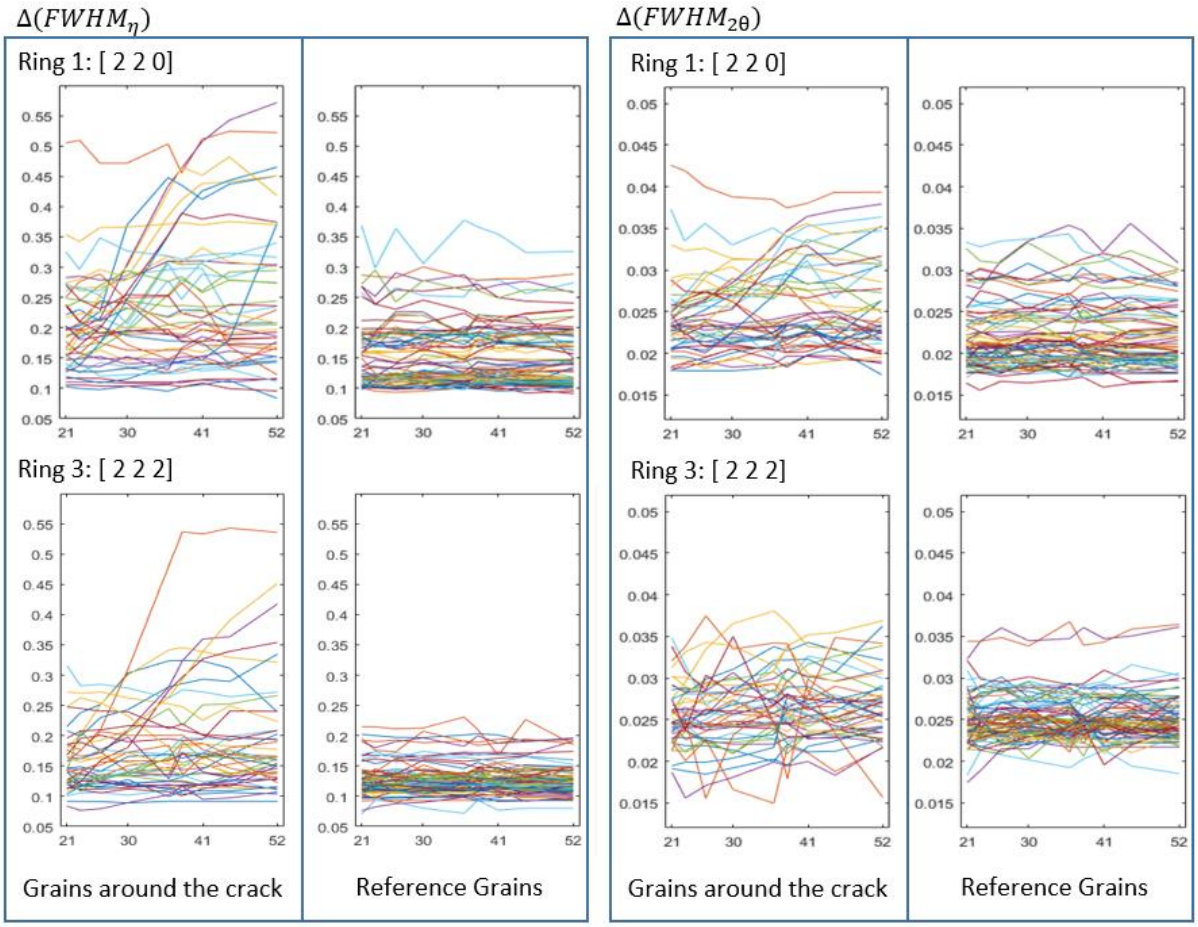

Figure 4.12 Average FWHM along η and 2θ determined for the {220} and {222} family of planes and plotted against the cyclic loading state for grains adjacent to the SFC and a random selection of grains away from the SFC (provided as a baseline). Each color represents a grain averaged value. All FWHM values are in degrees (°).

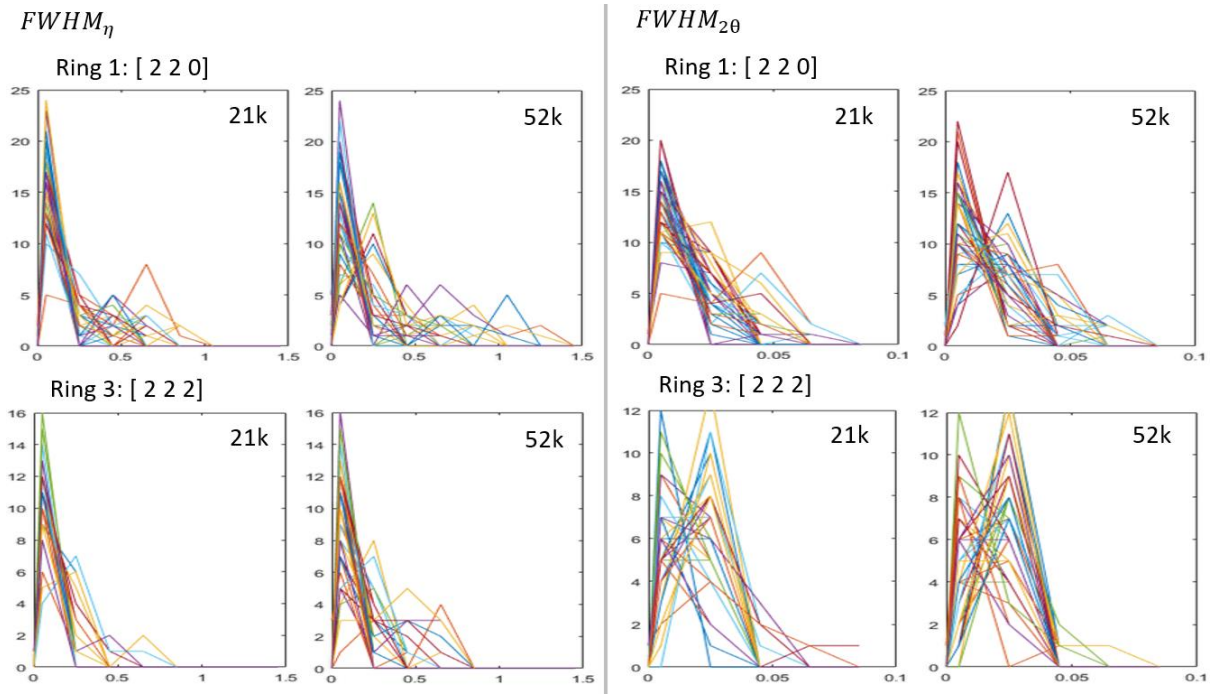

Figure 4.13 Histogram of FWHM along η and 2θ for the {220} and the {222} planes for each grain adjacent to the SFC between 21,000 cycles and 52,000 cycles. Each color represents a grain averaged value. All FWHM values are in degrees (°).

5. VOID COALESCENCE AND DUCTILE FAILURE IN IN718 ILLUMINATED THROUGH HIGH ENERGY X-RAYS

A complete description of the chapter can be found in:
D. Naragani, J.S. Park, P. Kenesei, M.D. Sangid, Void coalescence, and ductile failure in IN718 illuminated through high energy X-rays, (2019), under review.

5.1 Chapter Abstract

Ductile failure through the growth and coalescence of voids is of particular relevance for many engineering materials. Yet, the lack of experimental measures of the mechanical state of the material at the correct length scale has limited further understanding of the regime of ductile failure. In this study, we explore local grain-scale measures for their relevance as a physical basis for ductile failure. Additive manufactured materials, due to the presence of inherent porosity, as well as the ability to tailor porosity, provides a promising avenue to study ductile failure. Selective laser melting is used to manufacture a specially designed specimen with two large, internal voids, in addition to the natural porosity, which is characteristic to the production process. The initial porosity and its evolution upon tensile loading are characterized in this study via micro-tomography. Several locations of void coalescence are captured in the sample, revealing activity of multiple modes of failure. Finite element simulations of a homogenized material continuum, instantiated with the initial void structure, is able to predict the geometrical localizations at the sites of coalescence but does not identify the mechanism. The heterogeneous micromechanical state that is created around voids due to grain interactions, in an industrially relevant polycrystalline alloy, is captured via far-field high energy diffraction microscopy. These experiments determine narrow bands of low stress triaxiality, at the onset of failure, which highlight the path of coalescence through inter-void shearing. Reciprocal space mapping has been interpreted in terms of intragranular plasticity and strain heterogeneity, which can be coupled with high triaxiality to form necessary and sufficient conditions for coalescence through inter-void necking. In this study, the experimentally determined grain-scale description of the micromechanical state has created a physical basis that can accurately capture both the sites and the mechanism of void coalescence at the onset of ductile failure.

5.2 Introduction

Additive manufacturing (AM) offers tremendous potential as a rapid and versatile process to produce parts with complex geometries at a lower cost, material consumption, and environmental footprint than traditional subtractive manufacturing methodologies [150]. However, Ni-based superalloys produced via the AM process are inherently associated with processing defects in the form of microporosity [151]. Rapid qualification strategies are becoming increasingly reliant on modeling and simulations, which have shown varying degree of success in the accurate prediction of the macroscopic response of the material. For example, the peak load, the fracture strain, the path of failure, etc. are easily over-predicted as documented in the Sandia Fracture challenge [33]. The main limitations of constitutive models is in a realistic description of the intrinsic state of the material and the proper calibration of material properties at an appropriate length scale. The level of detail and the length scale that is requisite for this task is an open question, but a suitable approach should have the capability of capturing the complex anisotropic response of the material in the vicinity of sites of eventual failure. It is hypothesized that the grain-scale provides a heterogeneous description of the micromechanical state that can capture all the necessary and sufficient conditions to create a physical basis for understanding the regime of ductile failure. In this paper, we will study void growth and void coalescence in a Nickel-based superalloy produced via an AM process, under tensile loading, through in-situ characterization of the micromechanical state at the grain scale through X-ray experiments.

The mechanisms of void growth and coalescence are three dimensional and stochastic in nature, and a thorough investigation of the size, shape, and relative position of voids, in the bulk of a specimen, presents several experimental challenges. Experimental approaches are often limited to surface observations or post-mortem fractography via optical or electron microscopy. Surface observations are representative only in plane strain conditions like in experiments performed originally by McClintock [152] with a cylindrical hole machined in two-dimensional plates, which others have extended to multiple holes in regular and random arrays [153,154]. Otherwise, in 3D components and samples, surface information can be inconsistent with localizations that exist in the bulk of the material that initiate cracks and may only represent the incipient shear processes before terminal fracture [155]. Noell et al. have conducted detailed fractography to identify as many as seven different failure mechanisms that may be operating within the material facilitating and interacting with one another. Only full-field measurements of the activity in the bulk of the

sample, due to macroscopic loading, can hope to capture all these incipient mechanisms. Experimentally, it is difficult both to manufacture and measure the evolution of a three-dimensional distribution of internal voids, in order to study their interaction during loading. These limitations are overcome, in the present study, via a combination of instantiating the pores through computer aided design prior to the AM build process and micro-tomography characterization.

The geometrical stress concentrations created by the void structure within a material play a significant role in the localization of the structural response of a material. Void growth and coalescence have been classically studied extensively on the continuum scale, through solid mechanics theory and modeling [156–159]. These studies for ductile failure were predicated upon a homogenized description of the continuum with numerical computations with a representative void, [160–162] which are idealizations to explore the fundamental basis of the ductile failure process. Finite element implementations to model the homogenized material with options to describe the flow characteristics and failure criteria in detail [33] are more common nowadays, albeit on idealized pore structures. In this study, a representative pore structure was characterized via μ-CT and used to instantiate a finite element model to analyze ductile failure.

The microstructure of a material plays an important role in the intrinsic properties of the material and the ensuing mechanical response of a polycrystalline sample due to macroscopic loading. The anisotropy created by the grain structure will generate a heterogeneous response from the material in competition with the geometrical stress concentrators. Carroll et al. [163] and Battaile et al. [164] have shown that the variation in effective plastic strain can be as high as 37% and the localization in extreme values can be twice as high as those in the absence of the microstructure. The interaction of voids with internal stresses has also been studied in [165–167] through crystal plasticity simulations, in order to account for the effect of the grain structure, but these approaches would benefit, in terms of calibration and validation, from information at the same scale. The relevance of the grain structure has not been explored via experiments for the mechanisms of ductile failure. Bao et al. [162] created a failure locus of fracture strain as a function of stress triaxiality to demonstrate the importance of stress triaxiality on the incipient mechanisms of ductile failure. The onset of damage before ductile failure can be localized to microscopic ligaments within the material and the stress triaxiality in these ligaments needs to be characterized to ascertain the local competition between mechanisms. Ghahremaninezhad et al. [168–170] used a technique based on the change in grain size to estimate local strain levels on the surface of the

sample. In this study, high energy X-ray diffraction microscopy (HEDM) [47,48,50,67,92,151,171] has been employed to identify and measure the grain-level micromechanics.

The advent of advanced X-ray characterization techniques has enabled the use of high-energy synchrotron X-rays to non-destructively characterize and track the micromechanical state of a test specimen during simultaneous mechanical loading. High-resolution X-ray micro-computed tomography (μ-CT) has been used extensively in the past to interrogate the internal structure of a specimen [106,107,172–175]. In this implementation, μ-CT uses a classic rotation method with a parallel X-ray beam to obtain projections, which help decipher the density variations within the sample and thus aids in the characterization of the void structure (due to the lack of material inside voids) within the bulk of the specimen. The evolution of the size, shape, and position of the voids due to tensile loading can be tracked and locations of failure documented via μ-CT. The μ-CT technique is complemented by far-field high energy diffraction microscopy (HEDM), which uses an identical setup: a single-axis goniometer perpendicular to the incident X-ray beam and a large framing area detector placed further downstream [47,48,50]. Far-field HEDM characterizes the microstructure surrounding the voids in a polycrystalline specimen by determining the centroid position, average orientation, and lattice strain for each grain in the volume illuminated via X-rays. This enables the unambiguously determination of the local stress states (via the measured lattice strains) in the material around the voids in critical regions of the bulk polycrystalline sample. These techniques will be elaborated further in Section 5.4.

Reciprocal space mapping is an X-ray diffraction technique used to determine the intragranular orientation spread and lattice strain heterogeneity in the diffracting grain. High-energy X-ray diffraction techniques have the ability to provide local measurements due to the underlying grain structure because of their sensitivity to the crystal lattice within the grains. However, there is a need to interpret the diffraction-based measures, in terms of classical understanding of plasticity and strain heterogeneity, in order to understand the mechanical response under ductile failure. Pagan et al. [176] have used similar measures to study sub-surface shear band formation, in terms of slip activity, in single crystal samples. In this paper, we offer perspectives on interpreting some intragranular measures determined via reciprocal space mapping and seek their relevance for the regime of ductile failure. Multi-modal X-ray characterization experiments have been performed during a tensile test of an additively manufactured Ni-based superalloy with voids to pinpoint the regime of ductile failure through a comprehensive dataset that traverses several length scales. This

enables a multi-scale analysis of the growth and coalescence of voids to assess the benefit and limitation of each scale and the relevance of a grain-scale analysis for ductile failure.

The paper has been divided into 7 sections. In Section 5.3, the details of the material used in the study are described. In Section 5.4, the techniques used to determine the micromechanical state of the region of interest are detailed. In Section 5.5, the results of the μ-CT, far-field HEDM, and finite element simulations are presented along with the implementation of the Rice and Tracey model [156]. In Section 5.6, a multi-scale analysis has been carried out, in order to assess the important contributions of each length scale in terms of critical attributes and their limitations in assessing ductile failure. This study highlights the potential benefits of a grain scale analysis to understand ductile failure, and finally, in Section 5.7, the overall conclusions from this study are summarized.

5.3 Material

In this paper, we study ductile failure through void growth and coalescence in a Ni-based superalloy, Inconel 718 (IN718), which is commonly used for high temperature applications [1]. In this study, the specimens are produced via additive manufacturing, specifically selective laser melting (SLM), which uses a high power-density laser to melt a thin layer of atomized fine metal powder in successive layers to build a part. The composition of the commercially available, gas-atomized powder can be found in the EOS material datasheet [177]. The AM build was post processed via a three step procedure – (i) vacuum homogenization at 1177℃ for one hour followed by two bar argon cooling at 38℃/h to below 538℃, (ii) solution annealed at 982℃ followed by argon cooling, and (iii) ageing treatment at 718℃ for 8h followed with furnace cooling to 621℃ at which the sample was held for 18h before argon cooling to 149℃. It is important to note these samples were not subjected to a hot isostatic pressing process, to preserve the intentional void structure. The γ phase of the Ni matrix has a face centered cubic (FCC) crystal structure with lattice constant of 0.3595 nm, determined via calibration of the far-field HEDM analysis in this study. The primary strengthening mechanism in this material is through a nanoscale γ'' phase with chemical composition Ni_3Nb and a BCT crystal structure [178]. Also, this material exhibits a γ' precipitate structure with chemical composition of $Ni_3(Al,Ti,Nb)$ and a $L1_2$ ordering structure present in primary, secondary and tertiary sizes [151]. The post-processing resulted in regularized

grains with a random textured suitable for X-ray diffraction experiments. The mean grain size in the material was found to be 48 μm accounting for twins and 80 μm when twins were merged with the parent grains (determined through electron back-scatter diffraction in [151]). The material exhibited a large distribution of grain sizes (20 μm - 220 μm). Complete characterization of the precipitates and microstructure for the same batch of material (in terms of AM and heat treatment) are discussed in detail in references [151,178].

The specimens were designed as cylinders of 6.31 mm and height of 50.80 mm (with height aligned to the vertical build orientation). Additionally, the samples were seeded with two large, internal voids with a nominal diameter of ~400 μm. The two voids lie approximately on the same horizontal plane and are offset from one another by ~400 μm. During the build, a fiducial mark was placed on the top of each specimen to indicate the alignment of the two voids within the cylinder. These voids will, henceforth, be referred to as the seeded voids. The specimens were wire electro-discharge machined to enclose these seeded voids within the 10 mm long gauge section. Further, the cross-section of the gauge was a 1.5 mm X 1.5 mm square with the seeded voids aligned along one of the diagonals (as pre-determined by the fiducial mark), as shown in Fig. 5.1(a). The specimen had several voids due to the SLM process as well, please see Fig. 5.1(b). There is an increased susceptibility of voids to develop around the seeded voids, due to changes in the overall density of material, leading to variations in the heat conductivity path [179]. For the remainder of the study, these voids will be referred to as the natural voids in the sample. Details of the SLM process, as well as the resulting microstructure and properties for IN718 specimens, with respect to the build direction, are discussed in [151,178,180]. Many of the voids in the sample are oblate in shape, due to the vertical build orientation of the specimen, as can be seen in Fig. 5.1(c). Figure 5.1(d) displays the largest cross-section of the seeded voids. There are several natural voids that are above and below this cross-section. The stresses are expected to be localized in slice B (Fig. 5.1(d)) because of the reduced cross-sectional area of the IN718 material, and hence this slice will be discussed in detail in Section 5.5.

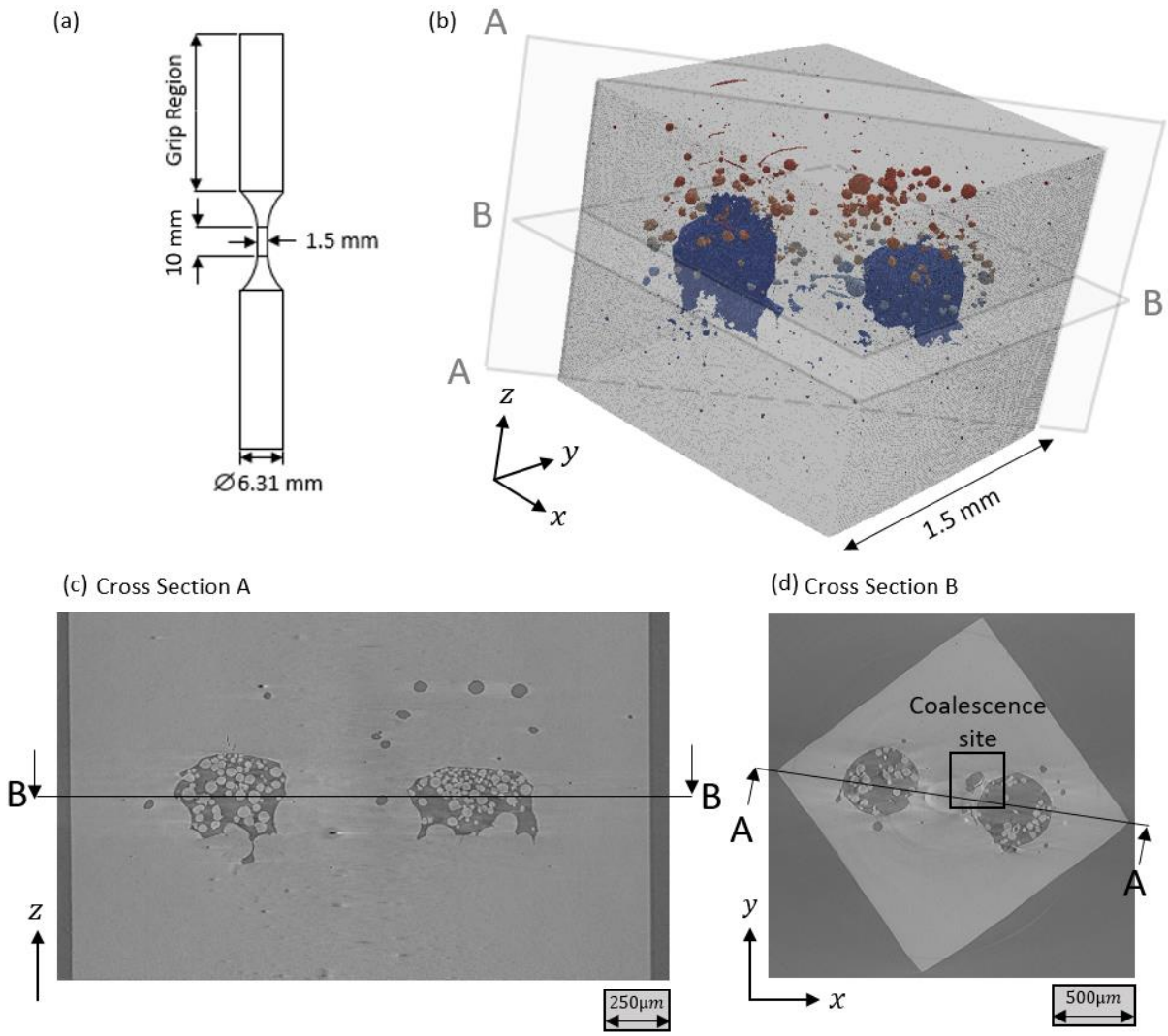

Figure 5.1 (a) Specification of the specimen for X-ray characterization experiments, (b) Void distribution in the region of interest around seeded voids, (c) Cross-section A of the ROI showing the shape of the seeded voids and the natural voids around them, and (d) Cross-section B at the largest area of the seeded voids marked with a void coalescence site that will be discussed in detail.

5.4 Loading and X-ray Characterization Experiment

The in-situ loading and X-ray characterization experiment was performed in the E hutch of beamline 1-ID at the Advanced Photon Source in Argonne National Laboratory. The specimen was loaded via a portable in-house load frame, used previously in [64]. The load frame employs a displacement controlled screw-driven motor to apply a tensile load to the specimen. During loading, a Prosilica GX2750 camera was used to conduct digital image correlation (DIC) on the face of the specimen, in order to determine and track the macroscopic strain state. Loading was guided by baseline stress-strain curves for similar sample geometries with seeded voids. The sample was loaded in displacement control and the tests were interrupted at distinct displacements to perform X-ray characterization techniques. The sample was loaded up to 3.44% macroscopic strain. The states marked in Fig. 5.2(a) will be discussed in the remainder of this paper. States 1 and 2 are chosen to represent the macroscopic strains before and after the macroscopic yielding of this sample. Due to the reduced cross-section in and around slice B, most of the deformation within the gauge length of this specimen are localized in this region. States 5 and 6 are captured before and after instances of void coalescence, respectively, in slice B within the sample.

High energy X-rays at the Re K-edge corresponding to energy, E = 71.676 keV, and a wavelength, λ = 0.172979 Å, are used to characterize the 1.5 mm X 1.5 mm square cross-section of the Ni-based superalloy. Two X-ray techniques are employed throughout this study in sequence. First, μ-CT was performed in the parallel beam configuration using an area detector with a 3 mm field-of-view and 1.5 μm pixel size, at ~100 mm distance from the sample. The X-ray beam size used for μ-CT in this study was 1.5 mm tall and 2.5 mm wide. The sample was rotated over a 360° angular range and radiographs were captured after every 0.2° increment. The posts of the load frame blocked the direct X-ray beam for an angular range of ~25°, while rotating along the loading axis (ω). The scans were reconstructed through TomoPy [181]. The missing projections have been calculated through the use of ω frames before and after the beam was blocked in the procedure described in [107]. Finding the region of interest was fairly straightforward, since the large seeded voids were visible in the radiographs. Noise was reduced via a median filter along with erosion and dilation processes within ImageJ [182]. Ring artifacts were suppressed through the Gaussian localization of the ring center in Hough parameter space followed by polar transformation and removal of the obtained linear stripes through a median template filter [183], the entire algorithm has been outlined by Jha et al. [42]. The voids inside the region of interest have a darker intensity

in the reconstructed images, which was used for segmentation. The statistics of the void distribution and its evolution upon loading is discussed in Section 5.5. Voids as small as 3 μm^3 could be detected at the resolution limit, according to the Nyquist theorem. Upon µ-CT analysis, we observed unmelted, loose powders trapped within the seeded voids. Due to the low packing density of these powders, they did not carry load and influence the subsequent experiment. In Fig. 5.2 (b-f), the evolution of the region of interest is depicted. After 0.9% strain, the sample experiences macroscopic yielding, and by 3.08%, necking of the sample can be clearly observed in the radiographs, please see Fig. 5.2 (e-f). Between 3.08% and 3.44%, void coalescence occurred at a few locations around the large seeded voids. Two of these locations have been marked in Fig. 5.2(g).

The state of the grain structure around the voids was characterized through far-field HEDM. Far-field HEDM requires a setup identical to µ-CT except with a flat panel detector with a large field of view kept further downstream. An amorphous silicon flat panel detector with an array of 2048 X 2048 pixels and 200 µm/pixel was placed ~850 mm from the sample. The sample was rotated along the loading axis over a range of 360° and frames were saved every 0.25°, while the sample was illuminated by an X-ray beam 30 µm tall and 2.5 mm wide. A 30 µm beam was chosen, in order to capture the large range of grain sizes in this material considering accurate indexing of all associated diffraction spots is limited by the dynamic range of the detector. Twenty scans were used to characterize the 600 µm tall volume, centered around the large seeded voids. Re-centering around the region of interest after each load state is crucial for tracking the indexed grains. A rigid body translation in the vertical direction is informed by loading displacements measured by DIC and employed for correction of the sample position, as described in [64]. This correction facilitated the re-centering of the region of interest in the X-ray beam.

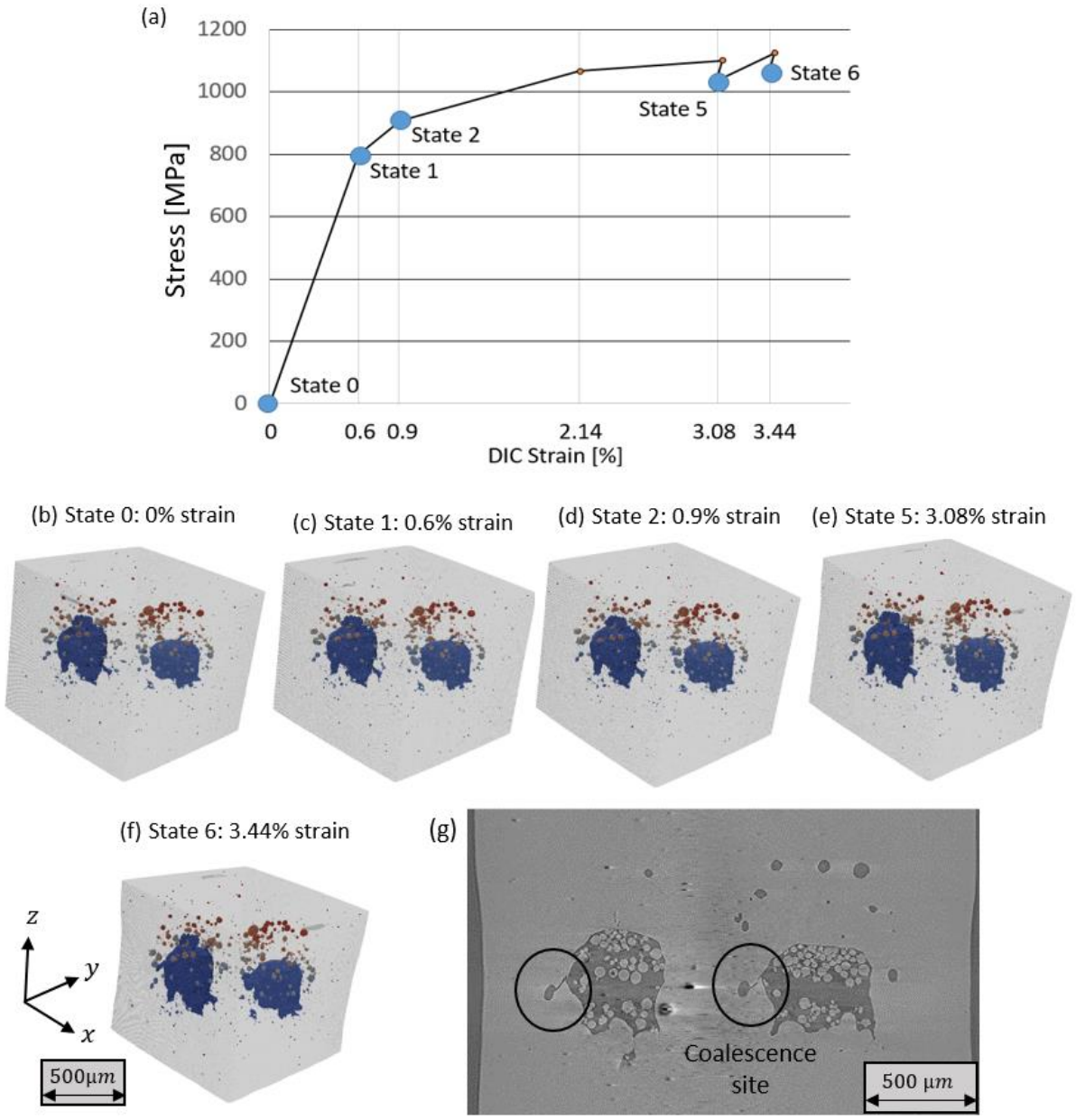

Figure 5.2 (a) Macroscopic stress vs. DIC strain curve. States which will be discussed in this paper have been indicated, (b)-(f) μ-CT reconstruction and segmentation results at each characterized state. The onset of ductile failure is captured through macroscopic necking at State 5 (e) and 6 (f), (g) Sites of void coalescence in cross-section A are shown at State 6.

Grains were indexed by using the third through eighth Debye-Scherer rings corresponding to the {220}, {131}, {222}, {040}, {331}, and {240} lattice planes. The inner rings were attenuated using lead tape, in order to obtain higher intensity on the outer rings to obtain higher strain resolution. The setup was calibrated, and the scans were reconstructed through the microstructural imaging and diffraction analysis software (MIDAS) [51,52]. The reconstructions provide the grain centroid position, grain averaged orientation, and the grain averaged lattice strain for each grain illuminated in the region of interest. A spatial resolution of ~20 μm for the centroid position, an angular resolution of 0.1° for the orientation, and a lattice strain resolution of 1e-4 are commonly reported for the far-field HEDM technique [52,53]. The indexing procedure relies on accurate determination of the centroid of a diffraction spot, a task that becomes increasingly difficult with spot spreading due to deformation of the diffraction grain. The search space was seeded with orientations of grains found in the initial state and their positions and strains were refined for successive load steps, in order to improve the accuracy of reconstruction at higher strain states. Approximately 150 grains were found in each 30 μm box at the initial state. The results will be discussed in Section 5.5. The stress is calculated from the lattice strains through the single crystal stiffness tensor for IN718 provided in [184] with C_{11}= 242.36 GPa, C_{12} = 139.73 GPa and C_{44} = 104.44 GPa. The stiffness tensor was confirmed via a series of modeling efforts for this material, as described in [167].

Spot spreading is primarily due to the deformation of the lattice in the diffracting grain. The damage to the lattice can be broadly divided into two contributing, yet distinct, parts: the curvature in the lattice and the distribution of the lattice strains within the grain (i.e. an elastic strain gradient). Since X-ray diffraction measures the orientation of the lattice planes and the lattice spacing with high resolution, it is inherently able to capture these curvatures and heterogeneities within a grain. In an ideal case, the well order lattice within a grain, between voids, will have perfectly aligned lattice plane normals and a lattice spacing that is consistent throughout the grain, as shown in Fig. 5.3(a). This results in a sharp and well defined diffraction spot. In Fig. 5.3, a schematic of the evolution of two voids are shown, where the radius of the initial spherical voids is indicated by R^i, and after growth of the voids, the major and minor axes of the voids are indicated by R_0^f and $R_{\pi/2}^f$, respectively (with notation adopted from [156]). Hence, as the voids grow ($R_0^f > R^i$) and the spacing between the voids reduces ($S^f < S^i$), the geometric deformation is accommodated by the lattice of the grains through their curvatures and strain heterogeneities, as shown in the schematic

in Fig. 5.3(b). Commonly the spot spreading is quantified through the full width at half maximum (FWHM) metrics, along two decoupled polar directions. Along 2θ or the radial direction, the FWHM corresponds to the heterogeneity in the lattice strains within the grain [57,58]. The FWHM along η (along the azimuth on the detector) or ω (across frames during rotation of the sample) corresponds to the curvature of the lattice planes within the grain [57,59]. In this polycrystalline sample, multiple grains accommodate the deformation in the region of interest. An in-house code was developed in an effort to quantify this damage within the grains via the FWHM measures on all diffracting planes. A virtual diffraction simulation, as described in [58], was adapted from algorithms in MIDAS and used to determine the peak positions from the reconstructed grains. The simulator was coupled with an extraction and thresholding procedure, in order to determine the FWHM of all the spots indexed to a grain.

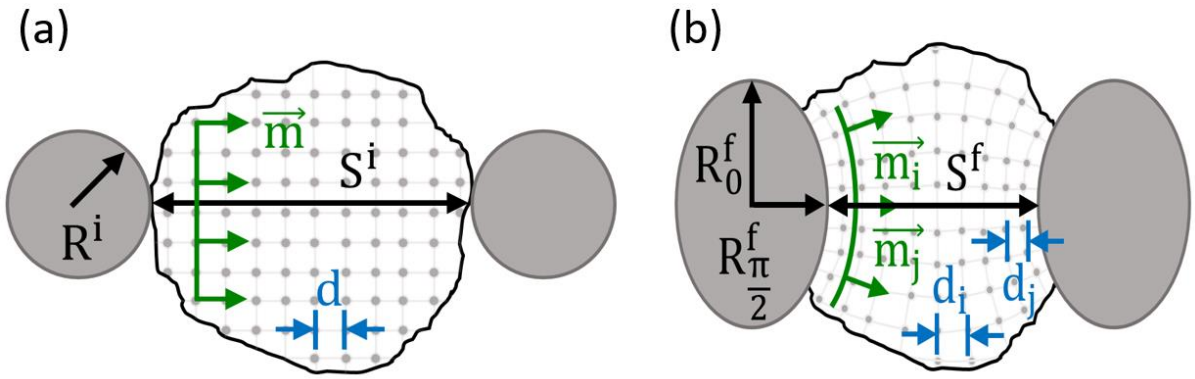

Figure 5.3 Schematic of lattice deformation in the matrix within the inter-void region represented through a single grain at (a) the initial state, before loading, with a well ordered lattice and at (b) after void growth, due to a macroscopic load, with damage accommodated through lattice curvature and intragranular strain heterogeneity.

5.5 Results

The registration between the multimodal X-ray characterization techniques of μ-CT and far-field HEDM is necessary to accurately determine and track the grains around the voids. In Fig. 5.4(a), the grain centroid and void distribution, determined from the two techniques, have been compiled and consolidated. After consolidation, a pipeline in Dream3D was used to create a

Laguerre tessellation from the grain centroids, in order to fill the scanned volume and render the region of interest. Laguerre tessellations are weighted by the size of the grains, which are correlated to the relative intensity values of the diffraction spots through MIDAS, and thus, represent a truer representation of the microstructure within the region of the interest (Fig. 5.4(b)). The grains in the slice at the center of the gauge, around the two large seeded voids and several smaller natural voids, will be shown in the remainder of this section, please see Fig. 5.4(c).

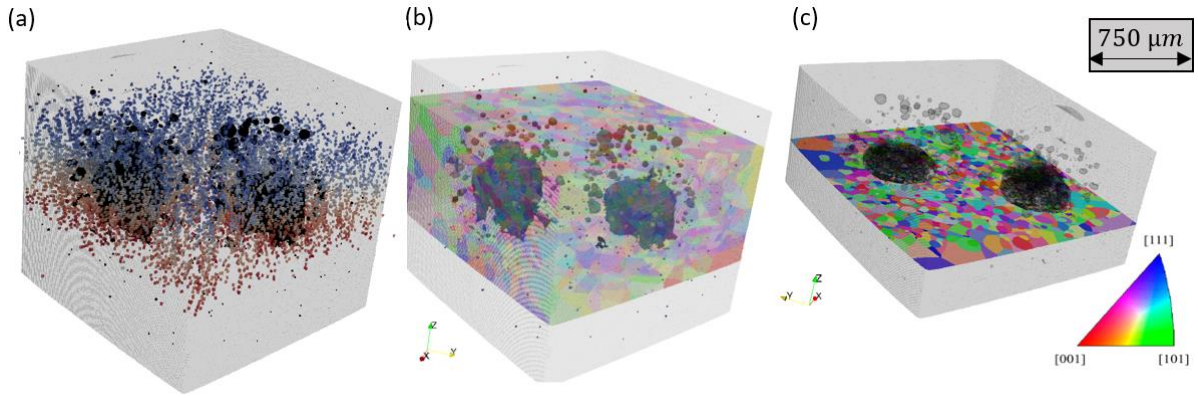

Figure 5.4 (a) Scatter plot of the grains found through far-field HEDM reconstruction after registration with the void distribution in the specimen determined through μ-CT. (b) Laguerre tessellation performed in Dream3d to render the region of interest. (c) Grains in cross-section B, around the voids have been extracted for further analysis.

5.5.1 Void evolution

The change in porosity due to tensile loading has been determined via μ-CT and depicted in Fig. 5.5(a). The majority of the initial volume of voids is due to the two large seeded voids in the gauge section. As expected, the porosity increases with tensile loading. The slope of the initial segment, before 0.6% strain, is fairly gentle, as the material is predominately elastically loaded. The increase in porosity is almost entirely due to the growth of the two seeded voids. The increase after 0.6% and before 3.08% strain is very stable. Between these states, the sample is macroscopically plasticizing. Between 3.08% and 3.44%, voids coalesce at a few locations, please

see Fig. 5.2(g). The rupture of the material between these voids causes a sharper increase in the amount of porosity. The sample fractures right after 3.4% macroscopic strain.

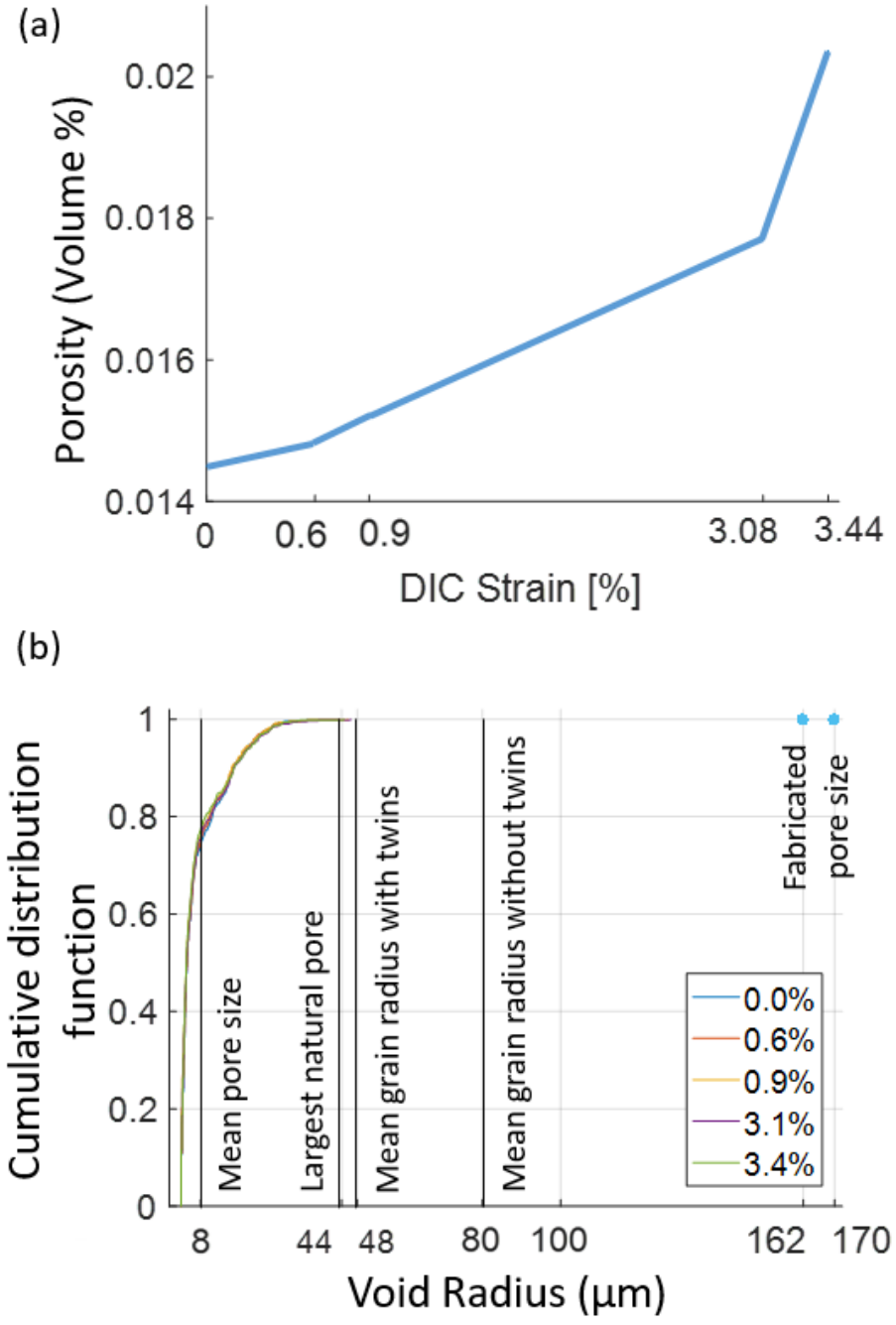

Figure 5.5 (a) Change in porosity due to macroscopic loading and (b) the cumulative distribution function of the equivalent spherical radius of the voids with reference to the grain size (from EBSD) and the size of the seeded voids.

In this study, we have a large range of void sizes, as shown in Fig. 5.5(b). The smallest void that can be detected is 2 pixels wide in each dimension, which for the current detector is equivalent to a sphere with a radius of 1.5 μm. The mean natural void radius, at the initial state, is 8 μm, while the largest natural void found at the initial state is 44 μm. The natural voids are a consequence of trapped gas during the AM build and are either spherical or slightly oblate along the tensile axis of the specimen. No keyhole or lack of fusion-bonding type voids were observed in these specimens. The seeded voids, manifesting from the computer aided design of the part, are 162 μm and 170 μm in equivalent spherical radius at the initial state. Likewise, the seeded voids are initially oblate in shape aligned with the tensile axis of the sample. The growth of voids is not isotropic in nature; the voids elongate in the tensile dimension, while they contract in the transverse dimension [156]. Therefore, the voids in the sample become prolate with tensile loading. The growth of the voids is tracked by calculating an equivalent spherical radius which is a close but approximate measure of the actual oblate or prolate shape of the void. Thus, the change in the cumulative distribution function of the equivalent void radius, with tensile loading, is minimal (Fig. 5.5(b)) despite the change in total porosity captured in Fig. 5.5(a). The implementation of the Rice and Tracey model to account for the non-uniform growth of the voids will be discussed in Section 5.5.3.

5.5.2 Finite element simulation

Classical models for ductile failure are predicated upon a homogenized description of the material; often in an idealized fashion with a single void in a unit cell or a well ordered distribution of voids generally of the same size. This conventional rendition is useful in understanding the mechanisms of ductile failure, but, is not representative of real materials which have a stochastic distribution of void shapes, sizes, and locations. First, a finite element simulation was initialized with a homogenized material description and an identical state of void distribution, as that captured for the sample upon the initial μ-CT characterization. This allows us to bridge the rationale behind the conclusions from classical studies of void growth and coalescence (representing the mechanical state due to the actual void distribution), while providing a comparison to the micromechanical state identified from the HEDM experiment. A linear elastic-plastic material model with J2 plasticity (determined from the macroscopic stress-strain data [151]) was used in

Abaqus to describe the homogenized continuum. The voxelized μ-CT data was meshed in Paraview. The distribution of the micromechanical fields from the simulation have been depicted in Fig. 5.6, specifically the total strain component in the loading direction, the stress in the loading direction, the hydrostatic stress, and the stress triaxiality (which is defined as the ratio of the hydrostatic stress to the von Mises stress). Through this simulation, we can determine the local value of these stress measures in the sample due to the actual shape, size, and location of the voids.

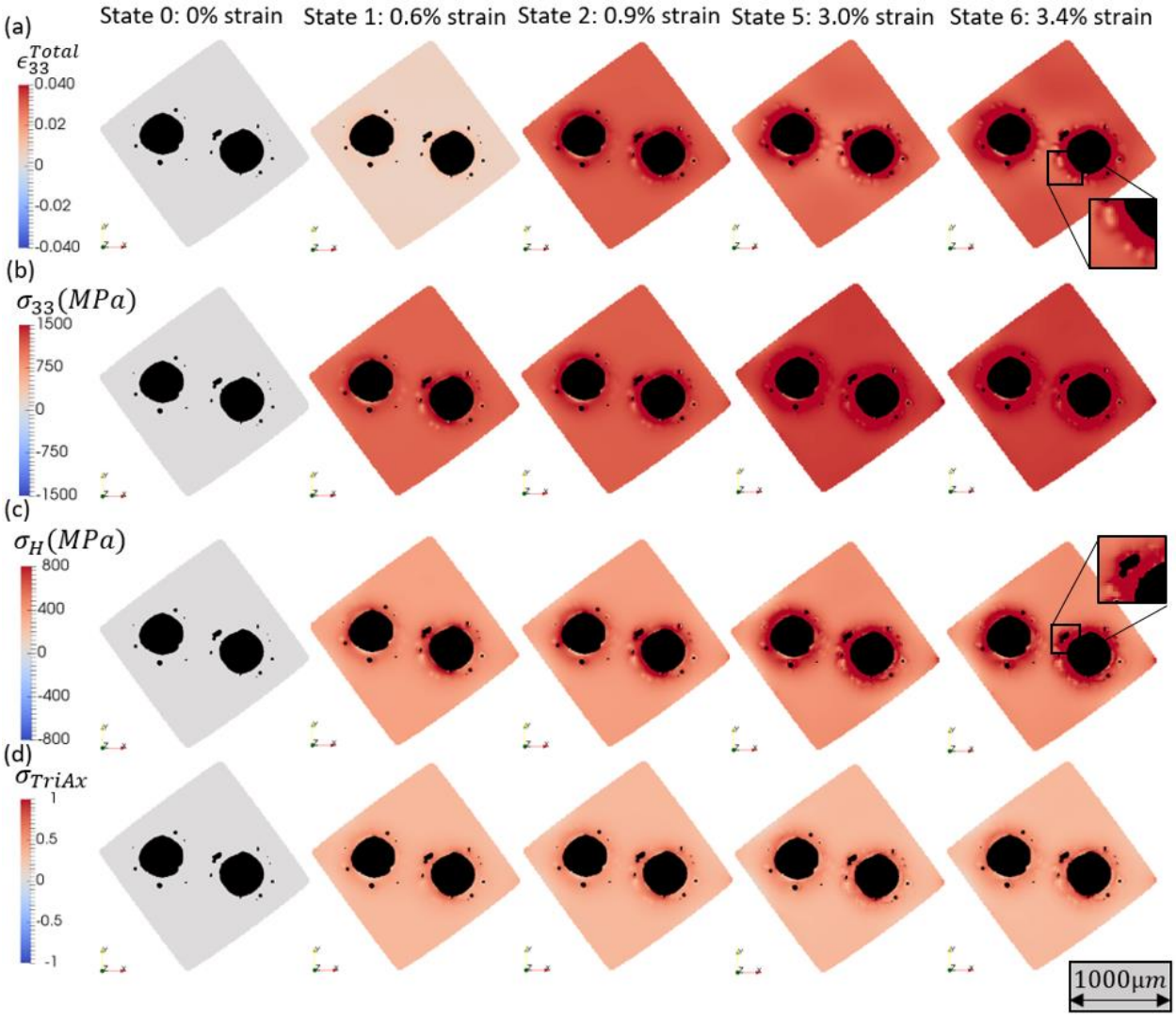

Figure 5.6 Results of the elastic-plastic FEM simulation of the homogenized continuum for cross-section B: (a) total strains in the loading direction, (b) stress in the loading direction, (c) hydrostatic stresses, and (d) the stress triaxiality.

The stress in the loading direction is high in the transverse plane containing the voids. As expected, the hydrostatic stress and the stress triaxiality are concentrated in the inter-void region (between the seeded voids and natural voids) as shown in the inset in the last column of Fig. 5.6(c). A high value of these stress measures is associated with rupture in the material, which is described through nucleation of secondary voids [158,185,186], typically an order of magnitude smaller in size than the primary voids, that accelerate the damage process. Moreover, another perturbation to the micromechanical fields is observed due to natural voids existing above and below the plane shown in Fig. 5.6. These natural voids create low stress regions in the slice shown, please see inset in the last column of Fig. 5.6(a). This creates sharp gradients in the stress fields. From the continuum simulations, we observe that several factors, including the shape, size, and proximity of the voids, play a role in the micromechanical response. The inter-void region will be discussed further in Section 5.6, in order to understand the mechanism of void coalescence in 3D.

The two seeded voids have high stresses around them, since they act as stress concentrators. These stresses are very high, even at 0.6% macroscopic strain, which is before the macroscopic yield point. This stress concentration explains why the large seeded voids start to grow much before the macroscopic yield for the material (as mentioned in Section 5.5.1). The natural voids show similar stress concentrations but to a lesser degree due to their smaller size. Some natural voids have irregular shapes, which increases the stress concentration around them, please see inset in last column of Fig. 5.6(c) for an example. With successive loading, the stress fields around the large seeded voids expands and is superimposed with the stress field around the adjacent smaller natural voids. Between 3.0% and 3.4% macroscopic strain, several natural voids coalesce with the bigger seeded voids, as shown in Figs. 5.1(d) and 5.2(g). These regions have been extracted and will be discussed in Section 5.6.

5.5.3 Grain-averaged micromechanical state

The average grain size for this material is 48 μm, when twins are considered as separate grains. As previously mentioned, the grain size distribution is broad, implying that there are very small and very large grains in this material [151]. More heterogeneity in the strain response around the void is expected, as the ratio between the void size and the grain size decreases [163]. Thus to understand the failure mechanism, it is necessary to incorporate the evolution of the

micromechanical state of the grains, especially around the voids. The lattice strain and stress distributions, determined from the far-field HEDM characterization of the region of interest, have been shown in Fig. 5.7. Immediately, the heterogeneity in stress distribution due to the microstructure is evident. Small misalignments from the load frame and imbalances in the sample, due to the distribution of voids, result in a slight bending load present in the initial stages of the experiment. As shown in the first column of Fig. 5.7, the sample developed a small tensile load towards the left corner of the images shown and a compressive load towards the right corner. There are also small variations due to the type II residual stresses in the microstructure. The initial state and the type II residual stresses in the grains are very small but can affect the response of the material [187].

With successive loading increments, the strains and stresses increase in the cross-section shown in Fig. 5.7. From the plots for the hydrostatic stress and the stress triaxiality in Fig. 5.7(c-d), the stresses concentrate around the two large seeded voids, but are extremely heterogeneous from 0.6% onwards. The stresses concentrate at the center of the sample and towards the left corner by 0.9% strain. Between 3.08% and 3.4% strain, some cases of void coalescence occur which relaxes the stress in several locations [188]. Far-field HEDM relies on the accurate determination of the centroidal position of the diffraction spots on the detector, which are used to measure the lattice strains in each grain. After the sample has been significantly deformed, these diffraction spots start spreading, images of spot spreading have been shown previously for this material in [151]. This leads to higher possibility of errors for the elastic strain determined for each grain. At the same time, the values of the FWHM, determined from reciprocal space mapping, become significant and useful to explain the mechanical behavior. All the grains found in the initial state have been identified and their orientations are seeded in subsequent reconstruction analyses through the six loading states, in order to reliably track the lattice strains evolution in each grain. The damage in selected grains, around coalescence sites, is determined from reciprocal space mapping of their respective lattice structures and will be discussed in Section 5.6.

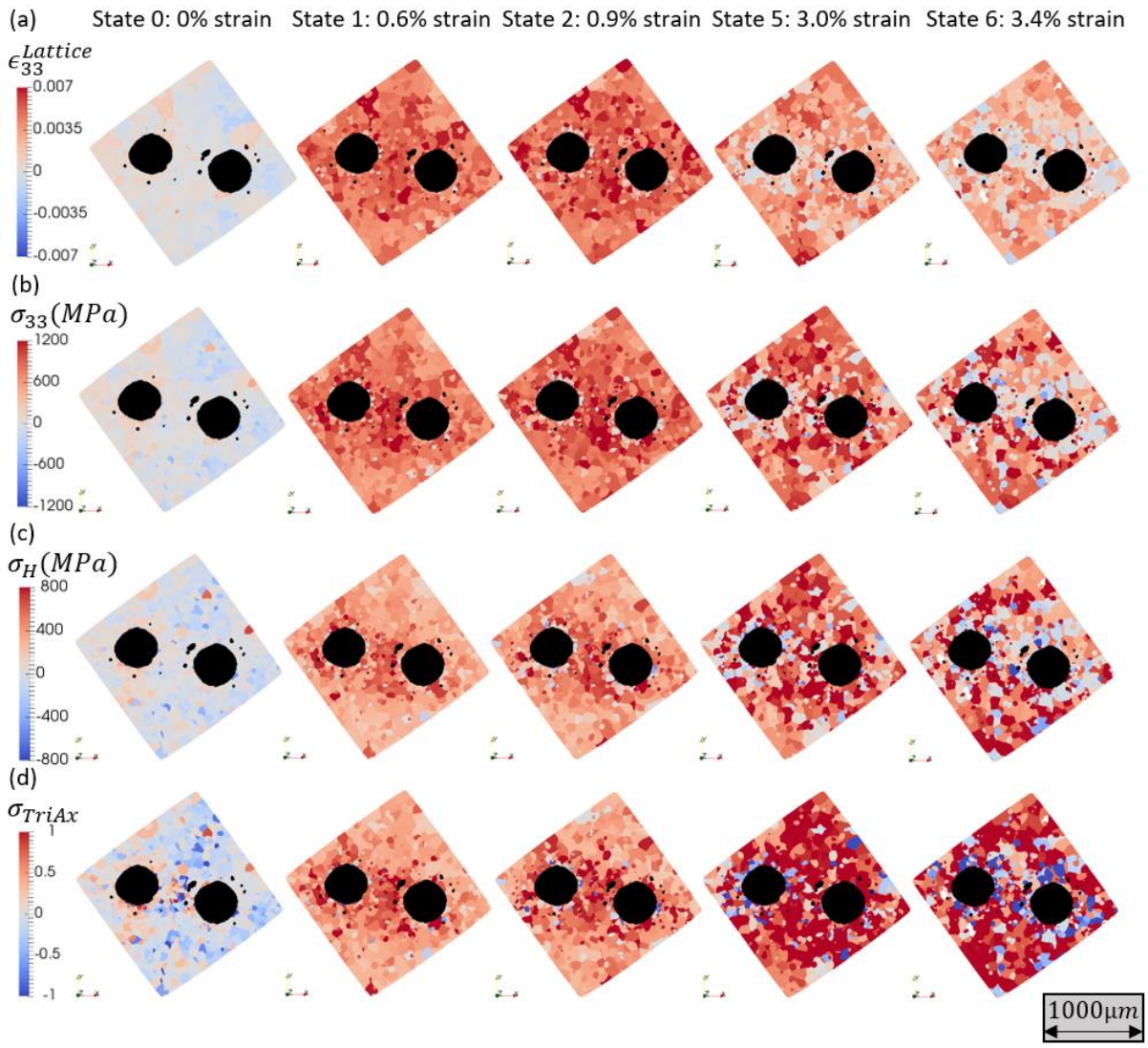

Figure 5.7 Results from the far-field HEDM reconstruction for cross-section B: **(a)** lattice strains in the loading direction, **(b)** stress in the loading direction, **(c)** hydrostatic stresses, and **(d)** the stress triaxiality.

5.5.4 Rice and Tracey model

Rice and Tracey [156] described a variational principal to characterize the flow field in an elastically rigid and incompressible plastic material, containing an internal spherical void or voids, subjected to a remote stress field. The evolution of an initially spherical void with radius R^i is described through the following relation:

$$R_0^f = \left[\exp(D\varepsilon_t) + \frac{1+E}{D}(\exp(D\varepsilon_t) - 1)\right] R_0^i \tag{5.1}$$

$$R_{\frac{\pi}{2}}^f = \left[\exp(D\varepsilon_t) - \frac{1+E}{2D}(\exp(D\varepsilon_t) - 1)\right] R_{\frac{\pi}{2}}^i \tag{5.2}$$

Where R_0^f and $R_{\frac{\pi}{2}}^f$ are the principal radii of the ellipsoidal void in the tensile and transverse directions, respectively. The macroscopic true strain, in the loading direction, is given by ε_t. In Eqs. 1 and 2, the growth of a void is established as the superposition of a uniform volume changing term (described by a scalar D) and a shape changing term (described by a scalar 1+E). The dilatational field, D, is defined as follows:

$$D = 0.588 \sinh\left(\frac{3}{2}\frac{\sigma_H}{Y}\right) + 0.008 \cosh\left(\frac{3}{2}\frac{\sigma_H}{Y}\right) \tag{5.3}$$

According to Rice and Tracey, the shape changing term is dependent on the hardening behavior of the material, where E = 5/3 is appropriate for strong hardening or very low triaxiality in a non-hardening material or E = 2 is appropriate for weaker hardening or higher triaxiality in a non-hardening material. For the present material in this study, E = 2 is appropriate to describe the shape changing behavior. In Eq. 3, the ratio of the hydrostatic stress (σ_H) and the yield stress (Y) represent a form of the stress triaxiality, which is determined by [174,189], as follows:

$$\frac{\sigma_H}{Y} = \frac{1}{3} + \ln\left(1 + \frac{1}{2}\sqrt{\varepsilon_t - \varepsilon_n}\right) \tag{5.4}$$

The necking strain (ε_n) is determined from the intersection of the true stress (σ_t) and the work hardening rate $\left(\frac{d\sigma_t}{d\varepsilon_t}\right)$ curves as a function of the true strain (ε_t). The stress-strain curves from [151] were used for calculating ε_n, which was found to be 0.55%.

The above equations were used to determine the expected growth of an internal void or voids for the actual sample. The true change in the tensile and transverse dimensions of all the voids in the sample has been determined through μ-CT. The cumulative change in the dimensions of the voids in the region of interest has been plotted in Fig. 5.8(a) with solid lines. The curves of the prediction of the model have been plotted in Fig. 5.8(a) through dashed lines. The Rice and Tracey model displays a good agreement with the experimental measurements. From the graph, the model provides an incomplete description of this behavior at two particular locations – the macroscopic yield point of the material and the point prior to material failure. The reason behind these deviations will be discussed in Section 5.6.

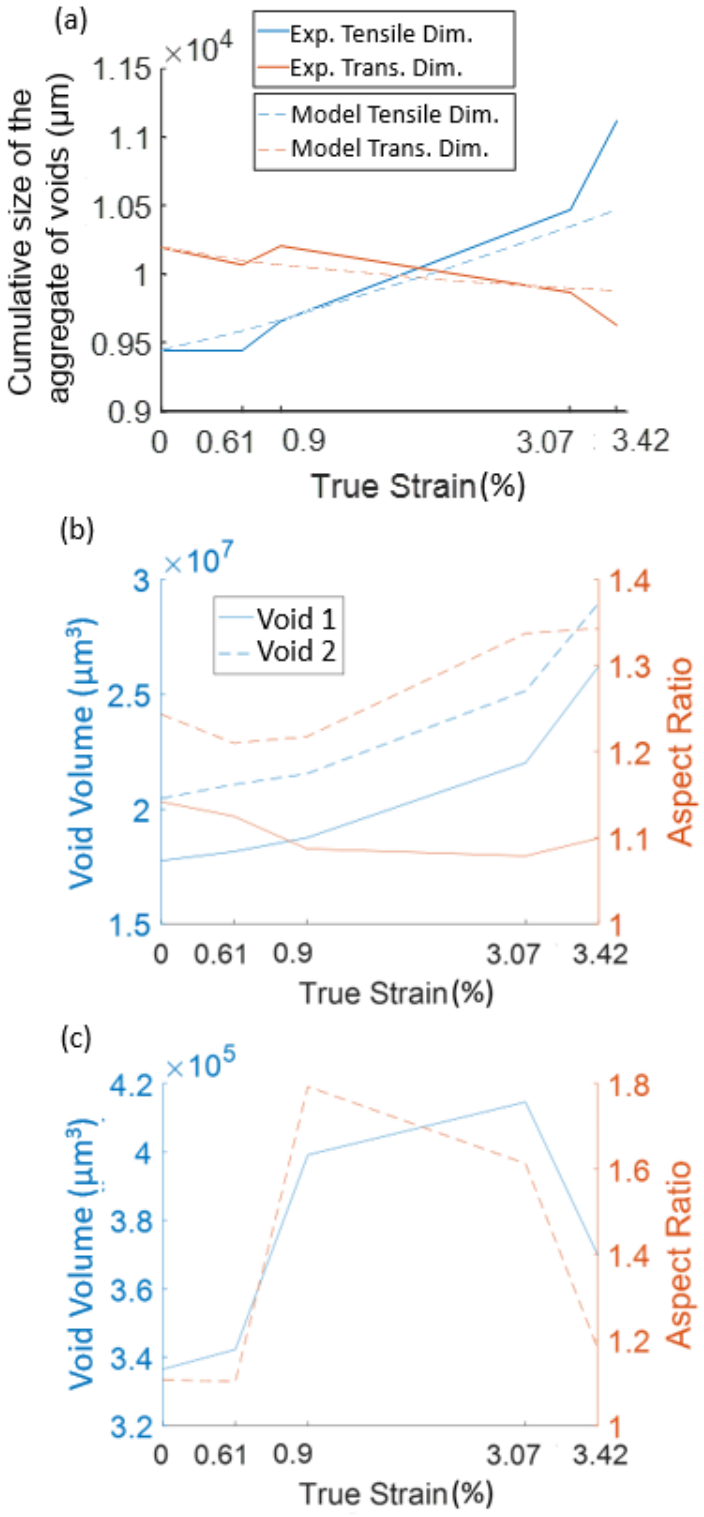

Figure 5.8 (a) Comparison between the cumulative dimension of the aggregate of voids, in the tensile and transverse directions, determined from the µ-CT reconstruction and predicted by the Rice and Tracey model. The change in void volume and aspect ratio (shape distortion) of: (b) the large seeded voids and (c) largest naturally occurring void in the region of interest.

5.6 Discussion

The Rice and Tracey [156] model has been implemented for the present specimen by employing information from the macroscopic true stress-strain curve and shows good agreement with the growth of the aggregate of voids captured through μ-CT. As shown in Fig. 5.8(a), the model predictions deviate from experimental observation of the cumulative change in the dimensions of the voids around the macroscopic yield point and after 3.08% macroscopic strain is applied. The deviation at the macroscopic yield of the material was due to ambiguity in determining the true strain at necking, while the deviation after 3.08% strain is due to coalescence events. The Rice and Tracey model [156] captures the experimental trend, because it is based on a macroscopic definition of stress triaxiality, which in this implementation, adopted from [174,189], is based on the change in the tensile and/or transverse dimensions of the specimen's cross-section for the necked region. Since void nucleation is bypassed, due to the presence of inherent porosity from the AM process, the increase in the tensile dimension and associated decrease in the transverse dimension in the necked region (as shown in Fig. 5.2(e,f)) is accommodated by deformation of the voids present. Due to its concurrence with experimental results at the specimen scale, the Rice and Tracey model has been widely adopted. However, if the evolution of each individual void is checked, as shown in Fig. 5.8(b-c), the Rice and Tracey model is more applicable for the large-seeded voids than the smaller natural voids in many cases.

The failure criteria for a specimen scale implementation of the Rice and Tracey model [156] is based on achieving a critical change in the dimensions of the voids (ratio of final longitudinal to initial longitudinal dimension). The only physical attribute that is considered at this scale of analysis is, therefore, the effective porosity or void fraction. Coalescence is not considered explicitly in the Rice and Tracey model and thus for the present study, after state 5, at 3.08% macroscopic strain, the experimental results significantly deviate from the Rice and Tracey predictions. Though the deviation in Fig. 5.8(a) might seem subtle, local variations in the response of the material can result in large changes in the effective fracture strain and is thus insufficient to properly understand ductile failure, let alone predict fracture strain. The basis of the Rice and Tracey model [156] is the role of the stress triaxiality in driving the growth of voids, which is explored further in the next paragraph at the microscale.

A homogenized description of the material in a linear elastic-plastic finite element simulation that has been instantiated with the exact size, shape, and location of all voids within the specimen

is able to accurately predict the potential sites of coalescence around the seeded voids. The homogenized material model is effective, because it can capture the stress concentrations due to the initial void structure in response to macroscopic loading. The model predicts that regions of the highest stress concentration, in terms of σ_{33}, σ_{Hyd}, and σ_{TriAx} as shown in Fig. 5.9, are created around the large-seeded voids. An analysis of the µ-CT reconstruction at State 6 (3.4% macroscopic strain) reveals that the locations of void coalescence match with those predicted by the simulation, as shown in Fig 5.10(a,b). Regions between C1-C4 around the seeded void on the left of Fig 5.10(a,b) and between sites C5-C8 around the seeded void on the right form almost contiguous regions of coalescence and crack formation in the manner determined by the model.

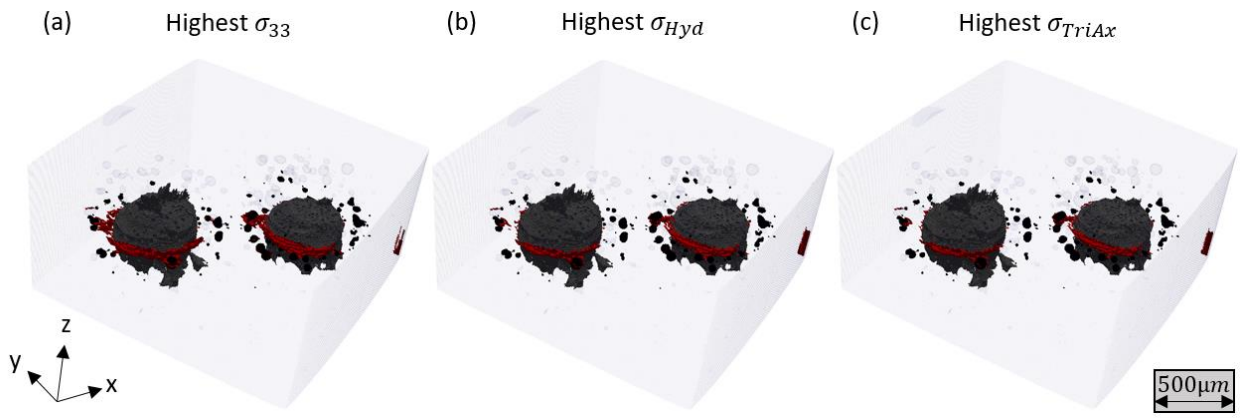

Figure 5.9 Sites of stress concentration after a macroscopic strain of 3.08% was applied through a linear elastic-plastic FEM simulation. (a) Metric: stress in the loading direction: µ (1270 MPa) + 2σ (248 MPa) > 1765 MPa; (b) Metric: hydrostatic stress: µ (423 MPa) + 3σ (179 MPa) > 960 MPa; (c) Metric: stress triaxiality: µ (0.3152) + 2.5σ (0.1721) > 0.7454. All three metrics suggest similar locations of high stress concentration, regions above the threshold have been highlighted in red.

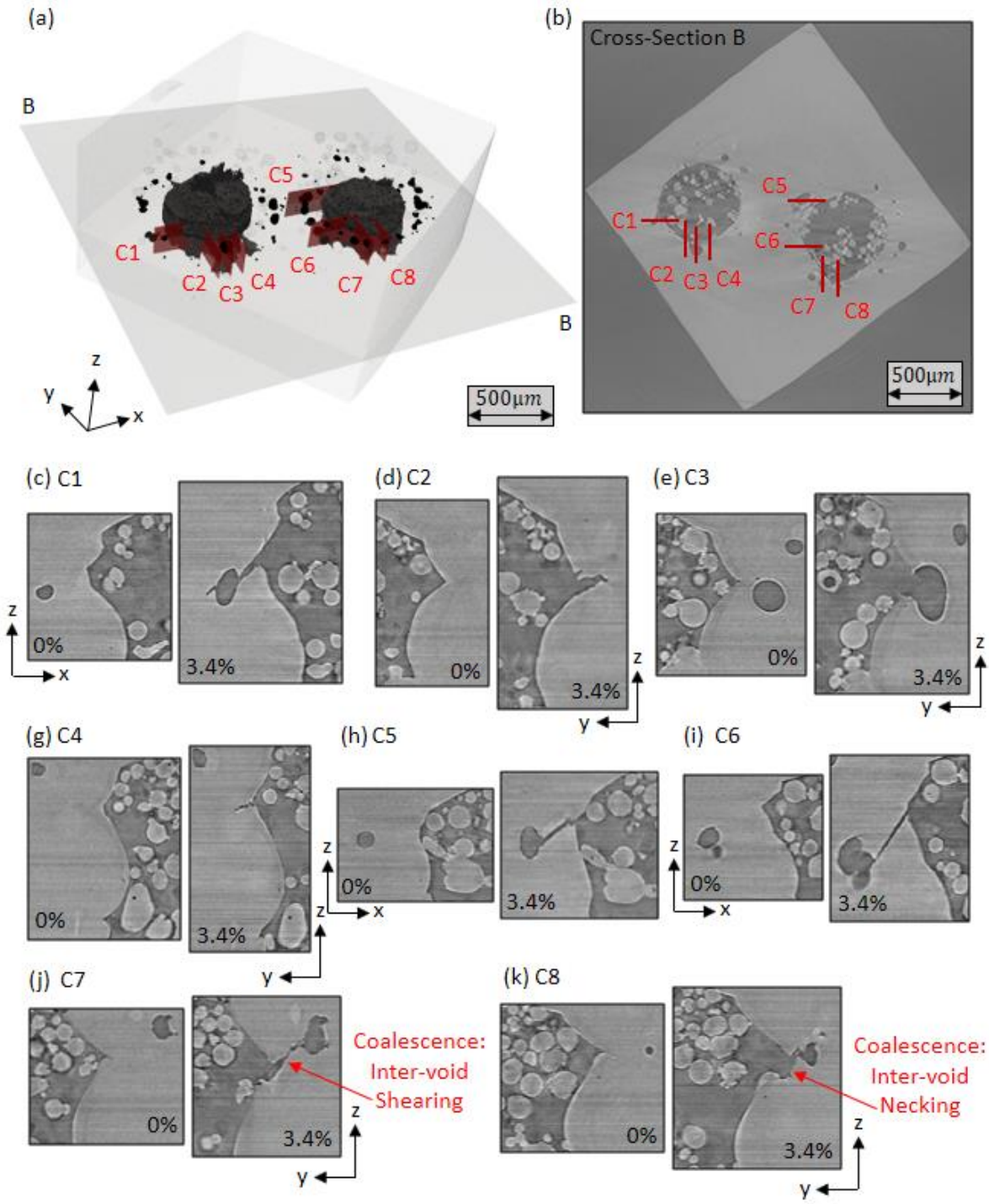

Figure 5.10 Sites of coalescence captured via μ-CT (a) 3D view of voids inside the region of interest; Cross-section B (as defined in Fig. 1) in dark grey marks the approximate slice of coalescence events around the seeded voids; specific planes, marked in red, have been extracted to show coalescence events. (b) Cross-section B and the coalescence sites, as marked in (a), at the final state of 3.4% macroscopic strain. (c-k) Coalescence sites around the seeded void between the initial (left) and final (right) states respectively. The path of coalescence suggests different modes of coalescence as marked in (j) and (k).

Carroll et al. [163] and Battaile et al. [164] have shown that the stress concentration due to voids becomes dominant when the size of voids is of the order or larger than that of the grains. Their studies were carried out with a single void/hole with respect to the microstructure. In this paper, several voids over a range of sizes were studied in proximity to their neighbors, as would exist in real AM materials. The simulations show, for this void distribution, the largest stress concentrators, which are expected to dominate the response of the material, occur at the locations between the natural and large-seeded voids. The physical attributes that should be considered at this scale of analysis, include statistics on the distribution of sizes and shapes, especially sharp features that result in stress concentrations. Analytical solutions attempt to incorporate shape effects through empirical constants like those adopted in [190], which is captured via a finite element implementation that incorporates a full-field method to account for these distributions. Moreover, the proximity of the voids to neighboring voids is particularly important, due to interaction effects.

The μ-CT reconstructions, shown in Fig 5.10(j,k), reveal that multiple modes of void coalescence may be active in the material. In this regard, the plot of stress triaxiality (Fig. 5.9(c)) is of particular interest because classically, stress triaxiality is used to differentiate mechanisms of void coalescence [162]. The simulation predicts high triaxiality at all sites of void coalescence, which suggests only one mechanism is active at each of the coalescence sites - inter-void necking, due to a homogenized description of the material with an isotropic yielding model in these simulations. The purpose of the present simulation was to capture the effect of the geometrical stress concentrators in the region of interest through a simple finite element implementation to assess its advantages and disadvantages. The homogenized material model is able to accurately determine the sites of void coalescence, but does not capture the correct coalescence mechanism at each of these sites. These models would be deemed as phenomenological and not necessarily physics-based. Further, the mechanisms proceed via different means, resulting in a deviation in the total strain to failure. Hence, by not capturing the appropriate mechanism in the model, there is uncertainty in the prediction of the strain to failure. The effect of the grain structure needs to be explored at this point to identify its relevance for ductile failure in this material.

The evolution of the micromechanical state measured at the grain scale was hypothesized, at the beginning of the paper, to capture the necessary and sufficient conditions to understand the

regime of ductile failure. To mediate a grain scale analysis, small volumes from the tessellation were extracted around known coalescence sites as shown in Fig. 5.11.

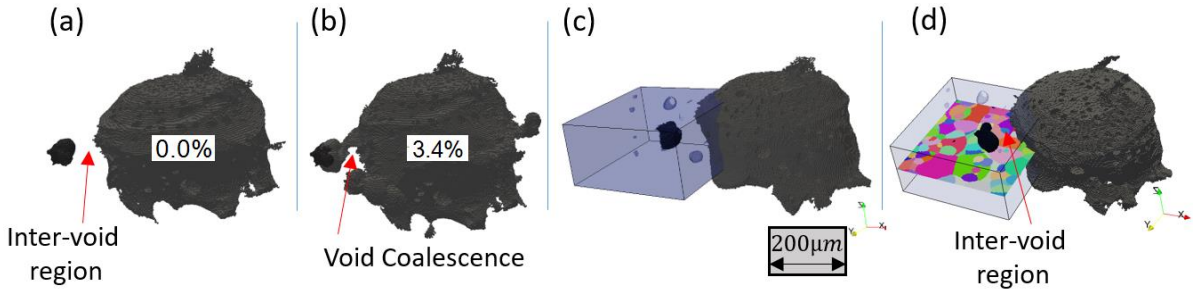

Figure 5.11 Extraction of the grain structure (~70 grains) surrounding the coalescence site marked in Fig.1: (a) the initial state before coalescence; (b) at 3.4% strain, after coalescence; (c) region extracted around coalescence site; and (d) grain structure in the region of interest.

For this critical region, a direct comparison of the distribution of the stress triaxiality between the experiment and simulation identifies the potential limitations of the simulation approach, as shown in Fig. 5.12. The heterogeneity in stress triaxiality in this small region is not captured by the simulation. It is important to capture the distribution of stress triaxiality states, particularly the low and negative stress triaxiality values, because they correspond to a different mechanism of void coalescence, i.e. through inter-void shearing [191–193]. In this study, we find that the grains at specific locations of coalescence show low (<1/3) to negative stress triaxiality (Fig. 5.13(b,f,j,n)), thus mediating a shear dominated coalescence event. This mechanism has received less attention in literature, and is not captured by widely-used, homogenized models, such as in [157]. The other active mechanism is inter-void necking, which is mediated by high triaxiality, as shown in Fig. 5.14(b,f). The simulations predicted high triaxiality, and as a consequence inter-void necking, at all experimentally observed coalescence sites, albeit as shown in Fig. 5.13, several of these sites exhibited shear dominated coalescence. Noell et al. [194] conducted detailed fractography after ductile failure and suggested as many as seven different mechanisms can be operative, in a sequential progression. In this study we show, similarly, that multiple mechanisms of void coalescence are active simultaneously around the seeded voids. The activation of a mechanism is dependent on the response of a very localized region between the two voids, which has been captured explicitly through the characterization of grains in this study. While the dominant stress concentrations within this sample were present near the large-seeded voids, the nuanced

micromechanical information necessary to understand the mechanisms driving ductile failure were only identified via the grain level response provided by far-field HEDM. And with the proper understanding of the physics-based mechanisms, predictive models can be generated for ductile failure.

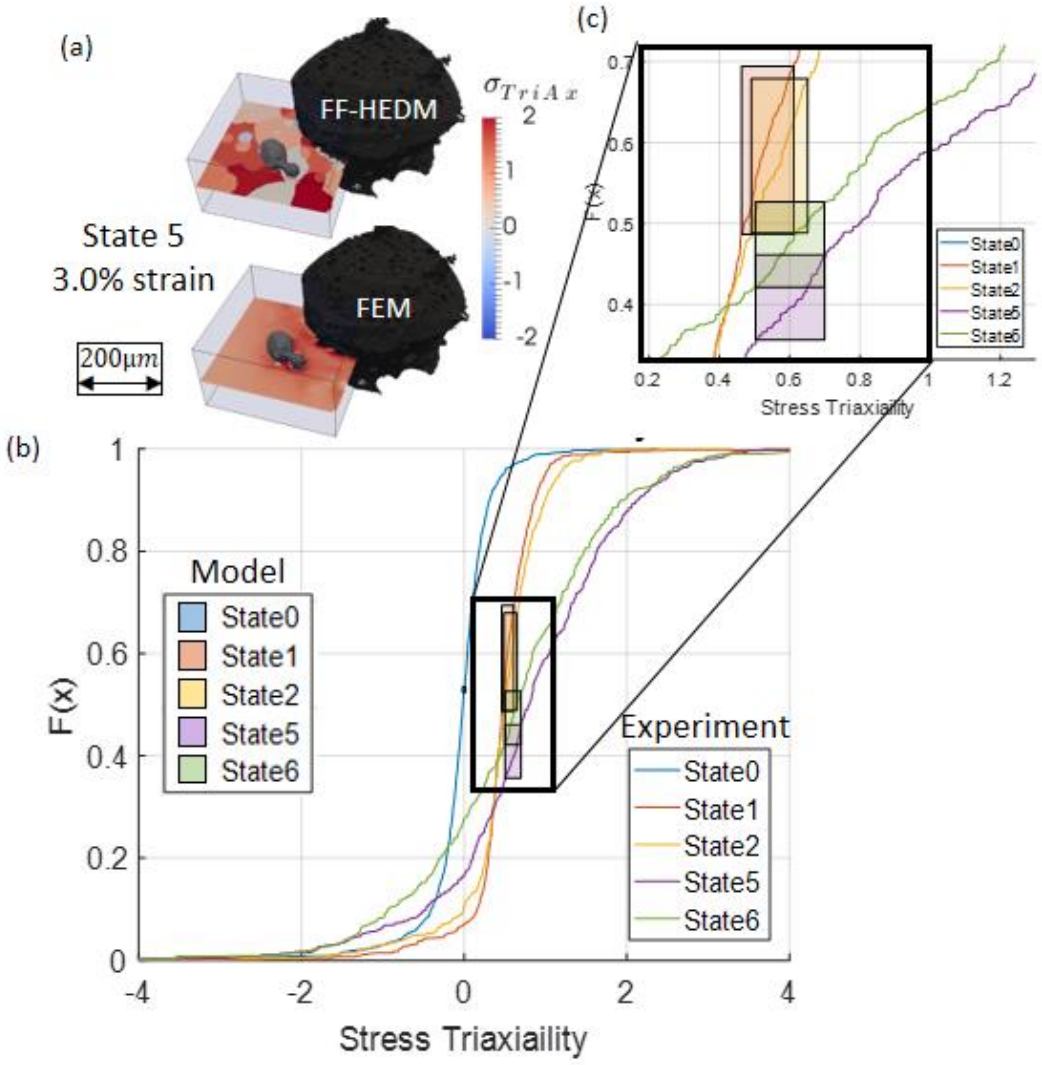

Figure 5.12 (a) Stress triaxiality in the region extracted around the void coalescence site. (b) Comparison between the results from far-field HEDM and FEM elastic-plastic simulation of the homogenized continuum. The far-field HEDM results are plotted with solid lines. The FEM results are plotted through rectangles, where the width represents the range between the 25th and 75th quantile of the stress triaxiality in the extracted region and the height represents the cumulative probability for the range with respect to the experimental curves. (c) The inset from (b), magnified to show the narrow distribution of the stress triaxiality from the isotropic FEM simulation.

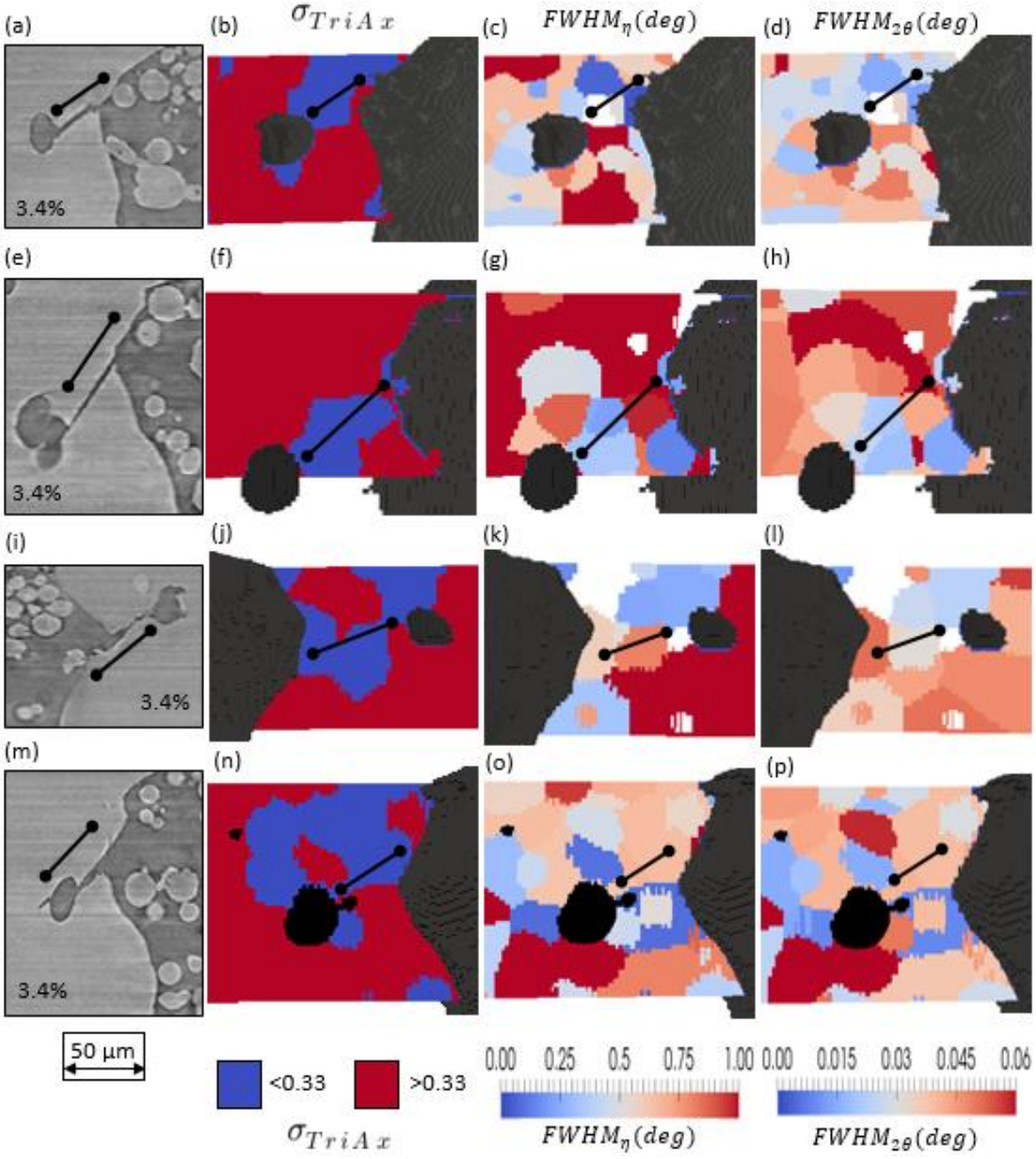

Figure 5.13 Void coalescence through inter-void shearing around (a) site C5, (e) site C6, (i) site C7, and (m) site C1, because of low to negative stress triaxiality marked by blue color in (b,f,j,n). Black line marks the path of coalescence as observed via µ-CT. No trend is found in the FWHM measures along η (c,g,k,o) and 2θ (d,h,l,p).

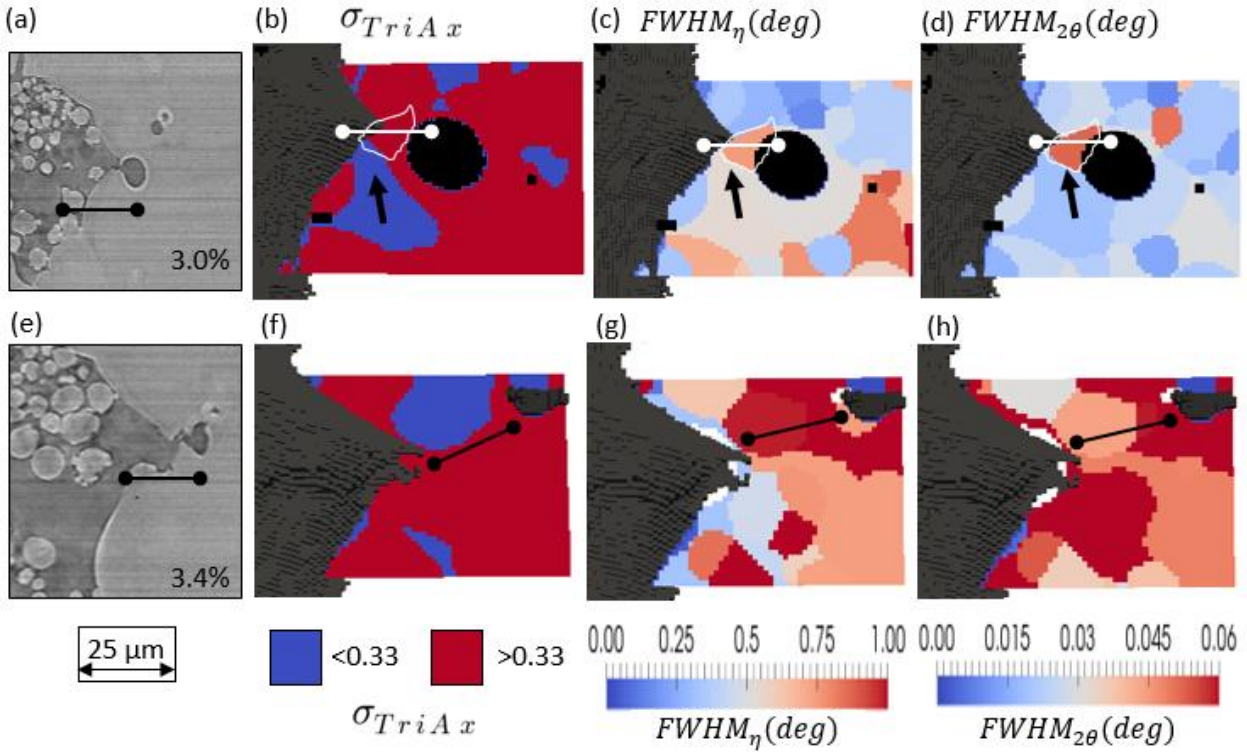

Figure 5.14 Void coalescence through inter-void necking at (a) site C3 and (e) site C8 is associated with high stress triaxiality, marked by the red color in (b,f) and concentration of the FWHM along η (c,g) and 2θ (d,h). The white/black lines mark the path of coalescence. In (b,c,d), a single grain is outlined by a white boundary, in the spacing between voids, that accommodates the plasticity and strain heterogeneity.

High triaxiality has been purported as a sufficient criterion for inter-void necking, although this may be too broad of classification, due to the following (i) many regions within the specimen display high triaxiality that do not lead to void coalescence and (ii) high triaxiality is a reported condition for additional mechanisms, such as void nucleation. For this reason, additional criteria, along with high triaxiality, are necessary to sufficiently describe inter-void necking, which are elucidated via reciprocal space mapping. High-energy X-ray diffraction techniques have the ability to provide data that can facilitate this distinction because of their sensitivity to the underlying crystal lattice within the grains. Although, before we accomplish this, there is a need to interpret the diffraction-based measures in terms of classical understanding of plasticity and strain heterogeneity. In this study, we show one such interpretation (please see schematic in Fig. 5.3) of the FWHM measures, obtained from analysis of the diffraction spots that are indexed to a

grain. The grains between voids accommodate necking through plasticity, which results in lattice curvature, and intergranular strain/stress heterogeneity. In Fig. 5.14, two regions of inter-void coalescence are shown, along with the values of the triaxiality and FWHM measures (along η and 2θ) in the surrounding grains. The grains that result in inter-void necking display high values of both triaxiality and FHWM measures. As can be seen in Fig. 5.7(d), there are many grains that exhibit a high value of stress triaxiality, which do not result in inter-void necking. Thus, high FHWM metrics, indicative of plasticity and strain heterogeneity, along with high values of triaxiality form a necessary and sufficient criterion for inter-void necking. These reciprocal space mapping approaches represent grain average values of the FWHM metrics, thus homogenizes spatial information near the pore, over the length-scale of the entire grain. For higher fidelity measurements, advanced X-ray techniques can be used, such as a point focused beam with a very far-field detector [176] to maximize the spatial and reciprocal space resolution near a pore or through analogous techniques like dark field X-ray microscopy [149].

Only a very small number of ductile failure studies have reported measurements at the microscale, particularly the grain scale [169,170]; macroscale quantities and surface measurements are still much more commonly reported for ductile failure. In this paper, we have shown that there are advantages to exploring ductile failure at the grain-level scale, which offers a departure from homogeneous descriptors. Further, grain level attributes capture all the necessary and sufficient information to predict the location and the mechanism of ductile failure. Multiple mechanisms are simultaneously operative in the bulk of the material, due to stress concentrating geometries over a range of sizes, while the grain level micromechanical attributes offer the necessary information to isolate and differentiate the individual mechanisms. As concluded by one of the results of the Sandia Fracture challenge [33], grain-level orientation dependence and localized deformation, among other factors, is essential for accurate predictions of ductile failure. Models, which work at the grain scale and are calibrated to experimental information like that provided in this paper, hold great promise for high fidelity predictive capabilities in the regime of ductile failure.

5.7 Summary and Conclusion

High-energy X-ray characterization experiments have been carried out to mediate a multi-scale analysis of ductile failure through void growth and coalescence in an additively manufactured Ni-based superalloy. The size and shape of each void along with their positions, with respect to the

surrounding voids in the region of interest, have been determined via μ-CT. The growth and coalescence between voids have been captured at several locations and the path of coalescence has been found to be indicative of the mechanism of coalescence prior to ductile failure.

A specimen scale analysis of void growth, through the Rice and Tracey model implementation, has shown good correspondence with the aggregate geometric changes in porosity but is not representative of the evolution of individual voids. Local coalescence events are not explicitly captured through the Rice and Tracey model, which results in deviation from experimental observations. Further, a linear elastic-plastic finite element simulation has been instantiated with the exact size, shape, and location of all the voids in the region of interest, which allows for an accurate description of the stress concentrations due to the interaction between voids. The finite element simulation determines the precise sites of experimentally-observed void coalescence, however, the exact mechanisms of coalescence are not ascertained with a homogenized material model.

The grain structure surrounding the voids has been characterized through far-field HEDM to determine the position, orientation, and lattice strains in each grain of the region of interest, and consolidated with the μ-CT information of the coalescence sites. The heterogeneity created in the material, due to the response of the grain structure to macroscopic loading, creates large variations in the micromechanical states, which are not captured by the homogenized material model. Two mechanisms of ductile failure were observed: (i) inter-void shearing, which corresponds to grains exhibiting low stress triaxiality and (ii) inter-void necking, which corresponds to grains exhibiting high stress triaxiality. Albeit, many grains in the region of interest display high stress triaxiality values, which indicates that high stress triaxiality is not a sufficient criterion for inter-void necking. High levels of plasticity and stress heterogeneity within the lattice of the grain(s) between voids provides the additional information, along with high stress triaxiality, to provide the necessary and sufficient criteria for inter-void necking based failure. In summary, a grain scale description of the micromechanical state has been proven to accurately capture both the sites and the mechanisms of void coalescence at the onset of ductile failure, and thus provides an ideal physical basis to understand the fundamentals of ductile failure; instilling trust in the predictive capabilities of models that incorporate the response of the grain structure for studying fracture.

6. CONCLUSIONS AND FUTURE WORK

6.1 Conclusions

The overarching goal of this thesis was to supplement the understanding of various defect mediated damage mechanisms by leveraging the advent of advanced X-ray characterization techniques to elucidate the structure and micromechanical state at the grain scale in the vicinity of critical locations of material failure. Towards the fulfillment of this objective, samples were designed to have (i) a seeded inclusion, (ii) a naturally initiated crack, and (iii) voids in the bulk of polycrystalline Ni-superalloy specimens. Computed micro-tomography (μ-CT) was undertaken to characterize the morphology and positions of the defect structure at the initial state and track it during successive loading. High energy diffraction microscopy (HEDM) was employed to elucidate the region of interest surrounding the defects by revealing the underlying heterogeneous (i) grain structure (orientation maps), (ii) the stress state in each discovered grain, and (iii) the intragranular lattice curvature and lattice strain heterogeneity which accommodates the deformation within the grain. Simulation tools were employed to prove the contribution of factors that were identified to be essential to the mechanism of failure for each of these defects. The main factors behind each defect mediated mechanism is as follows:

6.1.1 Case Study 1: Inclusion driven failure

Absorption contrast μ-CT was used to determine when, and more importantly where, the crack initiated. FF-HEDM was performed to map the microstructure surrounding the inclusion, including the orientations and 3-D intergranular strain states of each grain. The cyclic loading generated heterogeneity in stress distribution and a gradient was found to exist in the magnitude of strain across the crack initiation site which was revealed to create the necessary conditions for a crack to initiate. The main factors that resulted in this gradient have been corroborated through proof of principle 3-D EVP-FFT simulations, they are as follows:

- Debonding at the inclusion-matrix interface;
- Residual state induced by the inclusion in the surrounding matrix;
- Geometrical contribution of a large rigid inclusion at an inclination to the loading axis;

6.1.2 Case Study 2: Short fatigue crack driven failure

The tortuosity and progression of the short fatigue crack was determined through μ-CT in various modes. The heterogeneity in the evolving mechanical stress fields in conjunction with the deformation state within the grains, around the SFC, was determined through diffraction data from NF-HEDM, FF-HEDM, and reciprocal space mapping. The interaction of the SFC with ~50 adjacent grains has been studied in detail in regard to these micromechanical fields to discover that:

- The crack plane, during intragranular crack growth, conformed to the slip planes of the active slip system determined by the τ_{MRSS}. The normal stress relative to the most active slip plane served as an opening stress during intragranular crack propagation.
- The crack growth direction, during intragranular crack growth, conformed to the slip directions of the active slip system determined by τ_{MRSS};
- The crack growth rate shows a correlation with the τ_{MRSS} on the conforming slip system within the grain;
- The crack growth direction, at the transition to a new grain, can be determined through the severity of the plasticity in the grains ahead of the crack front in terms of the FWHM measures for intragranular misorientation or lattice strain gradient within the grain.

Intergranular SFC growth, highly unlikely at room temperature and in ambient lab environments, was also observed along low energy grain boundaries; these grains were easily identified due to large misalignment in their stress state as determined through their stress coaxiality.

6.1.3 Case Study 3: Void growth and coalescence driven failure

The size and shape of each void along with their positions, with respect to the surrounding voids in the region of interest, have been determined via μ-CT. The grain structure surrounding the voids has been characterized through far-field HEDM to determine the position, orientation, and lattice strains in each grain of the region of interest, and consolidated with the μ-CT information of the coalescence sites. The growth and coalescence between voids have been captured at several locations and the path of coalescence has been found to be indicative of the

mechanism of coalescence prior to ductile failure. To capture both, the location and the mechanism of failure, the main factors were found to be:

- Inter-void shearing, which corresponds to grains exhibiting low stress triaxiality
- Inter-void necking, which corresponds to grains exhibiting high stress triaxiality.
- High levels of plasticity and stress heterogeneity within the lattice of the grain(s) between voids provides the additional information, along with high stress triaxiality, to provide the necessary and sufficient criteria for inter-void necking based failure.

In summary, from all three case studies, we find that a grain scale description of the micromechanical state can be unambiguously determined through experiments to examine the heterogeneity around defects in the material. This description has enabled us to identify and isolate the nature of factors essential to activate specific mechanisms at the onset failure. The grain scale thus provides an ideal departure from a homogenized description of the material and a physical basis that is necessary and sufficient to understand the fundamentals of defect mediated damage and failure. The datasets, that have been generated, can be used to instantiate and calibrate crystal plasticity models, at the grain level, for higher fidelity.

6.2 Future work and Recommendations

The case studies undertaken in this thesis are the first of their kind in their setup which combines in-situ mechanical loading and X-ray characterization techniques to elucidate the structural and micromechanical state locally around purposefully seeded defects in bulk polycrystalline metallic alloys. One of the main issues with leading such studies has been with designing experiments that are robust enough to succeed on their first try during precious and limited beam-time earned at a synchrotron source. This is partly due to a severe limitation during beam-time with long collection times for HEDM scans and real-time reconstructions to guide and inform the remainder of the experiment. There is fine balance that needs to be struck with the size of the region that needs to be scanned and the number of states that need to be interrogated with the expectations of capturing something noteworthy because of very limited feedback during the experiment.

In order to ensure success, in all three case studies, we incorporated defects which were larger in scale than the inherent scale of microstructural elements and would be found in only a few remote scenarios in production. This enabled us to predict regions of interest where activity would be localized and during the experiments we could scope out these regions quickly via μ-CT. Delineating such regions allowed precision scans with HEDM techniques that ensured enough detail was captured while saving time for more successive load states to be interrogated. On the flipside, there was a well-founded fear for the large scale of the defects to render the microscale information futile and reduce the problem to a simple geometric solution. We analyzed the data in detail to find relevance of the grain scale and demonstrated that it serves as a natural length scale that offers the perfect departure from a homogenized description of the material and an essential physical basis to understand various modes of failure.

One of the main comments is centered around creating samples with more representative defect structures and dividing the experiment into different parts with time in between to observe trends in the material and employ the predictive capabilities of models. This will serve the two-fold objective of creating well calibrated models and checking their fidelity through blind predictions of the outcome of the experiment. The predictions, irrespective of their veracity, will in-turn help direct the successive leg of the experiment.

Experimental techniques are available at both a length scale lower and higher than the grain scale. For instance:

- EBSD and DIC offer high resolution measurements of the structure and strain state at the surface analogous to μ-CT and HEDM in the bulk. One of the current undertakings in our lab, led by John Rotella, is to compare the two sets of techniques in order to ascertain the relevance of a 3D vs 2D surface measure of the micromechanical state.
- X-rays optics before illuminating the sample can be focused to create point focused beams for higher spatial resolution. Similarly, the diffracted beam can be magnified through either the optics (for ex. Dark field microscopy [149], coherent diffraction imaging [195]) or longer hutches for larger sample to detector distances (very far-field HEDM or high resolution reciprocal space mapping [196]) to extend the orientation and strain resolution of the measurements. However, the applicability of these techniques is concomitant to identifying even smaller regions of interest and onerous task of extracting miniature samples around these regions. One such undertaking is being led by Sven Gustafson to

better understand the phenomenon of twin interaction in Ni-superalloys that create a heterogeneous stress state.

- The choice of the experimental technique is based on the scale of the problem and in many cases lower resolution techniques like Energy Dispersive X-ray diffraction [197] or Neutron diffraction [198] techniques can offer complementary information at a scale that is sufficient for the mechanism. One such undertaking has been published by Ritwik Bandyopadhyay [197] has been used to study residual strain analysis in linear friction welds of similar and dissimilar titanium alloys.

One of the main outputs of each of these case studies is a rich multi-modal dataset that can be used to inform models at the grain scale.

- The grain level information can be used to instantiate accurate sample geometry and grain structures while initializing them with type-2 residual stresses in the model [187]
- The data can be used to calibrate the model to local grain scale response
- The outcome of the experiment can be used to corroborate the predictions of the models to ensure high fidelity and instill faith in the model
- Finally, a sensitivity study and uncertainty quantification can prove to be a powerful tool with the help of actual data to assess the contribution of the numerous variables and fine tune the models themselves.

These modeling efforts are a continuous endeavor in the $ACME^2$ lab. The author has accepted a post-doctoral research position at the Air Force Research lab where he hopes to continue this line of research.

REFERENCES

[1] R.C. Reed, The Superalloys: Fundamentals and Applications, Cambridge University Press, 2006. doi:10.1017/CBO9780511541285.

[2] M.J. Caton, S.K. Jha, A.H. Rosenberger, J.M. Larsen, Divergence of mechanisms and the effect on the fatigue life variability of Rene'88DT, Superalloys 2004. (2004) 305–312.

[3] E.S. Huron, P.G. Roth, The influence of inclusions on low cycle fatigue life in a P/M nickel-base disk superalloy, Superalloys 1996. (1996) 359–368.

[4] F. Alexandre, S. Deyber, A. Pineau, Modelling the optimum grain size on the low cycle fatigue life of a Ni based superalloy in the presence of two possible crack initiation sites, Scr. Mater. 50 (2004) 25–30. doi:10.1016/j.scriptamat.2003.09.043.

[5] J.M. Hyzak, I.M. Bernstein, The Effect of Defects on the Fatigue Crack Initiation Process in Two P / M Superalloys : Part I . Fatigue Origins, Metall. Trans. A. 13 (1982) 33–43.

[6] P.S. Karamched, A.J. Wilkinson, High resolution electron back-scatter diffraction analysis of thermally and mechanically induced strains near carbide inclusions in a superalloy, Acta Mater. 59 (2011) 263–272. doi:10.1016/j.actamat.2010.09.030.

[7] Y. MURAKAMI, M. ENDO, Effects of defects, inclusions and inhomogeneities on fatigue strength, Int. J. Fatigue. 16 (1994) 163–182. doi:10.1016/0142-1123(94)90001-9.

[8] A.F. (Alten F.. Grandt, Fundamentals of structural integrity : damage tolerant design and nondestructive evaluation, J. Wiley, 2003.

[9] M.F. Ashby, L.M. Brown, On diffraction contrast from inclusions, Philos. Mag. 8 (1963) 1649–1676. doi:10.1080/14786436308207329.

[10] J. Jiang, J. Yang, T. Zhang, J. Zou, Y. Wang, F.P.E. Dunne, T.B. Britton, Microstructurally sensitive crack nucleation around inclusions in powder metallurgy nickel-based superalloys, Acta Mater. 117 (2016) 333–344. doi:10.1016/j.actamat.2016.07.023.

[11] T. Zhang, J. Jiang, B.A. Shollock, T. Ben Britton, F.P.E. Dunne, Slip localization and fatigue crack nucleation near a non-metallic inclusion in polycrystalline nickel-based superalloy, Mater. Sci. Eng. A. 641 (2015) 328–339. doi:10.1016/j.msea.2015.06.070.

[12] J. Jiang, T.B. Britton, A.J. Wilkinson, Measurement of geometrically necessary dislocation density with high resolution electron backscatter diffraction: Effects of detector binning and step size, Ultramicroscopy. 125 (2013) 1–9. doi:10.1016/j.ultramic.2012.11.003.

[13] S. Suresh, Fatigue of Materials, 2nd ed., Cambridge University Press, 1998. doi:10.1017/CBO9780511806575.

[14] T.P. Gabb, J. Gayda, J. Telesman, A. Garg, The effects of heat treatment and microstructure variations on disk superalloy properties at high temperature, Superalloys 2008. (2008) 121–130. http://www.tms.org/superalloys/10.7449/2008/Superalloys_2008_121_130.pdf (accessed April 5, 2017).

[15] S. Pearson, Initiation of fatigue cracks in commercial aluminium alloys and the subsequent propagation of very short cracks, Eng. Fract. Mech. 7 (1975). doi:10.1016/0013-7944(75)90004-1.

[16] S. Suresh, R.O. Ritchie, Propagation of short fatigue cracks, Int. Met. Rev. 29 (1984) 445–475. doi:10.1179/imtr.1984.29.1.445.

[17] K.J. Miller, Short Fatigue Cracks, in: Adv. Fatigue Sci. Technol., Springer Netherlands, Dordrecht, 1989: pp. 3–22. doi:10.1007/978-94-009-2277-8_1.

[18] R.O. Ritchie, J. Lankford, Small fatigue cracks: A statement of the problem and potential solutions, Mater. Sci. Eng. 84 (1986) 11–16. doi:10.1016/0025-5416(86)90217-X.

[19] K.S. Ravichandran, R.O. Ritchie, Y. Murakami, Small fatigue cracks : mechanics, mechanisms, and applications : proceedings of the Third Engineering Foundation International Conference, Turtle Bay Hilton, Oahu, Hawaii, December 6-11, 1998, Elsevier, 1999.

[20] J. Schijve, Fatigue of Structures andMaterials, Springer. (2009).

[21] D. Davidson, K. Chan, R. McClung, S. Hudak, 4.05 – Small Fatigue Cracks, in: Compr. Struct. Integr., 2003: pp. 129–164. doi:10.1016/B0-08-043749-4/04073-8.

[22] A.J. McEvily, R.G. Boettner, On fatigue crack propagation in F.C.C. metals, Acta Metall. 11 (1963) 725–743. doi:10.1016/0001-6160(63)90010-5.

[23] K.J. Miller, Materials science perspective of metal fatigue resistance, Mater. Sci. Technol. 9 (1993) 453–462. doi:10.1179/mst.1993.9.6.453.

[24] G.R. Yoder, L.A. Cooley, T.W. Crooker, Quantitative analysis of microstructural effects on fatigue crack growth in widmanstätten Ti-6A1-4V and Ti-8Al-1Mo-1V, Eng. Fract. Mech. 11 (1979) 805–816. doi:10.1016/0013-7944(79)90138-3.

[25] A.K. Zurek, M.R. James, W.L. Morris, The Effect of Grain Size on Fatigue Growth of Short Cracks, Metall. Trans. A. 14 (1983) 1697–1705. doi:10.1007/BF02654397.

[26] A. Navarro, E.R. Rios, A microstructurally-short fatigue crack growth equation, Fatigue Fract. Eng. Mater. Struct. 11 (1988) 383–396. doi:10.1111/j.1460-2695.1988.tb01391.x.

[27] T. Zhai, A.J. Wilkinson, J.W. Martin, A crystallographic mechanism for fatigue crack propagation through grain boundaries, Acta Mater. 48 (2000) 4917–4927. doi:10.1016/S1359-6454(00)00214-7.

[28] K. Tanaka, Y. Akiniwa, Y. Nakai, R.P. Wei, Modelling of small fatigue crack growth interacting with grain boundary, Eng. Fract. Mech. 24 (1986) 803–819. doi:10.1016/0013-7944(86)90266-3.

[29] Y. Guilhem, S. Basseville, F. Curtit, J.-M. Stephan, G. Cailletaud, Y. Guilhem, S. Basseville, F. Curtit, J. Stéphan, G. Cailletaud, In-vestigation of the effect of grain clusters on fatigue crack initiation in polycrystals. International Jour-nal of Fatigue, 32 (2010) 1748–1763. doi:10.1016/j.ijfatigue.2010.04.003.

[30] M.D. Sangid, H.J. Maier, H. Sehitoglu, The role of grain boundaries on fatigue crack initiation – An energy approach, Int. J. Plast. 27 (2011) 801–821. doi:10.1016/J.IJPLAS.2010.09.009.

[31] H.E. Helmer, C. Körner, R.F. Singer, Additive manufacturing of nickel-based superalloy Inconel 718 by selective electron beam melting: Processing window and microstructure, (2019). doi:10.1557/jmr.2014.192.

[32] V.A. Popovich, E.V. Borisov, A.A. Popovich, V.S. Sufiiarov, D.V. Masaylo, L. Alzina, Functionally graded Inconel 718 processed by additive manufacturing: Crystallographic texture, anisotropy of microstructure and mechanical properties, Mater. Des. 114 (2017) 441–449. doi:10.1016/J.MATDES.2016.10.075.

[33] B.L. Boyce, S.L.B. Kramer, T.R. Bosiljevac, E. Corona, J.A. Moore, K. Elkhodary, C.H.M. Simha, B.W. Williams, A.R. Cerrone, A. Nonn, J.D. Hochhalter, G.F. Bomarito, J.E. Warner, B.J. Carter, D.H. Warner, A.R. Ingraffea, T. Zhang, X. Fang, J. Lua, V. Chiaruttini, M. Mazière, S. Feld-Payet, V.A. Yastrebov, J. Besson, J.-L. Chaboche, J. Lian, Y. Di, B. Wu, D. Novokshanov, N. Vajragupta, P. Kucharczyk, V. Brinnel, B. Döbereiner, S. Münstermann, M.K. Neilsen, K. Dion, K.N. Karlson, J.W. Foulk, A.A. Brown, M.G. Veilleux, J.L. Bignell, S.E. Sanborn, C.A. Jones, P.D. Mattie, K. Pack, T. Wierzbicki, S.-W. Chi, S.-P. Lin, A. Mahdavi, J. Predan, J. Zadravec, A.J. Gross, K. Ravi-Chandar, L. Xue, The second Sandia Fracture Challenge: predictions of ductile failure under quasi-static and moderate-rate dynamic loading, Int. J. Fract. 198 (2016) 5–100. doi:10.1007/s10704-016-0089-7.

[34] S.D. Shastri, J. Almer, C. Ribbing, B. Cederström, High-energy X-ray optics with silicon saw-tooth refractive lenses, J. Synchrotron Radiat. 14 (2007) 204–211. doi:10.1107/S0909049507003962.

[35] U. Lienert, S.F. Li, C.M. Hefferan, J. Lind, R.M. Suter, J. V. Bernier, N.R. Barton, M.C. Brandes, M.J. Mills, M.P. Miller, B. Jakobsen, W. Pantleon, High-energy diffraction microscopy at the advanced photon source, JOM. 63 (2011) 70–77. doi:10.1007/s11837-011-0116-0.

[36] S.R. Stock, Recent advances in X-ray microtomography applied to materials Recent advances in X-ray microtomography applied to materials, Int. Mater. Rev. 53 (2008) 129–181. doi:10.1179/174328008X277803.

[37] S.R. Stock, X-ray microtomography of materials X-ray microtomography of materials, Int. Mater. Rev. 44 (1999) 141–164. doi:10.1179/095066099101528261.

[38] Y. Wang, F. De Carlo, I. Foster, J. Insley, C. Kesselman, P. Lane, G. von Laszewski, D.C. Mancini, I. McNulty, M.-H. Su, B. Tieman, Quasi-real-time x-ray microtomography system at the Advanced Photon Source</title>, in: U. Bonse (Ed.), SPIE Proc. Dev. X-Ray Tomogr. II, International Society for Optics and Photonics, 1999: pp. 318–327. doi:10.1117/12.363735.

[39] A. Khounsary, P. Kenesei, J. Collins, G. Navrotski, J. Nudell, High Energy X-ray Micro-tomography for the characterization of thermally fatigued GlidCop specimen, J. Phys. Conf. Ser. 425 (2013) 212015. doi:10.1088/1742-6596/425/21/212015.

[40] B.A. Dowd, G.H. Campbell, R.B. Marr, V. V. Nagarkar, S. V. Tipnis, L. Axe, D.P. Siddons, Developments in synchrotron x-ray computed microtomography at the National Synchrotron Light Source, in: U. Bonse (Ed.), SPIE Proc. Dev. X-Ray Tomogr. II, International Society for Optics and Photonics, 1999: pp. 224–236. doi:10.1117/12.363725.

[41] J. Schindelin, C.T. Rueden, M.C. Hiner, K.W. Eliceiri, The ImageJ ecosystem: An open platform for biomedical image analysis, Mol. Reprod. Dev. 82 (2015) 518–529. doi:10.1002/mrd.22489.

[42] D. Jha, H.O. Sørensen, S. Dobberschütz, R. Feidenhans'l, S.L.S. Stipp, Adaptive center determination for effective suppression of ring artifacts in tomography images, Appl. Phys. Lett. 105 (2014) 143107. doi:10.1063/1.4897441.

[43] I. Arganda-Carreras, V. Kaynig, C. Rueden, K.W. Eliceiri, J. Schindelin, A. Cardona, H. Sebastian Seung, Trainable Weka Segmentation: a machine learning tool for microscopy pixel classification, Bioinformatics. 33 (2017) 2424–2426. doi:10.1093/bioinformatics/btx180.

[44] H.F. Poulsen, Three-dimensional X-ray diffraction microscopy : mapping polycrystals and their dynamics, Springer, 2004.

[45] H.F. Poulsen, An introduction to three-dimensional X-ray diffraction microscopy, J. Appl. Crystallogr. 45 (2012) 1084–1097. doi:10.1107/S0021889812039143.

[46] H.F. Poulsen, S.F. Nielsen, E.M. Lauridsen, S. Schmidt, R.M. Suter, U. Lienert, L. Margulies, T. Lorentzen, D.J. Jensen, Copyright, Three-Dimensional Maps of Grain Boundaries and the Stress State of Individual Grains in Polycrystals and Powders, J. Appl. Crystallogr. 34 (2001) 751–756. doi:10.1107/S0021889801014273.

[47] L. Margulies, T. Lorentzen, H.F. Poulsen, T. Leffers, Strain tensor development in a single grain in the bulk of a polycrystal under loading, Acta Mater. 50 (2002) 1771–1779. doi:10.1016/S1359-6454(02)00028-9.

[48] J. Oddershede, S. Schmidt, H.F. Poulsen, H.O. Srensen, J. Wright, W. Reimers, Determining grain resolved stresses in polycrystalline materials using three-dimensional X-ray diffraction, J. Appl. Crystallogr. 43 (2010) 539–549. doi:10.1107/S0021889810012963.

[49] J.H. Lee, C.C. Aydıner, J. Almer, J. Bernier, K.W. Chapman, P.J. Chupas, D. Haeffner, K. Kump, P.L. Lee, U. Lienert, A. Miceli, G. Vera, IUCr, Synchrotron applications of an amorphous silicon flat-panel detector, J. Synchrotron Radiat. 15 (2008) 477–488. doi:10.1107/S090904950801755X.

[50] J. V. Bernier, N.R. Barton, U. Lienert, M.P. Miller, Far-field high-energy diffraction microscopy: a tool for intergranular orientation and strain analysis, J. Strain Anal. Eng. Des. 46 (2011) 527–547. doi:10.1177/0309324711405761.

[51] H. Sharma, R.M. Huizenga, S.E. Offerman, A fast methodology to determine the characteristics of thousands of grains using three-dimensional X-ray diffraction. I. Overlapping diffraction peaks and parameters of the experimental setup, J. Appl. Crystallogr. 45 (2012) 693–704. doi:10.1107/S0021889812025563.

[52] H. Sharma, R.M. Huizenga, S.E. Offerman, A fast methodology to determine the characteristics of thousands of grains using three-dimensional X-ray diffraction. II. Volume, centre-of-mass position, crystallographic orientation and strain state of grains, J. Appl. Crystallogr. 45 (2012) 705–718. doi:10.1107/S0021889812025599.

[53] J.C. Schuren, M.P. Miller, Quantifying the uncertainty of synchrotron-based lattice strain measurements, J. Strain Anal. Eng. Des. 46 (2011) 663–681. doi:10.1177/0309324711411553.

[54] R.M. Suter, D. Hennessy, C. Xiao, U. Lienert, Forward modeling method for microstructure reconstruction using x-ray diffraction microscopy: Single-crystal verification, Rev. Sci. Instrum. 77 (2006) 123905. doi:10.1063/1.2400017.

[55] S.F. Li, R.M. Suter, IUCr, M.J. C., X. C., L. U., T. B., J.D. J., K. M., Adaptive reconstruction method for three-dimensional orientation imaging, J. Appl. Crystallogr. 46 (2013) 512–524. doi:10.1107/S0021889813005268.

[56] C.M. Hefferan, S.F. Li, J. Lind, U. Lienert, A.D. Rollett, P. Wynblatt, R.M. Suter, Statistics of High Purity Nickel Microstructure From High Energy X-ray Diffraction Microscopy, Comput. Mater. Contin. 14 (2009) 209–219.

[57] M. Obstalecki, S.L. Wong, P.R. Dawson, M.P. Miller, Quantitative analysis of crystal scale deformation heterogeneity during cyclic plasticity using high-energy X-ray diffraction and finite-element simulation, Acta Mater. 75 (2014) 259–272. doi:10.1016/j.actamat.2014.04.059.

[58] S.L. Wong, J.S. Park, M.P. Miller, P.R. Dawson, A framework for generating synthetic diffraction images from deforming polycrystals using crystal-based finite element formulations, Comput. Mater. Sci. 77 (2013). doi:10.1016/j.commatsci.2013.03.019.

[59] J. Oddershede, J.P. Wright, A. Beaudoin, G. Winther, Deformation-induced orientation spread in individual bulk grains of an interstitial-free steel, Acta Mater. 85 (2015) 301–313. doi:10.1016/j.actamat.2014.11.038.

[60] A.W. Mello, A. Nicolas, M.D. Sangid, Fatigue strain mapping via digital image correlation for Ni-based superalloys: The role of thermal activation on cube slip, Mater. Sci. Eng. A. 695 (2017) 332–341. doi:10.1016/J.MSEA.2017.04.002.

[61] B. Pan, K. Qian, H. Xie, A. Asundi, Two-dimensional digital image correlation for in-plane displacement and strain measurement: a review, Meas. Sci. Technol. 20 (2009) 062001. doi:10.1088/0957-0233/20/6/062001.

[62] M.A. Sutton, S.R. McNeill, J.D. Helm, Y.J. Chao, Advances in Two-Dimensional and Three-Dimensional Computer Vision, in: Photomechanics, Springer Berlin Heidelberg, Berlin, Heidelberg, 2000: pp. 323–372. doi:10.1007/3-540-48800-6_10.

[63] W.Z. Abuzaid, M.D. Sangid, J.D. Carroll, H. Sehitoglu, J. Lambros, Slip transfer and plastic strain accumulation across grain boundaries in Hastelloy X, J. Mech. Phys. Solids. 60 (2012) 1201–1220. doi:10.1016/j.jmps.2012.02.001.

[64] K. Chatterjee, A. Venkataraman, T. Garbaciak, J. Rotella, M.D. Sangid, A.J. Beaudoin, P. Kenesei, J.-S. Park, A.L. Pilchak, Study of grain-level deformation and residual stresses in Ti-7Al under combined bending and tension using high energy diffraction microscopy (HEDM), Int. J. Solids Struct. 94 (2016) 35–49. doi:10.1016/j.ijsolstr.2016.05.010.

[65] R.A. Lebensohn, A.K. Kanjarla, P. Eisenlohr, An elasto-viscoplastic formulation based on fast Fourier transforms for the prediction of micromechanical fields in polycrystalline materials, Int. J. Plast. 32 (2012) 59–69. doi:10.1016/j.ijplas.2011.12.005.

[66] A. Rovinelli, H. Proudhon, R.A. Lebensohn, M.D. Sangid, Assessing the reliability of fast Fourier transform-based crystal plasticity simulations of a polycrystalline material near a crack tip, Int. J. Solids Struct. (2019). doi:10.1016/J.IJSOLSTR.2019.02.024.

[67] D. Naragani, M.D. Sangid, P.A. Shade, J.C. Schuren, H. Sharma, J.-S. Park, P. Kenesei, J. V. Bernier, T.J. Turner, I. Parr, Investigation of fatigue crack initiation from a non-metallic inclusion via high energy x-ray diffraction microscopy, Acta Mater. 137 (2017) 71–84. doi:10.1016/j.actamat.2017.07.027.

[68] M.D. Uchic, M.A. Groeber, D.M. Dimiduk, J.P. Simmons, 3D microstructural characterization of nickel superalloys via serial-sectioning using a dual beam FIB-SEM, Scr. Mater. 55 (2006) 23–28. doi:10.1016/j.scriptamat.2006.02.039.

[69] M.P. Echlin, A. Mottura, C.J. Torbet, T.M. Pollock, A new TriBeam system for three-dimensional multimodal materials analysis, Rev. Sci. Instrum. 83 (2012) 023701. doi:10.1063/1.3680111.

[70] M. Uchic, M. Groeber, M. Shah, P. Callahan, A. Shiveley, M. Scott, M. Chapman, J. Spowart, An Automated Multi-Modal Serial Sectioning System for Characterization of Grain-Scale Microstructures in Engineering Materials, in: 1st Int. Conf. 3D Mater. Sci., John Wiley & Sons, Inc., Hoboken, NJ, USA, 2013: pp. 195–202. doi:10.1002/9781118686768.ch30.

[71] D. V Nelson, Effect of Residual Stress on Fatigue Crack Propagation, Residual Stress Eff. Fatigue. STP 776 (1982) 172–194.

[72] G.A. Webster, A.N. Ezeilo, Residual stress distributions and their influence on fatigue lifetimes, Int. J. Fatigue. 23 (2001) 375–383. doi:10.1016/S0142-1123(01)00133-5.

[73] K.P. McNelis, P.R. Dawson, M.P. Miller, A two-scale methodology for determining the residual stresses in polycrystalline solids using high energy X-ray diffraction data, J. Mech. Phys. Solids. 61 (2013) 428–449. doi:10.1016/j.jmps.2012.09.015.

[74] J.-S. Park, U. Lienert, P.R. Dawson, M.P. Miller, Quantifying Three-Dimensional Residual Stress Distributions Using Spatially-Resolved Diffraction Measurements and Finite Element Based Data Reduction, Exp. Mech. 53 (2013) 1491–1507. doi:10.1007/s11340-013-9771-0.

[75] T.J. Turner, P.A. Shade, J. V. Bernier, S.F. Li, J.C. Schuren, P. Kenesei, R.M. Suter, J. Almer, Crystal Plasticity Model Validation Using Combined High-Energy Diffraction Microscopy Data for a Ti-7Al Specimen, Metall. Mater. Trans. A. 48 (2017) 627–647. doi:10.1007/s11661-016-3868-x.

[76] I. Cernatescu, V. Venkatesh, J.L. Glanovsky, L.H. Landry, R.N. Green, M. Street, E. Hartford, Residual Stress Measurements Implementation for Model Validation as part of Foundational Engineering Problem Program on ICME of Bulk Residual Stress in Ni Rotors, AIAA J. Proceedings, SciTech Conf. Proc. 0387. (2015) 1–9. doi:10.2514/6.2015-0387.

[77] W.D. Musinski, D.L. McDowell, On the eigenstrain application of shot-peened residual stresses within a crystal plasticity framework: Application to Ni-base superalloy specimens, Int. J. Mech. Sci. 100 (2015) 195–208. doi:10.1016/j.ijmecsci.2015.06.020.

[78] R. Pokharel, J. Lind, A.K. Kanjarla, R.A. Lebensohn, S.F. Li, P. Kenesei, R.M. Suter, A.D. Rollett, Polycrystal Plasticity: Comparison Between Grain - Scale Observations of Deformation and Simulations, Annu. Rev. Condens. Matter Phys. 5 (2014) 317–346. doi:10.1146/annurev-conmatphys-031113-133846.

[79] P.A. Turner, C.N. Tomé, A study of residual stresses in Zircaloy-2 with rod texture, Acta Metall. Mater. 42 (1994) 4143–4153. doi:10.1016/0956-7151(94)90191-0.

[80] T. Zhang, J. Jiang, B. Britton, B. Shollock, F. Dunne, Crack nucleation using combined crystal plasticity modelling, high-resolution digital image correlation and high-resolution electron backscatter diffraction in a superalloy containing non-metallic inclusions under fatigue, Proc. R. Soc. London A Math. Phys. Eng. Sci. 472 (2016). http://rspa.royalsocietypublishing.org/content/472/2189/20150792 (accessed April 5, 2017).

[81] R.C. Buckingham, C. Argyrakis, M.C. Hardy, S. Birosca, The effect of strain distribution on microstructural developments during forging in a newly developed nickel base superalloy, Mater. Sci. Eng. A. 654 (2016) 317–328. doi:10.1016/j.msea.2015.12.042.

[82] D.R. Chang, D.D. Krueger, R. a. Sprague, Superalloy Powder Processing, Properties, and Turbine Disk Applications, Superalloys 1984 (Fifth Int. Symp. (1984) 245–273. doi:10.7449/1984/Superalloys_1984_245_273.

[83] P.A. Shade, B. Blank, J.C. Schuren, T.J. Turner, A rotational and axial motion system load frame insert for in situ high energy x-ray studies, Rev. Sci. Instrum. 86 (2015).

[84] M. Preuss, P.J. Withers, J.W.L. Pang, G.J. Baxter, Inertia welding nickel-based superalloy: Part II. Residual stress characterization, Metall. Mater. Trans. A. 33 (2002) 3227–3234. doi:10.1007/s11661-002-0308-x.

[85] A. Lyckegaard, E.M. Lauridsen, W. Ludwig, R.W. Fonda, H.F. Poulsen, On the Use of Laguerre Tessellations for Representations of 3D Grain Structures, Adv. Eng. Mater. 13 (2011) 165–170. doi:10.1002/adem.201000258.

[86] M.A. Groeber, M.A. Jackson, DREAM.3D: A Digital Representation Environment for the Analysis of Microstructure in 3D, Integr. Mater. Manuf. Innov. 3 (2014) 5. doi:10.1186/2193-9772-3-5.

[87] T. Zhang, D.M. Collins, F.P.E. Dunne, B.A. Shollock, Crystal plasticity and high-resolution electron backscatter diffraction analysis of full-field polycrystal Ni superalloy strains and rotations under thermal loading, Acta Mater. 80 (2014) 25–38. doi:10.1016/j.actamat.2014.07.036.

[88] H. Mughrabi, R. Wang, K. Differt, U. Essmann, Fatigue Crack Initiation by Cyclic Slip Irreversibilities in High-Cycle Fatigue, in: Fatigue Mech. Adv. Quant. Meas. Phys. Damage, ASTM International, 100 Barr Harbor Drive, PO Box C700, West Conshohocken, PA 19428-2959, 1983: pp. 5-5–41. doi:10.1520/STP30551S.

[89] B. Lin, L.G. Zhao, J. Tong, H.-J. Christ, Crystal plasticity modeling of cyclic deformation for a polycrystalline nickel-based superalloy at high temperature, Mater. Sci. Eng. A. 527 (2010) 3581–3587. doi:10.1016/j.msea.2010.02.045.

[90] A. Yamaji, K. Sato, Distances for the solutions of stress tensor inversion in relation to misfit angles that accompany the solutions, Geophys. J. Int. 167 (2006) 933–942. doi:10.1111/j.1365-246X.2006.03188.x.

[91] H. Ritz, P. Dawson, T. Marin, Analyzing the orientation dependence of stresses in polycrystals using vertices of the single crystal yield surface and crystallographic fibers of orientation space, J. Mech. Phys. Solids. 58 (2010) 54–72. doi:10.1016/j.jmps.2009.08.007.

[92] J.C. Schuren, P.A. Shade, J. V. Bernier, S.F. Li, B. Blank, J. Lind, P. Kenesei, U. Lienert, R.M. Suter, T.J. Turner, D.M. Dimiduk, J. Almer, New opportunities for quantitative tracking of polycrystal responses in three dimensions, Curr. Opin. Solid State Mater. Sci. 19 (2015) 235–244. doi:10.1016/j.cossms.2014.11.003.

[93] W. Pabst, G. Tichá, E.V.A. Gregorová, Effective elastic properties of alumina-zirconia composite ceramics - part 3 . calculation of elastic moduli of polycrystalline alumina and zirconia from monocrystal data, Ceramics-Silikáty. 48 (2004) 41–48.

[94] J. Lankford, F.N. Kusenberger, Initiation of fatigue cracks in 4340 steel, Metall. Trans. 4 (1973) 553–559. doi:10.1007/BF02648709.

[95] R. Prasannavenkatesan, J. Zhang, D.L. McDowell, G.B. Olson, H.-J. Jou, 3D modeling of subsurface fatigue crack nucleation potency of primary inclusions in heat treated and shot peened martensitic gear steels, Int. J. Fatigue. 31 (2009) 1176–1189. doi:10.1016/j.ijfatigue.2008.12.001.

[96] J. Zhang, R. Prasannavenkatesan, M.M. Shenoy, D.L. McDowell, Modeling fatigue crack nucleation at primary inclusions in carburized and shot-peened martensitic steel, Eng. Fract. Mech. 76 (2009) 315–334. doi:10.1016/j.engfracmech.2008.10.011.

[97] R. Pokharel, R.A. Lebensohn, Instantiation of crystal plasticity simulations for micromechanical modelling with direct input from microstructural data collected at light sources, Scr. Mater. 132 (2017) 73–77. doi:10.1016/j.scriptamat.2017.01.025.

[98] J. Lankford, Initiation and early growth of fatigue cracks in high strength steel, Eng. Fract. Mech. 9 (1977) 617–624. doi:10.1016/0013-7944(77)90074-1.

[99] P. Clement, J.P. Angeli, A. Pineau, SHORT CRACK BEHAVIOUR IN NODULAR CAST IRON, Fatigue Fract. Eng. Mater. Struct. 7 (1984) 251–265. doi:10.1111/j.1460-2695.1984.tb00194.x.

[100] K.S. Chan, J. Lankford, The role of microstructural dissimilitude in fatigue and fracture of small cracks, Acta Metall. 36 (1988) 193–206. doi:10.1016/0001-6160(88)90038-7.

[101] J.C. Newman, E.P. Phillips, M.H. Swain, Fatigue-Life Prediction Methodology Using Small-Crack Theory, 1997. doi:10.1016/S0142-1123(98)00058-9.

[102] J. Lankford, D.L. Davidson, K.S. Chan, The influence of crack tip plasticity in the growth of small fatigue cracks, Metall. Mater. Trans. A. 15 (1984) 1579–1588. doi:10.1007/BF02657797.

[103] J.F. McCarver, R.O. Ritchie, Fatigue crack propagation thresholds for long and short cracks in René 95 Nickel-base superalloy, Mater. Sci. Eng. 55 (1982) 63–67. doi:10.1016/0025-5416(82)90084-2.

[104] Y. Murakami, M. Endo, Effects of defects, inclusions and inhomogeneities on fatigue strength, (1993). doi:10.1016/0142-1123(94)90001-9.

[105] E. Ferrié, J.-Y. Buffière, W. Ludwig, 3D characterisation of the nucleation of a short fatigue crack at a pore in a cast Al alloy using high resolution synchrotron microtomography, Int. J. Fatigue. 27 (2005) 1215–1220. doi:10.1016/J.IJFATIGUE.2005.07.015.

[106] J.-Y. Buffière, S. Savelli, P.H. Jouneau, E. Maire, R. Fougères, Experimental study of porosity and its relation to fatigue mechanisms of model Al–Si7–Mg0.3 cast Al alloys, Mater. Sci. Eng. A. 316 (2001) 115–126. doi:10.1016/S0921-5093(01)01225-4.

[107] S.T. Carter, J. Rotella, R.F. Agyei, X. Xiao, M.D. Sangid, Measuring fatigue crack deflections via cracking of constituent particles in AA7050 via in situ x-ray synchrotron-based micro-tomography, Int. J. Fatigue. 116 (2018) 490–504. doi:10.1016/J.IJFATIGUE.2018.07.005.

[108] W. Wen, P. Cai, A.H.W. Ngan, T. Zhai, An experimental methodology to quantify the resistance of grain boundaries to fatigue crack growth in an AA2024 T351 Al-Cu Alloy, Mater. Sci. Eng. A. (2016). doi:10.1016/j.msea.2016.04.071.

[109] W. Schaef, M. Marx, H. Vehoff, A. Heckl, P. Randelzhofer, A 3-D view on the mechanisms of short fatigue cracks interacting with grain boundaries, Acta Mater. 59 (2011) 1849–1861. doi:10.1016/J.ACTAMAT.2010.11.051.

[110] W. Ludwig, J.-Y. Buffière, S. Savelli, P. Cloetens, Study of the interaction of a short fatigue crack with grain boundaries in a cast Al alloy using X-ray microtomography, Acta Mater. 51 (2003) 585–598. doi:10.1016/S1359-6454(02)00320-8.

[111] M. Herbig, A. King, P. Reischig, H. Proudhon, E.M. Lauridsen, J. Marrow, J.-Y. Buffière, W. Ludwig, 3-D growth of a short fatigue crack within a polycrystalline microstructure studied using combined diffraction and phase-contrast X-ray tomography, Acta Mater. 59 (2011) 590–601. doi:10.1016/j.actamat.2010.09.063.

[112] J.P. Hanson, A. Bagri, J. Lind, P. Kenesei, R.M. Suter, S. Gradečak, M.J. Demkowicz, Crystallographic character of grain boundaries resistant to hydrogen-assisted fracture in Ni-base alloy 725, Nat. Commun. 9 (2018) 3386. doi:10.1038/s41467-018-05549-y.

[113] A.D. Spear, S.F. Li, J.F. Lind, R.M. Suter, A.R. Ingraffea, Three-dimensional characterization of microstructurally small fatigue-crack evolution using quantitative fractography combined with post-mortem X-ray tomography and high-energy X-ray diffraction microscopy, Acta Mater. (2014). doi:10.1016/j.actamat.2014.05.021.

[114] G.P. Sheldon, T.S. Cook, J.W. Jones, J. Lankford, Some observations on small fatgiue cracks in a superalloy, 3 (1981) 219–228. doi:10.1111/j.1460-2695.1980.tb01361.x.

[115] T.J. Marrow, M. Mostafavi, T. Hashimoto, G.E. Thompson, A quantitative three-dimensional in situ study of a short fatigue crack in a magnesium alloy, Int. J. Fatigue. (2014). doi:10.1016/j.ijfatigue.2014.04.003.

[116] J. Oddershede, B. Camin, S. Schmidt, L.P. Mikkelsen, H.O. Sørensen, U. Lienert, H.F. Poulsen, W. Reimers, Measuring the stress field around an evolving crack in tensile deformed Mg AZ31 using three-dimensional X-ray diffraction, Acta Mater. 60 (2012) 3570–3580. doi:10.1016/J.ACTAMAT.2012.02.054.

[117] D. Wilson, Z. Zheng, F.P.E. Dunne, A microstructure-sensitive driving force for crack growth, J. Mech. Phys. Solids. 121 (2018) 147–174. doi:10.1016/J.JMPS.2018.07.005.

[118] W.D. Musinski, D.L. McDowell, Simulating the effect of grain boundaries on microstructurally small fatigue crack growth from a focused ion beam notch through a three-dimensional array of grains, Acta Mater. 112 (2016) 20–39. doi:10.1016/J.ACTAMAT.2016.04.006.

[119] H. Proudhon, J. Li, W. Ludwig, A. Roos, S. Forest, Simulation of Short Fatigue Crack Propagation in a 3D Experimental Microstructure, Adv. Eng. Mater. 19 (2017) 1600721. doi:10.1002/adem.201600721.

[120] G.M. Castelluccio, D.L. McDowell, Microstructure-sensitive small fatigue crack growth assessment: Effect of strain ratio, multiaxial strain state, and geometric discontinuities, Int. J. Fatigue. 82 (2016) 521–529. doi:10.1016/J.IJFATIGUE.2015.09.007.

[121] J.D. Hochhalter, D.J. Littlewood, M.G. Veilleux, J.E. Bozek, A.M. Maniatty, A.D. Rollett, A.R. Ingraffea, A geometric approach to modeling microstructurally small fatigue crack formation: III. Development of a semi-empirical model for nucleation, Model. Simul. Mater. Sci. Eng. 19 (2011) 035008. doi:10.1088/0965-0393/19/3/035008.

[122] A. Rovinelli, R.A. Lebensohn, M.D. Sangid, Influence of microstructure variability on short crack behavior through postulated micromechanical short crack driving force metrics, Eng. Fract. Mech. 138 (2015) 265–288. doi:10.1016/j.engfracmech.2015.03.001.

[123] P. Neumann, The geometry of slip processes at a propagating fatigue crack—II, Acta Metall. 22 (1974) 1167–1178. doi:10.1016/0001-6160(74)90072-8.

[124] P. Neumann, Coarse slip model of fatigue, Acta Metall. 17 (1969) 1219–1225. doi:10.1016/0001-6160(69)90099-6.

[125] R.M.N. Pelloux, Mechanisms of formation of ductile fatigue striations., ASM Trans. Q., 1969.

[126] A. Rovinelli, M.D. Sangid, H. Proudhon, W. Ludwig, Using machine learning and a data-driven approach to identify the small fatigue crack driving force in polycrystalline materials, Npj Comput. Mater. 4 (2018) 35. doi:10.1038/s41524-018-0094-7.

[127] A. Fatemi, D.F. Socie, A critical plane approach to multiaxial fatigue damage including out-of-phase loading, Fatigue Fract. Eng. Mater. Struct. 11 (1988) 149–165. doi:10.1111/j.1460-2695.1988.tb01169.x.

[128] G.M. Castelluccio, D.L. McDowell, A mesoscale approach for growth of 3D microstructurally small fatigue cracks in polycrystals, Int. J. Damage Mech. 23 (2014) 791–818. doi:10.1177/1056789513513916.

[129] G.R. Irwin, Linear fracture mechanics, fracture transition, and fracture control, Eng. Fract. Mech. 1 (1968) 241–257. doi:10.1016/0013-7944(68)90001-5.

[130] A.M. Korsunsky, D. Dini, F.P.E. Dunne, M.J. Walsh, Comparative assessment of dissipated energy and other fatigue criteria, Int. J. Fatigue. 29 (2007) 1990–1995. doi:10.1016/J.IJFATIGUE.2007.01.007.

[131] M.D. Sangid, G.J. Pataky, H. Sehitoglu, R.G. Rateick, T. Niendorf, H.J. Maier, Superior fatigue crack growth resistance, irreversibility, and fatigue crack growthâ€“microstructure relationship of nanocrystalline alloys, Acta Mater. 59 (2011) 7340–7355. doi:10.1016/j.actamat.2011.07.058.

[132] G.M. Castelluccio, D.L. McDowell, Assessment of small fatigue crack growth driving forces in single crystals with and without slip bands, Int. J. Fract. 176 (2012) 49–64. doi:10.1007/s10704-012-9726-y.

[133] J. Lankford, The growth of small fatigue cracks in 7075-T6 Aluminum, Fatigue Fract. Eng. Mater. Struct. 5 (1982) 233–248. doi:10.1111/j.1460-2695.1982.tb01251.x.

[134] D.C. Pagan, M.P. Miller, Connecting heterogeneous single slip to diffraction peak evolution in high-energy monochromatic X-ray experiments, J. Appl. Crystallogr. 47 (2014) 887–898. doi:10.1107/S1600576714005779.

[135] P.A. Shade, B. Blank, J.C. Schuren, T.J. Turner, P. Kenesei, K. Goetze, R.M. Suter, J. V. Bernier, S.F. Li, J. Lind, U. Lienert, J. Almer, A rotational and axial motion system load frame insert for in situ high energy x-ray studies, Rev. Sci. Instrum. 86 (2015) 093902. doi:10.1063/1.4927855.

[136] S.D. Shastri, K. Fezzaa, A. Mashayekhi, W.-K. Lee, P.B. Fernandez, P.L. Lee, IUCr, Cryogenically cooled bent double-Laue monochromator for high-energy undulator X-rays (50–200 keV), J. Synchrotron Radiat. 9 (2002) 317–322. doi:10.1107/S0909049502009986.

[137] H.F. Poulsen, S.F. Nielsen, E.M. Lauridsen, S. Schmidt, R.M. Suter, U. Lienert, L. Margulies, T. Lorentzen, D. Juul Jensen, IUCr, Three-dimensional maps of grain boundaries and the stress state of individual grains in polycrystals and powders, J. Appl. Crystallogr. 34 (2001) 751–756. doi:10.1107/S0021889801014273.

[138] M. Moscicki, P. Kenesei, J. Wright, H. Pinto, T. Lippmann, A. Borbély, A.R. Pyzalla, Friedel-pair based indexing method for characterization of single grains with hard X-rays, Mater. Sci. Eng. A. 524 (2009) 64–68. doi:10.1016/J.MSEA.2009.05.002.

[139] A. Borbely, L. Renversade, P. Kenesei, J. Wright, On the calibration of high-energy X-ray diffraction setups. I. Assessing tilt and spatial distortion of the area detector, J. Appl. Crystallogr. 47 (2014) 1042–1053. doi:10.1107/S160057671400898X.

[140] A. Borbély, L. Renversade, P. Kenesei, On the calibration of high-energy X-ray diffraction setups. II. Assessing the rotation axis and residual strains, J. Appl. Crystallogr. 47 (2014) 1585–1595. doi:10.1107/S1600576714014290.

[141] C. Laird, The Influence of Metallurgical Structure on the Mechanisms of Fatigue Crack Propagation "The Influence of Metallurgical Struc-ture on the Mechanisms of Fatigue Crack, 1967. doi:10.1520/STP47230S.

[142] M.D. Sangid, H. Sehitoglu, H.J. Maier, T. Niendorf, Grain boundary characterization and energetics of superalloys, Mater. Sci. Eng. A. 527 (2010) 7115–7125. doi:10.1016/J.MSEA.2010.07.062.

[143] Y. Gao, J.S. Stölken, M. Kumar, R.O. Ritchie, High-cycle fatigue of nickel-base superalloy René 104 (ME3): Interaction of microstructurally small cracks with grain boundaries of known character, Acta Mater. 55 (2007) 3155–3167. doi:10.1016/J.ACTAMAT.2007.01.033.

[144] A. Rovinelli, Y. Guilhem, H. Proudhon, R.A. Lebensohn, W. Ludwig, M.D. Sangid, Assessing reliability of fatigue indicator parameters for small crack growth via a probabilistic framework, Model. Simul. Mater. Sci. Eng. 25 (2017) 045010. doi:10.1088/1361-651X/aa6c45.

[145] D.C. Pagan, J. V. Bernier, D. Dale, J.Y.P. Ko, T.J. Turner, B. Blank, P.A. Shade, Measuring Ti-7Al slip system strengths at elevated temperature using high-energy X-ray diffraction, Scr. Mater. 142 (2018) 96–100. doi:10.1016/J.SCRIPTAMAT.2017.08.029.

[146] R.I. Stephens, H.O. Fuchs, Metal fatigue in engineering, Wiley, 2001.

[147] Y.H. Zhang, L. Edwards, The effect of grain boundaries on the development of plastic deformation ahead of small fatigue cracks, Scr. Metall. Mater. 26 (1992) 1901–1906. doi:10.1016/0956-716X(92)90056-K.

[148] C. Efstathiou, D.E. Boyce, J.-S. Park, U. Lienert, P.R. Dawson, M.P. Miller, A method for measuring single-crystal elastic moduli using high-energy X-ray diffraction and a crystal-based finite element model, Acta Mater. 58 (2010) 5806–5819. doi:10.1016/J.ACTAMAT.2010.06.056.

[149] H. Simons, A. King, W. Ludwig, C. Detlefs, W. Pantleon, S. Schmidt, I. Snigireva, A. Snigirev, H.F. Poulsen, Dark-field X-ray microscopy for multiscale structural characterization, Nat. Commun. 6 (2015). doi:10.1038/ncomms7098.

[150] W.E. Frazier, Metal Additive Manufacturing: A Review, J. Mater. Eng. Perform. 23 (2014) 1917–1928. doi:10.1007/s11665-014-0958-z.

[151] M.D. Sangid, T.A. Book, D. Naragani, J. Rotella, P. Ravi, A. Finch, P. Kenesei, J.-S. Park, H. Sharma, J. Almer, X. Xiao, Role of heat treatment and build orientation in the microstructure sensitive deformation characteristics of IN718 produced via SLM additive manufacturing, Addit. Manuf. 22 (2018) 479–496. doi:10.1016/J.ADDMA.2018.04.032.

[152] F. McClintock, Local criteria for ductile fracture, Int. J. Fract. Mech. 4 (1968) 101–130. doi:10.1007/BF00188939.

[153] P.E. Magnusen, E.M. Dubensky, D.A. Koss, The effect of void arrays on void linking during ductile fracture, Acta Metall. 36 (1988) 1503–1509. doi:10.1016/0001-6160(88)90217-9.

[154] R. Becker, The effect of porosity distribution on ductile failure, J. Mech. Phys. Solids. 35 (1987) 577–599. doi:10.1016/0022-5096(87)90018-4.

[155] V. Tvergaard, A. Needleman, Analysis of the cup-cone fracture in a round tensile bar, Acta Metall. 32 (1984) 157–169. doi:10.1016/0001-6160(84)90213-X.

[156] J.R. Rice, D.M. Tracey, On the ductile enlargement of voids in triaxial stress fields∗, J. Mech. Phys. Solids. 17 (1969) 201–217. doi:10.1016/0022-5096(69)90033-7.

[157] A.L. Gurson, Continuum Theory of Ductile Rupture by Void Nucleation and Growth: Part I—Yield Criteria and Flow Rules for Porous Ductile Media, J. Eng. Mater. Technol. 99 (1977) 2. doi:10.1115/1.3443401.

[158] V. Tvergaard, Interaction of very small voids with larger voids, Int. J. Solids Struct. 35 (1998) 3989–4000. doi:10.1016/S0020-7683(97)00254-0.

[159] A. Needleman, Void Growth in an Elastic-Plastic Medium, J. Appl. Mech. 39 (1972) 964. doi:10.1115/1.3422899.

[160] J. Besson, Continuum Models of Ductile Fracture: A Review, (n.d.). doi:10.1177/1056789509103482.

[161] X. Gao, J. Kim, Modeling of ductile fracture: Significance of void coalescence, Int. J. Solids Struct. 43 (2006) 6277–6293. doi:10.1016/J.IJSOLSTR.2005.08.008.

[162] Y. Bao, T. Wierzbicki, On fracture locus in the equivalent strain and stress triaxiality space, Int. J. Mech. Sci. 46 (2004) 81–98. doi:10.1016/J.IJMECSCI.2004.02.006.

[163] J.D. Carroll, L.N. Brewer, C.C. Battaile, B.L. Boyce, J.M. Emery, The effect of grain size on local deformation near a void-like stress concentration, Int. J. Plast. 39 (2012) 46–60. doi:10.1016/j.ijplas.2012.06.002.

[164] C.C. Battaile, J.M. Emery, L.N. Brewer, B.L. Boyce, Crystal plasticity simulations of microstructure-induced uncertainty in strain concentration near voids in brass, Philos. Mag. 95 (2015) 1069–1079. doi:10.1080/14786435.2015.1009958.

[165] R.A. Lebensohn, J.P. Escobedo, E.K. Cerreta, D. Dennis-Koller, C.A. Bronkhorst, J.F. Bingert, Modeling void growth in polycrystalline materials, Acta Mater. 61 (2013) 6918–6932. doi:10.1016/J.ACTAMAT.2013.08.004.

[166] B. Selvarajou, S.P. Joshi, A.A. Benzerga, Void growth and coalescence in hexagonal close packed crystals, J. Mech. Phys. Solids. 125 (2019) 198–224. doi:10.1016/J.JMPS.2018.12.012.

[167] V. Prithivirajan, M.D. Sangid, The role of defects and critical pore size analysis in the fatigue response of additively manufactured IN718 via crystal plasticity, Mater. Des. 150 (2018) 139–153. doi:10.1016/j.matdes.2018.04.022.

[168] A. Ghahremaninezhad, K. Ravi-Chandar, Ductile failure in polycrystalline OFHC copper, Int. J. Solids Struct. 48 (2011) 3299–3311. doi:10.1016/J.IJSOLSTR.2011.07.001.

[169] A. Ghahremaninezhad, K. Ravi-Chandar, Ductile failure behavior of polycrystalline Al 6061-T6, Int. J. Fract. 174 (2012) 177–202. doi:10.1007/s10704-012-9689-z.

[170] A. Ghahremaninezhad, K. Ravi-Chandar, Ductile failure behavior of polycrystalline Al 6061-T6 under shear dominant loading, Int. J. Fract. 180 (2013) 23–39. doi:10.1007/s10704-012-9793-0.

[171] S.F. Li, J. Lind, C.M. Hefferan, R. Pokharel, U. Lienert, A.D. Rollett, R.M. Suter, Three-dimensional plastic response in polycrystalline copper via near-field high-energy X-ray diffraction microscopy 1, J. Appl. Cryst. 45 (2012) 1098–1108. doi:10.1107/S0021889812039519.

[172] C. Landron, O. Bouaziz, E. Maire, J. Adrien, Experimental investigation of void coalescence in a dual phase steel using X-ray tomography, Acta Mater. 61 (2013) 6821–6829. doi:10.1016/J.ACTAMAT.2013.07.058.

[173] E. Maire, P.J. Withers, Quantitative X-ray tomography, Int. Mater. Rev. 59 (2014) 1–43. doi:10.1179/1743280413Y.0000000023.

[174] A. Weck, D.S. Wilkinson, E. Maire, H. Toda, Visualization by X-ray tomography of void growth and coalescence leading to fracture in model materials, Acta Mater. 56 (2008) 2919–2928. doi:10.1016/J.ACTAMAT.2008.02.027.

[175] A. Hosokawa, D.S. Wilkinson, J. Kang, E. Maire, Onset of void coalescence in uniaxial tension studied by continuous X-ray tomography, Acta Mater. 61 (2013) 1021–1036. doi:10.1016/J.ACTAMAT.2012.08.002.

[176] D.C. Pagan, M. Obstalecki, J.-S. Park, M.P. Miller, Analyzing shear band formation with high resolution X-ray diffraction, Acta Mater. 147 (2018) 133–148. doi:10.1016/J.ACTAMAT.2017.12.046.

[177] Material Datasheet: EOS Nickel IN718, EOS GmbH Electro Opt. Syst. Tech. Rep., 2015. [Online]. Available Http//Www.Eos.Info/Material-M. (2015).

[178] Y.S.J. Yoo, T.A. Book, M.D. Sangid, J. Kacher, Identifying strain localization and dislocation processes in fatigued Inconel 718 manufactured from selective laser melting, Mater. Sci. Eng. A. 724 (2018) 444–451. doi:10.1016/j.msea.2018.03.127.

[179] W.J. Sames, F.A. List, S. Pannala, R.R. Dehoff, S.S. Babu, The metallurgy and processing science of metal additive manufacturing, (2016). doi:10.1080/09506608.2015.1116649.

[180] J. Strößner, M. Terock, U. Glatzel, Mechanical and Microstructural Investigation of Nickel-Based Superalloy IN718 Manufactured by Selective Laser Melting (SLM), Adv. Eng. Mater. 17 (2015) 1099–1105. doi:10.1002/adem.201500158.

[181] D. Gürsoy, F. De Carlo, X. Xiao, C. Jacobsen, TomoPy: a framework for the analysis of synchrotron tomographic data., J. Synchrotron Radiat. 21 (2014) 1188–93. doi:10.1107/S1600577514013939.

[182] J. Schindelin, I. Arganda-Carreras, E. Frise, V. Kaynig, M. Longair, T. Pietzsch, S. Preibisch, C. Rueden, S. Saalfeld, B. Schmid, J.-Y. Tinevez, D.J. White, V. Hartenstein, K. Eliceiri, P. Tomancak, A. Cardona, Fiji: an open-source platform for biological-image analysis, Nat. Methods. 9 (2012) 676–682. doi:10.1038/nmeth.2019.

[183] A. Lyckegaard, G. Johnson, P. Tafforeau, Correction of ring artifacts in X-ray tomographic images The evolution of life histories in the Euarchonta View project Synchrotron imaging techniques View project Correction of Ring Artifacts in X-ray Tomographic Images, 2011. https://www.researchgate.net/publication/283832650 (accessed May 4, 2019).

[184] P. Haldipur, F.J. Margetan, R.B. Thompson, Estimation of Single-Crystal Elastic Constants from Ultrasonic Measurements on Polycrystalline Specimens, in: AIP Conf. Proc., AIP, 2004: pp. 1061–1068. doi:10.1063/1.1711735.

[185] G. Perrin, J.B. Leblond, Analytical study of a hollow sphere made of plastic porous material and subjected to hydrostatic tension-application to some problems in ductile fracture of metals, Int. J. Plast. 6 (1990) 677–699. doi:10.1016/0749-6419(90)90039-H.

[186] D. Fabrègue, T. Pardoen, A constitutive model for elastoplastic solids containing primary and secondary voids, J. Mech. Phys. Solids. 56 (2008) 719–741. doi:10.1016/J.JMPS.2007.07.008.

[187] K. Kapoor, M.D. Sangid, Initializing type-2 residual stresses in crystal plasticity finite element simulations utilizing high-energy diffraction microscopy data, Mater. Sci. Eng. A. 729 (2018) 53–63. doi:10.1016/J.MSEA.2018.05.031.

[188] N.A. Fleck, J.W. Hutchinson, V. Tvergaard, Softening by void nucleation and growth in tension and shear, J. Mech. Phys. Solids. 37 (1989) 515–540. doi:10.1016/0022-5096(89)90027-6.

[189] P.W. Bridgman, Studies in Large Plastic Flow and Fracture : With Special Emphasis on the Effects of Hydrostatic Pressure, NewYork: McGraw-Hill, 1952.

[190] T. Pardoen, J.. Hutchinson, An extended model for void growth and coalescence, J. Mech. Phys. Solids. 48 (2000) 2467–2512. doi:10.1016/S0022-5096(00)00019-3.

[191] X. Teng, T. Wierzbicki, Evaluation of six fracture models in high velocity perforation, Eng. Fract. Mech. 73 (2006) 1653–1678. doi:10.1016/J.ENGFRACMECH.2006.01.009.

[192] I. Barsoum, J. Faleskog, Rupture mechanisms in combined tension and shear—Experiments, Int. J. Solids Struct. 44 (2007) 1768–1786. doi:10.1016/J.IJSOLSTR.2006.09.031.

[193] K. Nahshon, J.W. Hutchinson, Modification of the Gurson Model for shear failure, Eur. J. Mech. - A/Solids. 27 (2008) 1–17. doi:10.1016/J.EUROMECHSOL.2007.08.002.

[194] P.J. Noell, J.D. Carroll, B.L. Boyce, The mechanisms of ductile rupture, Acta Mater. 161 (2018) 83–98. doi:10.1016/j.actamat.2018.09.006.

[195] S. Maddali, I. Calvo-Almazan, J. Almer, P. Kenesei, J.-S. Park, R. Harder, Y. Nashed, S.O. Hruszkewycz, Sparse recovery of undersampled intensity patterns for coherent diffraction imaging at high X-ray energies, Sci. Rep. 8 (2018) 4959. doi:10.1038/s41598-018-23040-y.

[196] U. Lienert, M.C. Brandes, J. V. Bernier, J. Weiss, S.D. Shastri, M.J. Mills, M.P. Miller, In situ single-grain peak profile measurements on Ti-7Al during tensile deformation, Mater. Sci. Eng. A. 524 (2009) 46–54. doi:10.1016/j.msea.2009.06.047.

[197] R. Bandyopadhyay, J. Rotella, D. Naragani, J.-S. Park, M. Eff, M.D. Sangid, Residual Strain Analysis in Linear Friction Welds of Similar and Dissimilar Titanium Alloys Using Energy Dispersive X-ray Diffraction, Metall. Mater. Trans. A. 50 (2019) 704–718. doi:10.1007/s11661-018-5034-0.

[198] G.E. (George E. Bacon, Neutron diffraction, Clarendon Press, 1975. https://inis.iaea.org/search/search.aspx?orig_q=RN:7224202 (accessed June 17, 2019).

[199] B.N. Sharma, D. Naragani, B.N. Nguyen, C.L. Tucker, M.D. Sangid, Uncertainty quantification of fiber orientation distribution measurements for long-fiber-reinforced thermoplastic composites, J. Compos. Mater. (2017) 002199831773353. doi:10.1177/0021998317733533.

VITA

Diwakar Naragani obtained his Bachelor of Mechanical Engineering from Thapar University, Patiala. During his Bachelors, he was part of a formula student racecar team as the chassis designer where the team designed an aluminum honeycomb composite monocoque. Additionally, he undertook an internship at Hindustan Aeronautics Ltd. in the structural design center and the composite manufacturing hub where he learnt the nuances of the structural FE design methodologies and nuances of the material choice during manufacturing for quality assurance. Through these experiences, the paramount importance of the choice of material throughout the design and life of a component became apparent.

Diwakar was admitted to Purdue University in 2013 for a Master of Science in Aeronautics and Astronautics with a major in structures and materials and a minor in systems engineering. During the Masters Diwakar worked on short projects with (i) Dr. Byron Pipes in material science for simulation of short fiber reinforced composites, (ii) Dr. Pablo Zavattieri in civil engineering with fracture modeling approaches using cohesive zone elements and mesh refinement techniques to alleviate mesh effect on a propagating crack and finally with (iii) Dr. Michael Sangid on predicting the properties of long-fiber-reinforced thermoplastic composites from experiementally determined fiber orientation data. After fulfilling the requirements of Master's program Diwakar continued in the school of Aeronautics and Astronautics for a PhD under the mentorship of Dr. Michael Sangid to pursue a study of defect structures in Ni-based superalloys through advanced experimental characterization techniques.

During the PhD, a focus was maintained on design of X-ray characterization experiments and understanding the basis of the experiments to exploit the several levels of rich information contained in X-ray data which are seldom used. Some foray was made into advanced modeling during this period, whenever the experimental results needed further corroboration from simulations. In August 2019, Diwakar successfully defended his PhD dissertation: High-energy X-ray study of Defect Mediated Damage in Bulk Polycrystalline Ni-superalloys. He is going to pursue a Post-doc with the Air Force Research Laboratory on high fidelity modeling and simulation with a focus on calibration from experimental techniques and verification through uncertainty quantification using experimental data.

PUBLICATIONS

Published:

[67] D. Naragani, M.D. Sangid, P.A. Shade, J.C. Schuren, H. Sharma, J.-S. Park, P. Kenesei, J. V. Bernier, T.J. Turner, I. Parr, Investigation of fatigue crack initiation from a non-metallic inclusion via high energy X-ray diffraction microscopy, Acta Mater. 137 (2017) 71–84. doi:10.1016/j.actamat.2017.07.027.

[151] M.D. Sangid, T.A. Book, D. Naragani, J. Rotella, P. Ravi, A. Finch, P. Kenesei, J.-S. Park, H. Sharma, J. Almer, X. Xiao, Role of heat treatment and build orientation in the microstructure sensitive deformation characteristics of IN718 produced via SLM additive manufacturing, Addit. Manuf. 22 (2018) 479–496. doi:10.1016/J.ADDMA.2018.04.032.

[197] R. Bandyopadhyay, J. Rotella, D. Naragani, J.-S. Park, M. Eff, M.D. Sangid, Residual Strain Analysis in Linear Friction Welds of Similar and Dissimilar Titanium Alloys Using Energy Dispersive X-ray Diffraction, Metall. Mater. Trans. A. 50 (2019) 704–718. doi:10.1007/s11661-018-5034-0.

[199] B.N. Sharma, D. Naragani, B.N. Nguyen, C.L. Tucker, M.D. Sangid, Uncertainty quantification of fiber orientation distribution measurements for long-fiber-reinforced thermoplastic composites, J. Compos. Mater. (2017) 002199831773353. doi:10.1177/0021998317733533.

Under review:

- D. Naragani, P.A. Shade, P. Kenesei, H. Sharma, M.D. Sangid, X-ray characterization of the micromechanical response ahead of a propagating short fatigue crack in a Ni-based superalloy, (2019) under review.
- D. Naragani, J.S. Park, P. Kenesei, M.D. Sangid, Void coalescence, and ductile failure in IN718 illuminated through high energy X-rays, (2019), under review.